Diplomarbeit

Modeling and evaluation of three-terminal impedance measurement configurations for solid oxide fuel cell electrodes

von

Richard Schlesinger, BSc
Matrikelnummer: 01428697

ausgeführt zum Zwecke der Erlangung des akademischen Grades

Diplom-Ingenieur (DI)

in Elektrotechnik/Energie- und Umwelttechnik

betreut von

Univ.Prof. Dipl.-Phys. Dr.rer.nat. Jürgen Fleig
Univ.Ass. DI Alexander Schmid
Dr.tech. DI Tobias Huber

eingereicht an der

Technischen Universität Wien

Institut für chemische Technologien und Analytik
Festkörperelektrochemie und Elektrokeramik

Wien, 26. Jänner 2018

Abstract

Solid oxide fuel cells (SOFCs) are a promising solution to various technological challenges, as they convert chemical energy directly into electrical energy. The electrochemical properties of the cell's electrodes and electrolyte, can be investigated by means of impedance spectroscopy (IS). To measure the separate impedance response of only one electrode of the electrochemical cell, a three-terminal configuration is required. However, implementing this method in solid state electrochemistry goes along with non-trivialities and error sources that do not exist to the same extent in liquid electrochemistry.

This work considers potential error sources and evaluates each of them quantitatively with special emphasis on their impact on thin film electrode measurements by means of finite elements analysis (FEA), electric circuit simulations and conducted measurements.

Three potential error sources were identified as crucial factors. Asymmetric electrode geometries go along with a shift of the reference equipotential line with frequency. This can lead to measurement errors and additional features like inductive loops in the impedance spectrum. Second, particular sample geometries go along with an electric potential spread across the reference electrode (RE). This causes a current flow through the reference electrode and a (frequency dependent) bypass of a part of the sample. Third, especially for high ohmic systems, coupling capacitances between the three electrodes are crucial, as they influence the impedance transfer function which can provoke additional features in the spectrum.

With the results of this work, it was possible to introduce an optimized sample and electrode geometry. This setup minimizes the error extent significantly in a wide range of electrode properties.

Keywords: Solid Oxide Fuel Cell (SOFC), Three-Point Impedance Spectroscopy, Reference Electrode (RE), Finite Elements Analysis (FEA), Electrode Kinetics, Electrochemical Energy Storage

Kurzfassung

Festoxidbrennstoffzellen (SOFCs) stellen eine vielversprechende Lösung zu verschiedensten technologischen Herausforderungen dar, indem sie chemische Energie direkt in elektrische Energie umwandeln. Die elektrochemischen Eigenschaften der SOFC Elektroden und des Elektrolyten können mittels Impedanzspektroskopie (IS) untersucht werden. Um die Impedanz von lediglich einer Elektrode einer elektrochemischen Zelle zu messen, ist eine Dreipunkt-Konfiguration vonnöten. Die Anwendung dieser Methode in der Festkörperelektrochemie geht jedoch mit Nichttrivialitäten und Fehlerquellen einher, die in der Flüssigelektrochemie in diesem Ausmaß nicht auftreten.

In dieser Arbeit werden potentielle Fehlerquellen diskutiert und mit Fokus auf den Einfluss auf Messungen an Dünnfilmelektroden quantitativ ausgewertet. Dazu wurden Finite Elemente Methode (FEM) Simulationen, elektrische Schaltkreissimulationen und Messungen durchgeführt.

Drei substantielle Fehlerquellen wurden identifiziert. Asymmetrische Elektrodengeometrien führen zu einer Verschiebung der Referenz-Äquipotentiallinie in Abhängigkeit der Frequenz. Das kann zu Messfehlern und zusätzlichen Erscheinungen im Impedanzspektrum führen. Weiters zeigte sich, dass bei gewissen Probengeometrien eine Potentialdifferenz entlang der Referenzelektrode (RE) vorliegt, die zu einem parasitären (frequenzabhängigen) Kurzschluss über die RE führt. Für hochohmige Systeme sind desweiteren Koppelkapazitäten zwischen den Elektroden relevant, die die Übertragungsfunktion der Impedanz beeinflussen, was wiederum zu speziellen Erscheinungen im Impedanzspektrum führen kann.

Mit den Ergebnissen dieser Arbeit war es möglich eine optimierte Zellgeometrie einzuführen. Diese reduziert das Fehlerausmaß bei einer breiten Spanne an Elektrodeneigenschaften beträchtlich.

Stichwörter: Festoxidbrennstoffzelle (SOFC), Dreipunkt Impedanzspektroskopie, Referenzelektrode (RE), Finite Elemente Methode (FEM), Elektrodenkinetik, Elektrochemische Energiespeicherung

Contents

Contents

1 Introduction

One of the bottlenecks in increasing the share of renewable volatile energy sources is energy storage. In an electrical power grid, supply always needs to meet demand and one must not exceed the other to ensure a stable grid with constant voltage and frequency [1]. Amongst others, excess electrical energy can be stored in form of chemical energy. A promising technological solution for chemical energy storage are solid oxide fuel/electrolysis cells (SOFC/SOEC) [2]. In SOFCs, a fuel (e.g. hydrogen or a hydrocarbon) is oxidized at the anode, whereas the reduction of the oxygen takes place separately at the cathode. The electrodes are connected by the solid electrolyte that serves as oxygen anion conductor. The electrons provided by the oxidation are lead over an electrical load where the released energy is used. If the process is operated in the reverse direction, i.e. for energy storage, the terminology is solid oxide electrolysis cell (SOEC).

SOFCs have the leverage that they directly convert the chemical energy into electrical energy. The detour over thermal and mechanical energy – as in conventional caloric power plants – is thus circumvented. This leads to higher efficiency since SOFCs are not limited to the Carnot efficiency and irreversible losses by conversion steps are minimized. The non-flammable solid electrolyte further contributes to the applicability of this technology.

The easy scalability enables the SOFC to be used for other purposes as well [3]. Decentral combined heat and power units are able to cover the energy demand of buildings. The car industry offers several application possibilities like electromobility and range extenders. Exhaust gas of SOFCs can be used as heat source for a gas or steam turbine to further increase the thermal efficiency of power plants [4]. These are only a few examples of the numerous application fields to employ this technology.

The state of the art solid electrolyte material is yttria stabilized zirconia (YSZ) [3, 5]. This ceramic conducts oxygen anions by its oxygen vacancies when heated

up to operating temperature. The current standard in SOFC anodes are Ni/YSZ cermets [3]. Since these feature faster kinetics than the cathode materials, the research focus is on the latter.

The most promising cathode materials are doped perovskites with a chemical formula of ABO_3 [6]. A wide range of those oxides are mixed conductors, referring to their capability of conducting electrons as well as oxygen anions. $La_{0.8}Sr_{0.2}MnO_3$ (LSM) – the current standard cathode material – proves to be chemically stable but rather high temperatures are required to ensure fast electrode kinetics, i.e. low resistances [3]. High operating temperatures decrease the practicability and first and foremost, set enormous demands for the materials in use. Specially relevant are the gas interconnects which connect the anode of one cell to the cathode of the neighbouring cell in series. Apart from low thermal expansion, high electronic conductivity and ionic insulation, those have to be mechanically and chemically stable in both, reducing and oxidizing conditions [7, 8]. High temperatures increase the challenge of meeting these requirements. Therefore, the exploration of superior electrode materials that can be operated at lower temperatures poses a major increase in technological and economical efficiency.

The efficiency of such cells is limited by its internal resistance which is caused to a large part by the non-reversible kinetics of the oxygen reduction reaction ($O_2 + 4\,e^- \longrightarrow 2\,O^{2-}$). To study this reaction, the impedance response of the cell can be measured by impedance spectroscopy (IS). The impedance response of the cell reflects a superposition of the electrochemical processes taking place within the sample and the spectrum can reveal kinetic and thermodynamic details of these processes. According to their conductive and capacitive properties, the different processes have different time constants and thus, the corresponding features in the spectrum can be distincted from one another.

Such measurements are typically done on sample cells consisting of a solid electrolyte and two electrodes. The sample is placed in an oxygen containing atmosphere and heated up to typical operating temperatures of about $600\,°C$ to $1000\,°C$. The electrodes are referred to as working electrode (WE) and counter electrode (CE). Geometrically well defined dense thin films are the preferred electrode struc-

tures to investigate the material's properties. Analyzing the geometry dependence of the observed processes can then help to determine reaction pathways and locations.

An inherent problem of two-point impedance spectroscopy is that the resulting measurement reflects a superposition of both electrodes (WE and CE) and the electrolyte. The electrolyte properties can be extracted easily, similar electrodes however are not separable due to their similar time constants. If one wants to acquire solely the impedance response of one electrode, other concepts need to be found. The simplest way is to create a cell with identical electrodes and normalize the measured properties to one electrode. However, superposed DC voltage (=bias) usually leads to different electrode properties of nominally identical electrodes due to their nonlinear resistance and voltage dependent capacitances. Thus, this method is very limited in practicability.

Another way to measure a single electrode is to use a very small microelectrode as WE combined with a very large CE. Due to the bigger area , the resistance of the counter electrode gets negligibly small and effectively vanishes in the impedance spectrum [9]. This method also goes along with some substantial disadvantages, though. Microelectrodes are produced by photolithography and ion beam etching, which irreversibly changes the surface properties of the electrodes.

The method to truly measure only the voltage drop (=overpotential) across the WE, is the three-terminal or three-point measurement. Here, a reference electrode (RE) is used to tap a reference potential close to the working electrode. The voltage is then measured between WE and RE which equates the WE overpotential and a part of the electrolyte. The WE overpotential is then divided by the current through the whole cell (WE to CE), to obtain the separate impedance of the WE. In liquid electrochemistry, a Haber-Luggin capillary is used to tap the reference potential [10, page 159]. This is a small glass tube that is dipped into the electrolytic solution and placed close to the WE. When dealing with solid bodies as electrolyte, the RE potential is not as trivial to acquire. Several publications starting from the mid 90s exist that deal with this topic. It has been found that the geometry of the cell drastically influences the observed overpotentials [11]. Studies showed

that distortions arise from a non-uniform reference potential in consequence of the transition from primary ($\omega \to \infty$) to secondary ($\omega \to 0$) current distribution [12–16]. This reference potential shift occurs in asymmetric cell configurations. An asymmetry can be caused by geometry as well as different WE/CE properties. Several cell geometries have been proposed and evaluated [12–14, 16–20], the main results were that a thicker electrolyte and a big distance from WE to RE tend to minimize errors. However, proposed geometries are rather hard to produce [13, 16] and require big electrolytes of heights up to 1 cm [16]. Other approaches are based on correction formulae [20, 21].

Apart from the non-uniform current distribution, other error sources have been identified. A high-ohmic RE for example, leads to a voltage divider effect between the RE and the voltmeter input impedance [22–26]. Coupling capacitances between the electrodes have also been detected to cause measurement distortions [24, 27]. There are plenty of other error sources arising from intrinsic as well as external error sources [28–33]. All in all, a broadly and simply applicable three-point measurement setup has not been discovered, yet.

Previous three-point impedance measurements with a novel electrode geometry performed at TU Wien, have again shown large measurement errors and artifacts [34]. Errors refer to erroneous measurement results or distorted impedance spectra. Artifacts are separate features in the impedance spectrum i.e. loops or semicircles that may influence the deduced electrochemical properties. With regard to these novel observations as well as to literature data, it is essential to further consider and improve the situation of three-point impedance measurements in solid state electrochemistry. This is the topic of the thesis. The main objectives can be formulated as follows:

- Identify known and discover potential error and artifact sources in three-point impedance spectroscopy

- Quantify potential measurement errors, with special focus on thin film electrode measurements

- Find a three-point measurement setup that avoids or at least minimizes mea-

surement errors and artifacts

The potential error sources were investigated in detail by conducting simulations. Finite Elements Analysis (FEA) was used to calculate the electric field distribution within the test samples on basis of a shortened Maxwell equation system. Apart from this simulation type with a distributive character, electric equivalent circuits with discrete elements representing the electrochemical reactions and external surroundings, were modeled as well. Morevoer, impedance spectroscopy measurements were conducted on samples with porous $La_{0.6}Sr_{0.4}FeO_{3-\delta}$ (LSF) electrodes to validate the simulation results.

2 Fundamentals

This chapter gives the reader a selection of the most import theoretical background behind this work. The chapter starts with an introduction to impedance spectroscopy (IS). The application for solid state electrochemical measurements, and especially the difference between two and three-point measurements is elucidated. A summary of currently known error and artifact sources for three-point measurements (see Table 2.1) will be presented. Since Finite Elements Analysis (FEA) is the central tool in this work, the second part of the chapter will describe the background of this method. The general working principle and the fundamental equation system behind the calculations are outlined.

2.1 Impedance Spectroscopy (IS)

Impedance spectroscopy is a measuring technique that uses the impedance response of a system to draw conclusions about the properties of an investigated sample. There are two potential ways to receive the impedance response of the cell. In a potentiostatic measurement, an AC voltage is applied to the electrodes and the resulting current is measured. In a galvanostatic measurement, an electric current is impressed and the concluding voltage drop is measured. In either ways, the impedance is obtained by Ohm's law. The impedance is acquired for various frequency points to obtain an impedance spectrum as a function of frequency.

The resulting impedance spectrum can then be fitted with electric equivalent circuits. The structure of the equivalent network reflects processes and mechanisms taking place within the sample. The magnitude of the particular elements refers to electrochemical properties of the sample. Depending on the processes' time constants, the features appear at according frequencies in the spectrum. The workflow of this method is described in the context of electrochemistry in the subsequent chapter 2.1.1.

The main leverages of IS are the easy practicability and the rather trivial measuring principle. However, interpreting the resulting spectra can often be nontrivial.

2.1.1 Electrochemical Impedance Spectroscopy (EIS)

Electrochemical impedance spectroscopy (EIS) is one of the most common methods to analyze electrochemical systems. To investigate mechanisms such as electrode kinetics and the particular quantitative properties, a sample cell consisting of a solid oxide electrolyte is contacted with a working electrode (WE) and a counter electrode (CE). Geometrically well defined dense thin films are most commonly chosen as electrode structure to conclude from the results to the electrochemical reaction mechanisms and processes. The cell is then put into an oxygen containing atmosphere and heated up to the operating temperature. Typical SOFC temperatures are 600 °C to 1000 °C. The impedance response is then acquired as described above in section 2.1.

Electrochemical systems are mainly ohmic-capacitive. Resistances arise generally out of electrode reactions and ionic or electronic transport within the electrode or the electrolyte. Capacitances are mainly a consequence of stoichiometry changes (chemical capacitances), interface capacitances or geometrical (dielectric) capacitances. With the prerequisite of a homogeneous current distribution, those physical properties can be projected on discrete equivalent circuit elements – resistor and capacitor. The whole (ideal) electrochemical cell can thus be modeled as an equivalent circuit of resistors and capacitors.

The polarization resistance R_{pol} is the most important characteristic to describe the electrochemical reaction kinetics of an electrode. The polarization resistance is one of the main parts of the internal resistance of an SOFC. In case the cell carries current, a part of the cell voltage ($R_{pol} \cdot I$) is lost at the electrode. In electrochemical terms, this voltage drop across an electrode is called the overpotential. The polarization resistance is nonlinear and depends on several factors like the electrode polarization (=overpotential), the temperature and the oxygen partial pressure of the surrounding atmosphere [35].
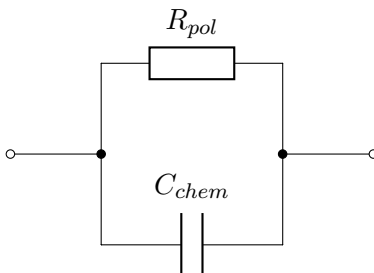
Figure 2.1: Simplified equivalent circuit of a surface limited thin film SOFC electrode with high electronic conductivity

The chemical capacitance C_{chem} is a non-electrostatic phenomenon. In the transmission line model of a mixed ionic and electronic conductor (MIEC), it appears as connection between the ionic and electronic conduction and is caused by a change in stoichiometry under polarization [36]. The capacitance scales linearly with the electrode volume and can reach enormous values of up to $10\,\frac{\mathrm{kF}}{\mathrm{cm}^3}$. Just as the polarization resistance, C_{chem} is also dependent on the temperature, oxygen partial pressure and the overpotential.

For surface limited electrodes with high electronic conductivity (which applies for most MIEC), the transmission line model presented in [36] can be simplified to a parallel circuit of R_{pol} and C_{chem} [37]. Therefore, thin film electrodes in equivalent networks were modeled as a parallel circuit of R_{pol} and C_{chem} as depicted in Figure 2.1. The applied AC voltage in electrochemical measurements is usually kept small ($\approx 10\,\mathrm{mV_{RMS}}$ to stay in the linear regime of the electrode resistance and capacitance.

A solid single crystal electrolyte can be modeled as an ohmic resistor arising from finite ionic conduction and a capacitor in parallel that represents the geometric i.e. dielectric capacitance of the sample. This geometric capacitance is only in the range of a few $10\,\mathrm{pF}$. Therefore, this dielectric capacitance can be neglected at higher temperatures, as the characteristic frequency of the $R_{YSZ}||C_{geo,YSZ}$-element is well beyond typical frequency ranges (up to $1\,\mathrm{MHz}$).

Thus, an equivalent circuit of a symmetric sample cell can be introduced. The equivalent network consists of working electrode (WE), counter electrode (CE)

and the electrolyte in between. The circuit of the sample cell is shown in Figure 2.2.
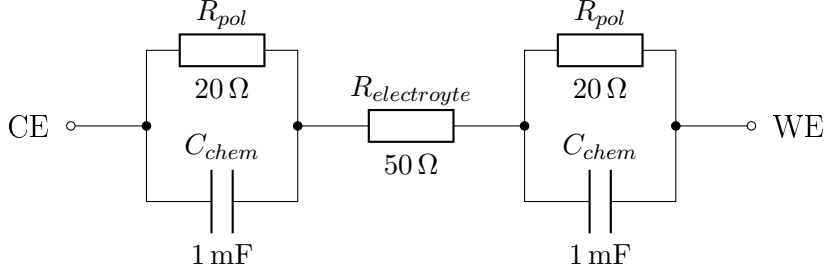

Figure 2.2: Equivalent network of a two-terminal symmetric sample cell; the elements are parameterized with exemplaric values, typical for perovskite thin films at operating temperatures around 600 °C to 650 °C (thin film height $\approx 50\,\text{nm}$, YSZ: $5\,\text{mm} \times 5\,\text{mm} \times 0.5\,\text{mm}$)

2.1.2 Impedance Spectra and their Interpretation

The impedance response of networks like the one in Figure 2.2 can be graphically displayed in a Nyquist or in a Bode Plot. The Nyquist plot shows the locus of the complex impedance in the complex plane. The electrochemist convention plots negative imaginary values upwards so that the graph is located mainly in the first quadrant. In a Bode Plot, the magnitude and the phase shift of a function is plotted over a logarithmic frequency axis.

The impedance spectrum of the symmetric cell in Figure 2.2 is depicted in Figure 2.3. The ohmic resistance of the electrolyte leads to a corresponding offset at the x-axis. A parallel circuit of a resistor and a capacitor (RC-element) leads to a semicircle in the Nyquist plot. The diameter equates the resistance and the capacitance can be extracted out of the angular peak frequency $\omega_{peak} = \frac{1}{RC}$. The reciprocal of the angular peak frequency is the relaxation time.
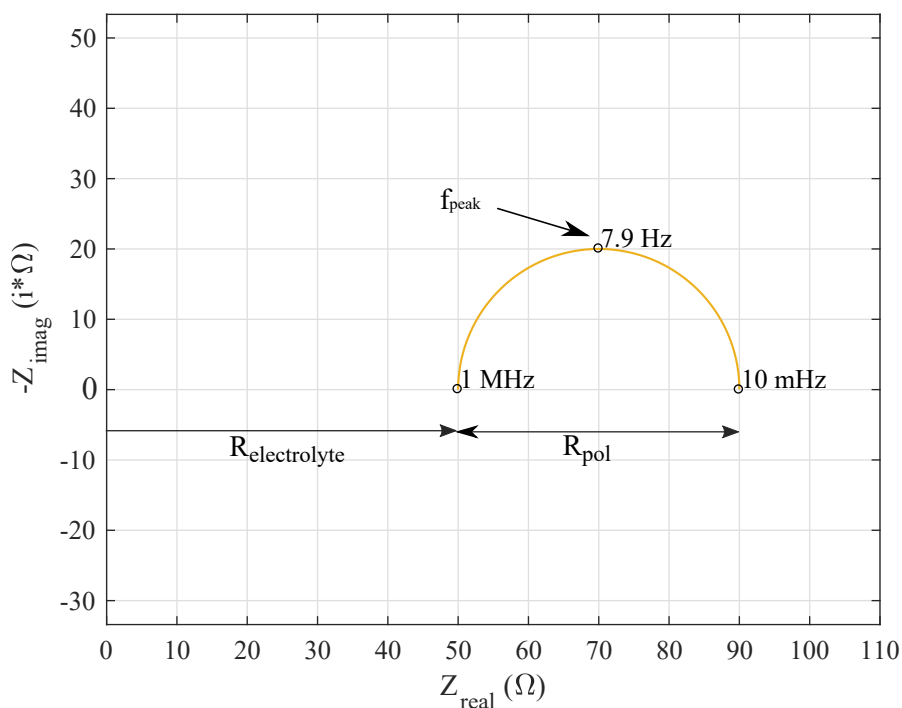
Figure 2.3: Impedance spectrum of the symmetric sample cell model depicted in
Figure 2.2

The spectrum in Figure 2.3 shows a capacitive semicircle with a diameter of $40\,\Omega$.
Due to the same peak frequency of WE and CE, their semicircles add up to one
big semicircle. The capacitance extracted from this big semicircle is $0.5\,\mathrm{mF}$. This
example shows that processes with similar time constants cannot be distinguished
in the case of two-point measurements on symmetric cells, only a superposition
of both electrodes is visible. Usually, one is interested in a single electrode, the
working electrode (WE). The concepts of normalizing the electrode properties to
one electrode and micro/macro arrangements were already elucidated in the intro-
duction and go along with severe disadvantages. Those methods especially fail if
a DC voltage (=bias) is superposed to the AC signal, because it is not possible
to determine the particular voltage drops across each single electrode. Therefore,
three-terminal measurements are required to measure solely the voltage drop across

the WE.

2.1.3 Three-Terminal Measurements

The basic idea of a three-terminal measurement is to add a reference electrode (RE) and tap a reference potential between the WE and the CE. The voltage is then measured from the RE to the WE terminal. The current is provided by the CE and measured through the whole circuit (from CE to WE). By applying Ohm's law and dividing the measured voltage by the measured current, one can achieve the separate impedance of the WE. The equivalent network of the symmetric sample cell of Figure 2.2 in a three-point measuring setup is depicted in Figure 2.4.
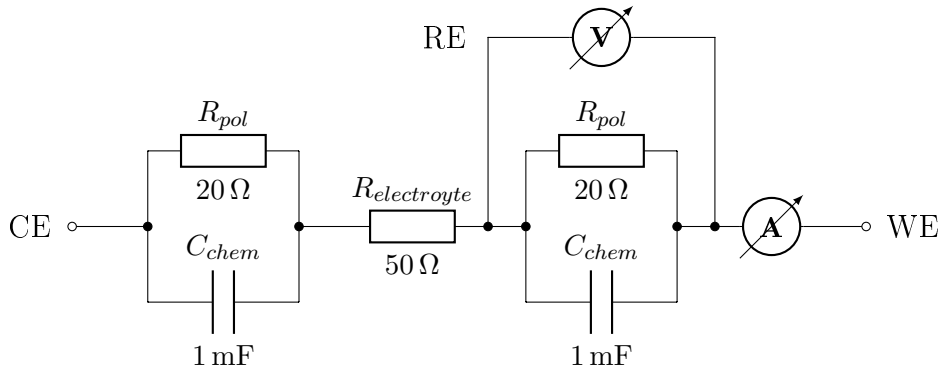

Figure 2.4: Three-point measurement equivalent network

The resulting impedance spectrum of the three-point measurement is depicted in Figure 2.5. The diameter of the semicircle equals now exactly the chosen value for the polarization resistance of the WE ($20\,\Omega$). Also the extracted capacitance refers to the correct value of $1\,\mathrm{mF}$.

Three-point measurements are specially relevant for asymmetric electrode properties. The showcase example are measurements under bias. This leads to asymmetric electrode properties due to nonlinear electrode kinetics and voltage dependent chemical capacitances.
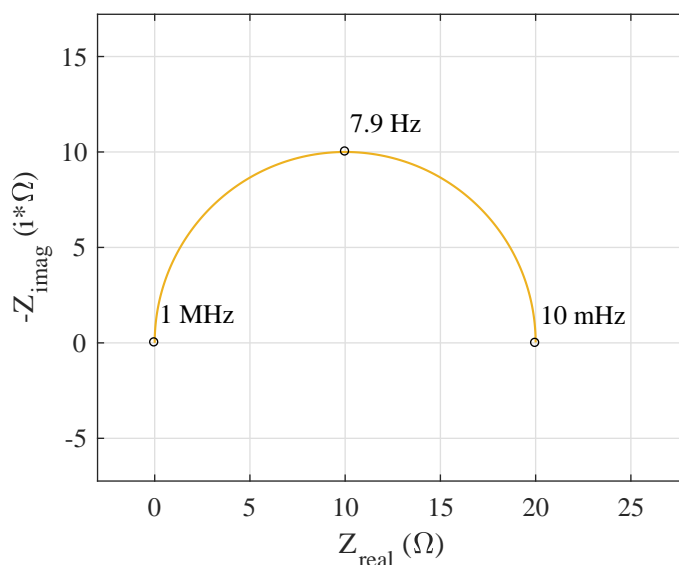
Figure 2.5: Impedance spectrum of the three-point measurement on the symmetric
sample cell model depicted in Figure 2.4

Unfortunately, the tapping of the reference potential on a three-dimensional solid
oxide is not trivial. There are plenty of error sources that arise out of intrinsic
effects of the sample and external measuring equipment. The follow up section
2.1.4 contains a list of known potential error and artifact sources with regard to
their relevance for solid state electrochemistry. The influence on MIEC thin film
electrodes of these sources will be dealt with quantitatively in section 4.2.

2.1.4 Potential Artifact Sources in Three-Terminal Impedance Spectroscopy

Table 2.1 summarizes the known artifact and error sources for three-terminal
impedance spectroscopy measurements. The sources are categorized whether they
derive from intrinsic properties of the cell or from external sources. More precisely,
"intrinsic" refers to error sources that occur even with ideal measuring equipment.
Non-uniform current and potential distributions within the test sample are exam-

ples for this category. "External sources" arise of externalities like the measuring equipment i.e. feed cables or the potentiostat. They are tackled by assuming an ideal test sample. Additionally, it is outlined whether a source mostly affects high frequencies (HF), low frequencies (LF), or both. Numerous errors can originate

Table 2.1: Artifact and error sources in three-terminal impedance spectroscopy

Intrinsic	LF	HF
RE does not separate WE overpotential from rest of cell	x	x
Non uniform (frequency dependent) current distribution	x	x
Inhomogeneous current density at inspected surface	x	x
External	LF	HF
Voltage divider effect between RE and voltmeter	x	x
Feed cable inductance and capacitance		x
Amperemeter-bypass by capacitive coupling to external shielding	x	
Bandwidth of current-to-voltage converter exceeded		x
Intrinsic and External	LF	HF
Three-terminal transfer characteristic	x	x

from intrinsic properties of the sample itself. In liquid electrochemistry, the reference potential required for the voltage measurement is easy to measure. Here, a Haber-Luggin capillary is dipped into the electrolytic solution and placed close to the working electrode [10, page 159]. Obviously, in solid state electrochemistry this cannot be done in the same way. The tapping of the correct reference potential is the reason why three-terminal measurements in solid state electrochemistry are a non-trivial issue.

RE does not separate WE overpotential from rest of cell

The purpose of the reference electrode is to separate the overpotential of the working electrode from the voltage drop across the rest of the cell. There are certain scenarios, in which this purpose cannot be fulfilled. Depending on the geometry of

the cell, the RE potential might consist not only of the WE overpotential and the almost inevitable part of the electrolyte, but also a part of the CE overpotential (cross contamination). This scenario can arise from geometrical circumstances and can be caused by electrode misalignment combined with an unfavourable placement of the reference electrode [14, 15]. It can be investigated by finite elements analysis of the sample and displaying the equipotential line of the reference electrode. If this line ends at the interface between counter electrode and electrolyte, the measured impedance partly results from the CE (see Figure 2.6).
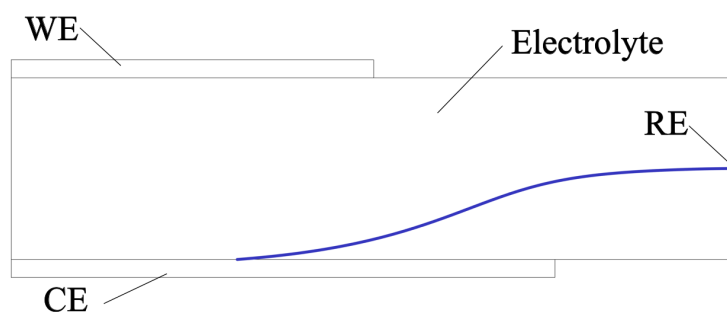

Figure 2.6: Cross contamination of the WE overpotential; the measured WE impedance contains parts of the CE impedance

This error source refers to the particular frequency points as standalone scenarios. A possible transition of the RE equipotential line over frequency is not addressed in this section. The next section deals with the pure variation of the RE potential regardless of the standalone field distributions.

Non Uniform (Frequency Dependent) Current Distribution

A real 3D sample cell comes with an essential difference to a 1D equivalent circuit. Due to the ohmic-capacitive electrode properties, the current distribution changes with frequency which is also reflected in the potential distribution. This can be visualized by the view of the primary ($\omega \to \infty$) versus the secondary ($\omega \to 0$)

(a) Primary current distribution ($\omega \to \infty$)   (b) Secondary current distribution ($\omega \to 0$)

Figure 2.7: Difference of primary and secondary current distribution due to ohmic-capacitive properties of the electrodes

current distribution within a sample.

At high frequencies, the electrodes are effectively short circuited by their chemical capacitance. The effective sample resistance arises exclusively from the electrolyte. To minimize the resistance, the current maximizes the effective cross section and thus expands within the electrolyte. For low frequencies, the electrodes are no longer short circuited and also contribute to the overall resistance. Thus, the current path homogeneously distributes over the electrode surface to maximize the cross section through the electrode as well. This leaves less possibility for the current to expand within the electrolyte at low frequencies.

Figure 2.7 shows the current distributions within an exemplaric sample cell where the electrodes do not spread across the whole surface. The reference potential is extracted at the right side of the sample directly at center height. This current distribution shift was already pointed out in [38].

This transition itself does not distort the measurement in case of a symmetric cell arrangement because the reference equipotential line does not shift over frequency. However, in case of asymmetric samples that are caused by geometry asymmetries or different WE/CE properties, the consequence for the measurement is a reference equipotential line shift [12–16]. Figure 2.8 shows the discrepancy of the high fre-
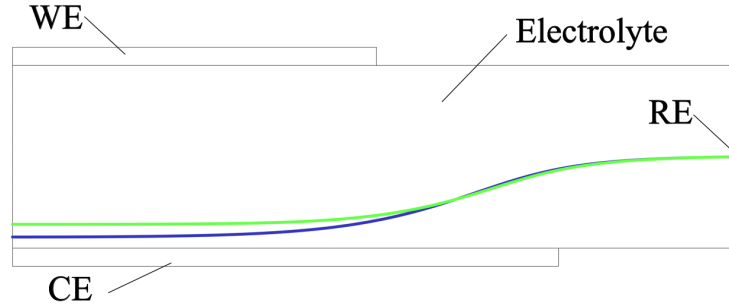
Figure 2.8: Shift of the reference equipotential line; Green line: RE potential for $\omega \to \infty$, Dark blue line: $\omega \to 0$

quency and low frequency RE equipotential line (2D). The RE potential shift leads to the fact that the amount of the measured electrolyte changes with frequency. This circumstance causes distorted arcs or inductive loops in the impedance spectrum.

This effect scales with misalignment of WE and CE. A thick electrolyte decreases the extent of this error source. In case of thin electrolytes and WE-CE misalignments, this effect can lead to very critical errors [12, 14, 15]. According to [16], also differences of WE/CE polarization resistances and interface capacitances increase the error of this phenomenon.

Inhomogeneous Current Density at Inspected Surface

An inhomogeneous current density at an inspected surface does not necessarily lead to artifacts or features in the impedance spectrum. However, in order to characterize materials regardless of the geometry, the ohmic (polarization resistance, electrolyte conductivity) and capacitive properties (interface or chemical capacitance) need to be related to the area. Of course, meaningful results are only achieved if the current density is homogeneous over the whole surface the property is related to. In case of inhomogeneous current densities, the integral $\int_{\mathcal{A}} \vec{n} \cdot \vec{J} \, dA$

will no longer simplify to the product of magnitude of current density times area. Accordingly, the specific resistance and capacitance can no longer be projected to discrete elements featuring a fixed impedance like the polarization resistance [13, 28].

Three-terminal Transfer Characteristic

This error source is effectively caused by coupling capacitances between the electrodes. The couple capacitances are a sum of both, the measuring probes and intrinsic capacitances (geometric capacitances between electrodes). Therefore, this issue is classified as intrinsic and external source.

Impedance transfer functions are usually non bijective complex functions. This means that a specific transfer function can possibly be deduced from more than one electric circuit.

In this specific case, a three-terminal equivalent circuit with purely ohmic electrodes and coupling capacitances between the electrode terminals (see Figure 2.9) leads to the very same impedance transfer function as a two-terminal network that was discovered by Fletcher [27]. The equivalent circuit contains a fictive inductance
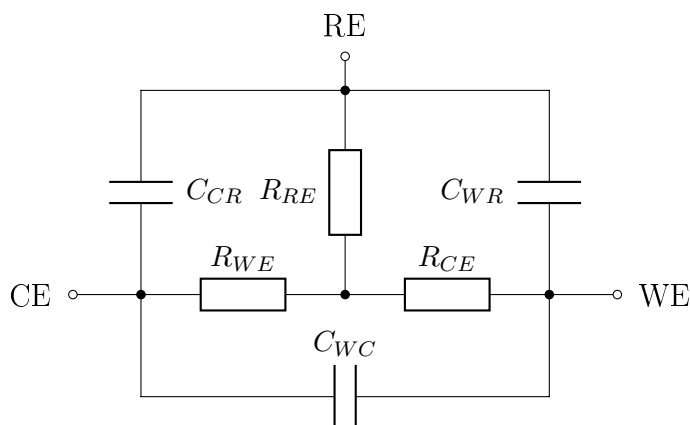

Figure 2.9: Original electric circuit-scheme of a 3-terminal network with purely ohmic electrodes and no electrolyte resistance (as in liquid electrochemistry)

and other non-existent elements. This can explain non-intuitive artifacts that may arise from three point measurements.

The two-terminal equivalent circuit is depicted in Figure 2.10. For low frequencies, the reactance of the capacitances $X_C = \frac{1}{\omega C}$ gets very high, so that the current flowing through the capacitances gets very low and causes an equivalently low voltage drop. The reactance of the series inductance $X_L = \omega L$ becomes very low for small frequencies and its influence on the measurement is negligible. However, for high frequencies, the working electrode is bypassed over the capacitances and the inductance can reach a similar magnitude like the resistance of the working electrode. This means that a part of the current does not flow through the WE, but bypasses it via C_1 and C_2. Additionally, a voltage divider effect between working electrode and inductance emerges. Both effects decrease the voltage drop across the working electrode, leading to a lower measured impedance. Over the whole evaluated frequence range, one or the other effect may prevail and subsequently, loops in the impedance spectrum may occur.

It is noteworthy that this equivalent circuit is derived from an aqueous electro-
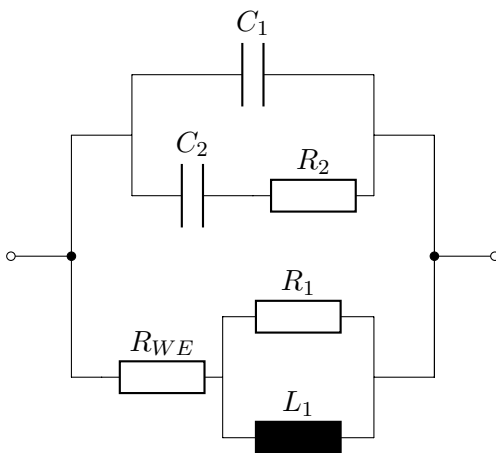

Figure 2.10: Two-terminal equivalent circuit of the three-terminal cell in Figure 2.9 according to Fletcher [27]

chemical system. The electrode impedances are purely ohmic and there are no chemical capacitances in parallel to the polarization resistances. Qualitative eval-

uations on the effect of coupling capacitances, however are also valid for solid state electrochemistry. Moreover, this model can easily be extended to solid electrolyte systems by replacing the electrode resistances with RC-elements and a serial electrolyte resistance. The values of the fictive elements can be calculated using the original element values. The equations according to Fletcher [27] are outlined below (equations 2.1 to 2.5).

$$L_1 = R_{RE}R_{CE}C_{CR} \tag{2.1}$$

$$R_1 = \frac{R_{RE}R_{CE}}{R_{RE} + R_{CE}} \tag{2.2}$$

$$R_2 = (R_{WE}R_{RE} + R_{WE}R_{CE} + R_{RE}R_{CE})\frac{C_{CR}}{R_{WE}C_2} \tag{2.3}$$

$$C_1 = C_{WR} + C_{WC} + \frac{C_{WR}C_{WC}}{C_{CR}} \tag{2.4}$$

$$C_2 = \frac{R_{RE}C_{WR}}{R_{WE}} + \frac{R_{CE}C_{WC}}{R_{WE}} - \frac{C_{WR}C_{WC}}{C_{CR}} \tag{2.5}$$

where

R_{WE}, R_{RE}, R_{CE} ... Polarization resistances of working, reference and counter electrode

C_{WR} ... Coupling capacitance between working and reference electrode

C_{CR} ... Coupling capacitance between counter and reference electrode

C_{WC} ... Coupling capacitance between working and counter electrode

Voltage Divider Effect between RE and Voltmeter

The voltage drop across the measured electrode is measured by a voltmeter. An ideal voltmeter features an infinitely high input impedance. In reality, however, the input impedance of a voltmeter Z_{input} is finite and consists of a very big resistance in parallel to a very small capacitance. The reference electrode impedance $\underline{Z}_{RE}$ and the input impedance of the voltmeter form a voltage divider together and the measured voltage can be calculated according to equation 2.6 (complex quantities

are underlined).

$$\underline{U}_m = \frac{\underline{Z}_{input}}{\underline{Z}_{input} + \underline{Z}_{RE}} \tag{2.6}$$

This effect is negligible, if Z_{RE} is much smaller than Z_{input}. However, one needs to consider that other influences can decrease the effective input impedance of the voltmeter. For example, if the shield of the RE BNC cable is grounded, the capacitance between the signal conductor and its shield is effectively in parallel to the input impedance and therefore adds up to the overall capacitance, lowering the overall impedance Z_{input}. A possible way to avoid this contribution is to actively shield the voltage BNC cable. Active shielding forces the signal lead and its shield on the same potential and thus the capacitance is cancelled out. The voltage divider effect was already pointed out by Hsieh who conducted electric circuit simulations in [22] and carried out measurements in [23]. Special attention to high reference electrode impedances by high electrode-electrolyte interface resistances was given in [24].

Feed Cable Inductance and Capacitance

The influence of cable inductances and capacitances can be evaluated according to an infinitesimal two-wire transmission line model [1, page 451]. The model comprises a series resistance (R') and inductance (L') and a cross conductance (G') and capacitance (C'). In reality, a two-wire line consists of an infinite number of these circuits that are connected in series. The model is depicted in Figure 2.11. In case the cable is lossless, R' and G' drop out. On basis of the remaining
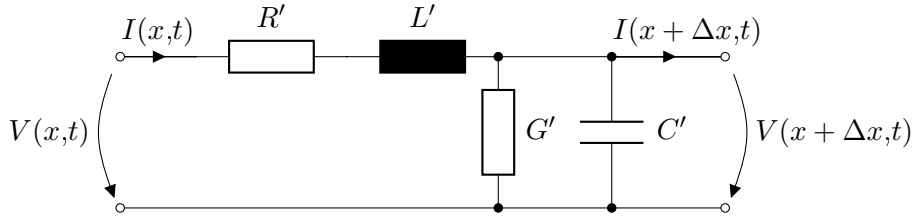

Figure 2.11: Transmission line model of a two-wire circuit

quantities, the wave resistance Z_0 can be defined according to equation 2.7 [see 1, page 455].

$$Z_0 = \sqrt{\frac{L'}{C'}} \tag{2.7}$$

If a transmission line is concluded with the wave resistance, electromagnetic waves are absorbed completely without any reflection effects at the end of the line. The wave resistance is important if one wants to investigate wave-phenomena which play a role for electromagnetic oscillations that feature wavelengths that are in the same order of magnitude like the length of the transmission line. In this thesis the wave resistance is used in a more fundamental context. Wave conductors feature a specific wave resistance which is usually known (e.g. datasheet) and thus the inductance can be calculated if the capacitance is known and vice versa.

For two parallel conductors with a center-to-center distance D and a diameter d, the inductance and capacitance per unit length can be calculated according to equations 2.8 ([see 39, page 284]) and 2.9 ([see 40, page 248]).

$$L' = \frac{\mu}{\pi} \operatorname{arccosh}\left(\frac{D}{d}\right) \tag{2.8}$$

$$C' = \frac{\pi \epsilon}{\operatorname{arccosh}\left(\frac{D}{d}\right)} \tag{2.9}$$

where

L' ... Inductance per unit length $[\frac{\mathrm{H}}{\mathrm{m}}]$

$\mu = \mu_0 \mu_r$ ... Magnetic permeability $[\frac{\mathrm{V\,s}}{\mathrm{A\,m}}]$ (for air $\mu_r = 1$)

C' ... Capacitance per unit length $[\frac{\mathrm{F}}{\mathrm{m}}]$

$\epsilon = \epsilon_0 \epsilon_r$ ... Electric permittivity $[\frac{\mathrm{A\,s}}{\mathrm{V\,m}}]$ (for air $\epsilon_r = 1$)

and $\operatorname{arccosh}(x) = \ln(x + \sqrt{x^2 - 1})$

Amperemeter is bypassed by Coupling Capacitances to External Shielding

In [30], an effect is described that is related with the shielding of the whole measuring setup. The capacitive coupling from the sample to the shielding box can be

modeled by a connection from a defined point in the sample equivalent circuit to the grounded shield via a box capacitance C_m. This capacitance bypasses a part of the electrochemical process within the sample and the amperemeter. For high frequencies, when the reactance of C_m is low in comparison to the impedance of the bypassed part of the sample, a part of the electric current flows via C_m and no longer through the whole sample. This effectively lowers the magnitude of the current flowing through the amperemeter. According to [30], the resulting artifact is a capacitive semicircle that is bigger than the expected sample-semicircle, followed by an inductive semicircle concluding in the ohmic resistance of the sample at frequencies $\rightarrow 0$.

Bandwidth of Current-to-Voltage Converter exceeded

Apart from the voltage measurement related issue elucidated in section 2.1.4, there is also an error source arising from the current measurement. Current measurements in sensitive measurement setups are carried out by an operational amplifier that functions as a current-to-voltage converter as depicted in Figure 2.12. The
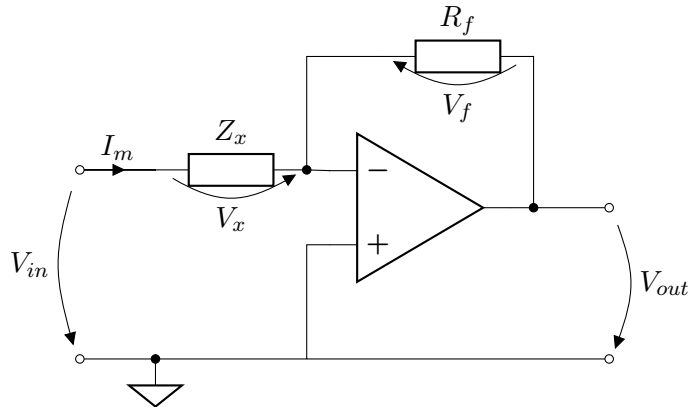

Figure 2.12: Current-to-voltage converter

electric current to be measured I_m is the current flowing through the inspected electrochemical cell with the overall impedance Z_x. I_m causes a voltage drop V_f

across the feedback resistor R_f which equals the output voltage V_{out} of the circuit. The current can then be calculated with Ohm's Law according to equation 2.10 (the minus arises from the voltage directions defined according to Figure 2.12).

$$I_m = - \frac{V_{out}}{R_f} \tag{2.10}$$

Since the non-inverting input of the operational amplifier is grounded and the amplifier controls V_{diff} to 0, the potential of the inverting input is effectively ground potential. This concept is related to as "virtual ground". The consequence of this is that the input impedance of the current to voltage converter equals 0 and does not influence the overall current I_m.

The gain of a closed loop inverting amplifier is defined according to equation 2.11 and purely dependent on the external impedances [see 41, page 8].

$$\text{Closed Loop Gain} = \frac{V_{out}}{V_{in}} = - \frac{R_f}{|Z_x|} \tag{2.11}$$

The gain of a real operational amplifier however, is limited. The easiest way to avoid excess of the maximum gain, is to keep the magnitude of the gain around 1. This can be achieved by choosing a feedback resistor with a resistance similar to the magnitude of the sample impedance [24].

When dealing with AC signals, one has to take into account that the gain of an operational amplifier is also frequency dependent. Above a characteristic frequency f_0, the gain drops by $-20\,\text{dB}$ per frequency decade due to a limited slew rate (how fast the output voltage can change in consequence of a change of the input signal $[\frac{\text{V}}{\text{µs}}]$) [24]. The frequency f_0 is essentially the bandwidth of the circuit. Thus, for $f > f_0$, V_{out} decreases, which corresponds to the measured current I_m. This circumstance leads to a higher measured impedance at high frequencies which equals inductive behaviour. This inductance however, is of course not a physical property of the cables or the sample, but an artifact arising from the measuring equipment. The bandwidth of an inverting operational amplifier can be calculated

according to equation 2.12 [see 41, page 212].

$$\text{Bandwidth} = \frac{\text{Gain Bandwidth product}}{\text{Closed Loop Gain}} \tag{2.12}$$

The Gain Bandwidth product is a constant parameter of the operational amplifier. The issue of of a limited bandwidth of the current-to-voltage converter was already pointed out in [24, 29, 31].

2.2 Finite Elements Analysis (FEA)

Finite Elements Analysis (FEA) was originally introduced as a method of structural mechanics. It is commonly used to calculate forces, mechanical stresses and resulting deformations of structural components. Moreover, this technique can be extended to several physical problems, such as acoustics, thermodynamics and electrochemistry by simply changing the underlying equations.
The application of the FEA method is quite straight forward. First, the continuous geometry of the physical problem is created or imported from an external CAD program. Next, the geometry is discretized into a finite number of small elements. One speaks of the FE mesh. The finer the mesh, the better the approximation to the continuous reality. After that, boundary conditions are set. For example an object can be forced on constant temperature, an object can be assigned to a constant electric potential (Dirichlet boundary conditions), or a constant heat source can be applied to an object (Neumann boundary bondition). For each finite element, the underlying differential equations are solved with the requisition of continuity at the edges of neighbouring elements. FEA allows a very precise approximation to the real analytical solution of systems of differential equations that arise from a physical problem of any desired geometry.
The underlying differential equations remain the same for all simulated geometries and scenarios. In this thesis, only stationary solutions in the frequency domain are relevant and the equations do not feature time dependencies. Since the sample dimensions are bigger than the skin depth of the magnetic field by several orders

of magnitude, a shortened Maxwell equation system without magnetic interactions is used. The skin depth of the magnetic field is given by equation 2.13.

$$\text{skin depth}\,\delta = \sqrt{\frac{2}{\mu\sigma\omega}} \tag{2.13}$$

μ ... Magnetic permeability $[\frac{\mathrm{V\,s}}{\mathrm{A\,m}}]$
σ ... Electric conductivity $[\frac{\mathrm{S}}{\mathrm{m}}]$
ω ... Angular frequency [1/s]
Inductive effects are hereby neglected and the electric field $\vec{E}$ is irrotational ($\vec{\nabla} \times \vec{E} = \vec{0}$). This permits the use of the electrostatic voltage definition, which is calculating the voltage between two locations as the difference of their electric potential V. Using this simplification is common practice in electrochemical field calculations. The equations that form the basis of the models are outlined below:

$$\vec{\nabla} \cdot \vec{J} = Q_{j,V} \tag{2.14}$$

$\vec{J}$ ... Electric current density $[\frac{\mathrm{A}}{\mathrm{m}^2}]$
$Q_{j,V}$ ... Current source within control volume $[\frac{\mathrm{A}}{\mathrm{m}^3}]$
In the modeled scenarios $Q_{j,V} = 0$ due to stationary conditions.

$$\vec{J} = \sigma\vec{E} + i\omega\vec{D} + \vec{J_e} \tag{2.15}$$

$\vec{E}$ ... Electric field intensity $[\frac{\mathrm{V}}{\mathrm{m}^2}]$
$\vec{D}$ ... Electric flux density or electric displacement field $[\frac{\mathrm{A\,s}}{\mathrm{m}^2}]$
$\vec{J_e}$ ... External current sources $[\frac{\mathrm{A}}{\mathrm{m}^2}]$
and i as the imaginary unit. In the model, there are no external current sources $\vec{J_e} = \vec{0}$. In a linear, isotropic and homogeneous material, the electric flux density $\vec{D}$ can be related to the electric field intensity $\vec{E}$ according to equation 2.16

$$\vec{D} = \epsilon\vec{E} \tag{2.16}$$

where ϵ is the electric permittivity consisting of the product of the vacuum permittivity ϵ_0 and a material dependent relative permittivity ϵ_r.

$$\vec{E} = -\vec{\nabla}V \tag{2.17}$$

V ... Electric potential [V]

Equation 2.14 is the electric current conservation or continuity equation. Equation 2.15 is the ohmic law in its complex local expression, whereas equation 2.17 is the equation for the electric field intensity when conditions are electrostatic or quasi electrostatic. The FEA program solves the electric current conservation with respect to Ohm's law and uses the electric potential as dependent variable.

If the current density $\vec{J}$ in equation 2.15 is inserted into the continuity equation 2.14, $\vec{D}$ is eliminated using equation 2.16 and the definition of the electric potential 2.17 is applied to the remaining mathematical expression, one obtains the well known Laplace's equation 2.18.

$$\Delta V = 0 \tag{2.18}$$

The solution of this equation $V(\vec{r})$ ($\vec{r}$ ... position vector) gives the electric potential distribution which is commonly illustrated in plotting equipotential lines (2D) or equipotential surfaces (3D).

3 Methodology

Two main methods were used in this work to analyze and quantify potential errors in three-point impedance spectroscopy: Simulations and measurements. The simulations were established to evaluate the error mechanisms. Furthermore, they enabled quantitative investigations. The measurements served mainly to

- Get physical properties of the examined materials as basic parameters for simulations

- Check results of the simulations for plausibility

- See if particular artifacts can be reproduced by certain means

Prior to the experimental and simulation sections, the investigated geometries are introduced.

3.1 Sample Geometries

All the impedance spectroscopy sample geometries featured yttria stabilized zirconia (YSZ) as solid oxygen anion electrolyte. The following abbreviations are used in this section:

- WE...Working electrode

- CE...Counter electrode

- RE...Reference electrode

Further details on the materials will be given in the experimental section 3.2.

3.1.1 Two-Terminal Geometry

The dimensions of the two-point sample electrolyte were $10\,\text{mm} \times 10\,\text{mm} \times 0.5\,\text{mm}$. The working and the counter electrode were attached to the sides with the area of $1\,\text{cm}^2$. Figure 3.1 shows a 3D model and a side view of the two-terminal sample.
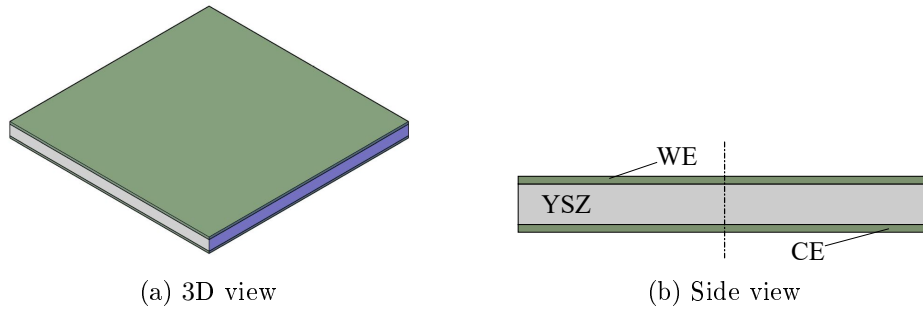

(a) 3D view   (b) Side view

Figure 3.1: Two-point sample

3.1.2 Ring Geometry

The ring geometry has been used in measurements previous to this work in [34]. This alignment consisted of a YSZ single crystal with an electrode surface of $5\,\text{mm} \times 5\,\text{mm}$. The total height of the substrate was $0.9\,\text{mm}$. At center height, there was a notch with a height of $0.3\,\text{mm}$ and a depth of $0.3\,\text{mm}$. Inside the notch, a porous reference electrode was brushed which was contacted with a platinum wire. 3D image and side view of this geometry are depicted in Figure 3.2.

(a) 3D view   (b) Side view
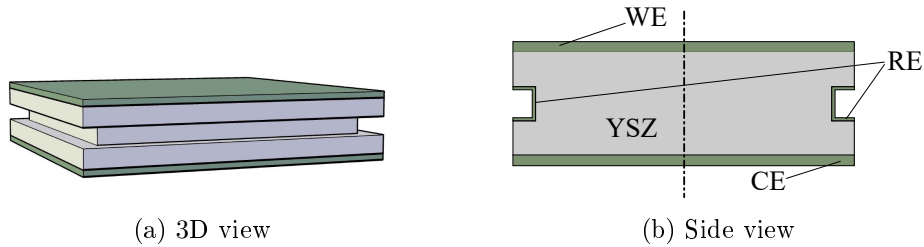
Figure 3.2: Ring geometry sample

3.1.3 Microelectrode Geometry

The microelectrode geometry sample featured the dimensions $10\,\text{mm} \times 10\,\text{mm} \times 0.5\,\text{mm}$, just as the two-point measurement sample. The difference to the two-point geometry is a cleared space without electrode material in the center of the working electrode. In the center of this hole, a microelectrode was placed and used as a reference electrode. The precise dimension of the cleared space is outlined in the specific results section 4.3.1. 3D view and sectional view are shown in Figure 3.3.

(a) 3D view   (b) Sectional view
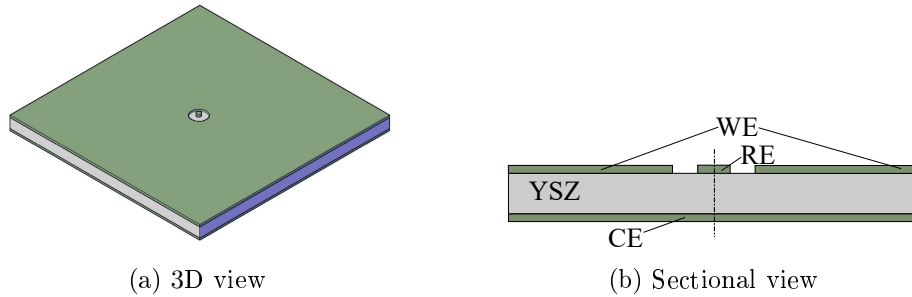
Figure 3.3: Microelectrode geometry sample

3.1.4 Rectangle Geometry

The YSZ substrate of the rectangle geometry featured the same dimensions like the microelectrody geometry and the two-point sample: $10\,\text{mm} \times 10\,\text{mm} \times 0.5\,\text{mm}$. Working and counter electrode faced each other on the surfaces of the size of $1\,\text{cm}^2$. The depth of the electrodes covered the whole sample depth of $10\,\text{mm}$. Various electrode lengths were investigated in measurement and simulation (see section 4.3.2). 3D view and side view of this geometry are given in Figure 3.4.

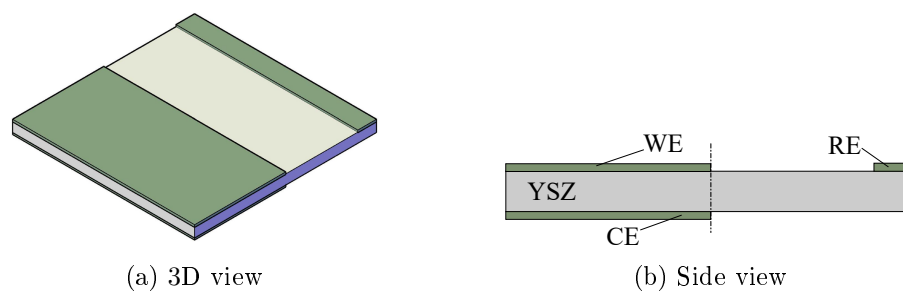(a) 3D view   (b) Side view

Figure 3.4: Rectangle geometry sample

3.1.5 Single Wing Geometry

In this geometry, a thicker YSZ substrate with the dimensions $10\,\text{mm} \times 10\,\text{mm} \times 1\,\text{mm}$ was chosen. The sample featured a symmetrical protrusion with a depth of $0.5\,\text{mm}$ and a height of $0.3\,\text{mm}$. This centric protrusion (=wing) served as host for the RE. The resulting surface of the aligned WE and CE area was thus $0.95\,\text{cm}^2$. Figure 3.5 shows a 3D view and a side view of this geometry.

(a) 3D view   (b) Side view
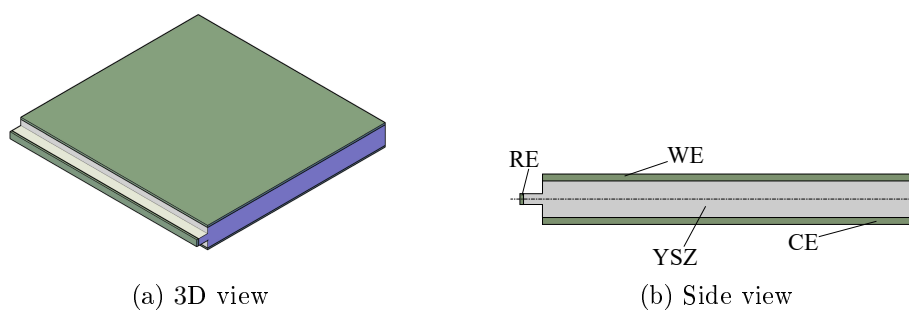
Figure 3.5: Single wing geometry sample

3.2 Experimental

This part covers the experiments on physical systems that were carried out. The biggest focus was on the evaluation of electrochemical systems. Apart from these,

also electric equivalent circuits were measured.

3.2.1 Sample Preparation

Two different substrate materials were used to perform the experiments. Yttria stabilized zirconia Y_2O_3 (YSZ) single crystals (9.5 mol% Y_2O_3; orientation 1 0 0; CrysTec Germany) served as oxygen ion conducting electrolyte in the impedance spectroscopy measurements. Both sides of the crystal were polished.

For Van der Pauw experiments, magnesium oxide MgO single crystals (orientation 1 0 0; CrysTec Germany) were used. Those experiments required insulating substrates. The magnesium oxide crystals were only polished on one side.

All measured electrodes in this work were porous $La_{0.6}Sr_{0.4}FeO_{3-\delta}$ (LSF) electrodes. To produce an electrode, LSF paste was brushed on the surfaces of the substrates and the sample was heated up to 100 °C for ten minutes. Since the electronic conductivity of LSF was not sufficient to polarize the whole electrode, a current collector was required. This was achieved by brushing an additional layer of platinum paste on top of the LSF layer. Then, the samples were sintered in air at 850 °C for 2 hours and 30 minutes.

For some geometries, there are noteworthy details on the preparation. The circle in the center of the microelectrode geometry was achieved by pushing the edge of a thin wire on the center of the surface while brushing the LSF paste on the sample. Thus, a small area stayed free of electrode material leaving a blank space for the RE.

To receive rather defined electrode edges for the rectangle geometry, a part of the substrate was covered with adhesive tape while brushing the electrode material on the YSZ sample. Obviously, the produced microelectrode and rectangle geometry were lacking precision due to the imperfect nature of the manual production processes.

The single wing geometry was not manufactured yet. All assessments to this geometry arise of simulations.

For the Van der Pauw measurements, the LSF electrode was brushed on the polished side of the MgO sample. There was no platinum current collector added on top of the LSF electrode, since these measurements were conducted to measure the in-plane conductivity of LSF.

3.2.2 Measurements

All measurements were conducted in synthetic air (21 vol% O_2, 79 vol% N_2) at a temperature of 635 °C unless stated otherwise in the specific section.

The impedance spectra were taken by applying a sine voltage of 0.01 V effective value between counter electrode (on potential) and working electrode (on ground potential). The evaluated frequency range reached from 1 MHz down to 10 mHz, 100 mHz (most frequent case) or 1 Hz.

Depending on the sample geometry, measurements required different contacting techniques. The two-terminal and the ring geometry samples were inserted vertically from above into the measuring apparatus and clamped between two platinum sheets. Thus, the electrical contact between WE and CE and their particular measuring probes was established. The RE of the ring geometry sample was contacted with an additional delicate platinum wire that was wrapped around the sample inside the notch.

The CE of microelectrode and the rectangle geometry samples were contacted by placing the bottom of the particular sample on a platinum sheet. WE and RE were contacted with PtIr needles mounted on flexible arms that carried the measurement probes inside. The porous electrode guaranteed sufficient grip of the wire and did not require further fixation. Only the tip of the RE needle of the microelectrode geometry was covered with LSF paste and put on the cleared spot on the YSZ substrate. This RE was then sintered in situ during the measurement. The contacting of the Van der Pauw samples was carried out by four Pt needles. To ensure precise results, the needles were placed as close as possible to the corners of the electrode.

3.2.3 Measuring Apparatuses

The previous sections focused on the samples. The following sections extend the documentation to the external measuring equipment. Since every type of measurement had certain requirements to meet, four different measuring apparatuses were used in this work. The two-point samples, the ring geometry samples and the Van der Pauw samples were measured with individual measuring apparatuses. The microelectrode and the rectangle geometry were carried out with the same measuring apparatus. Since the fundamental structure of the apparatuses is quite universal, only the last one mentioned will be described in detail as a showcase example.
The measuring apparatus consisted of the following elements (see Figure 3.6).

- A cradle of steel (A) on which the test rod (B) was mounted

- A bar of fused quartz with a flat surface (C) on which a platinum sheet (D) for contacting the counter electrode was clamped onto

- Pt needles (E) for contacting the working and reference electrode

- Cylindrical bars (F) in which the measuring probes for the electrodes were led through

- A sealing ring (G) as interface between flange (H) and airtight quartz glass cylinder (not visible in the picture)

- The BNC nodes (I) from the electrodes

- The cable (J) of the type K thermocouple located next to the platinum sheet (C)

- Gas inlet (K)

- And the gas outlet (L) with a bubbler (M) filled with silicone oil
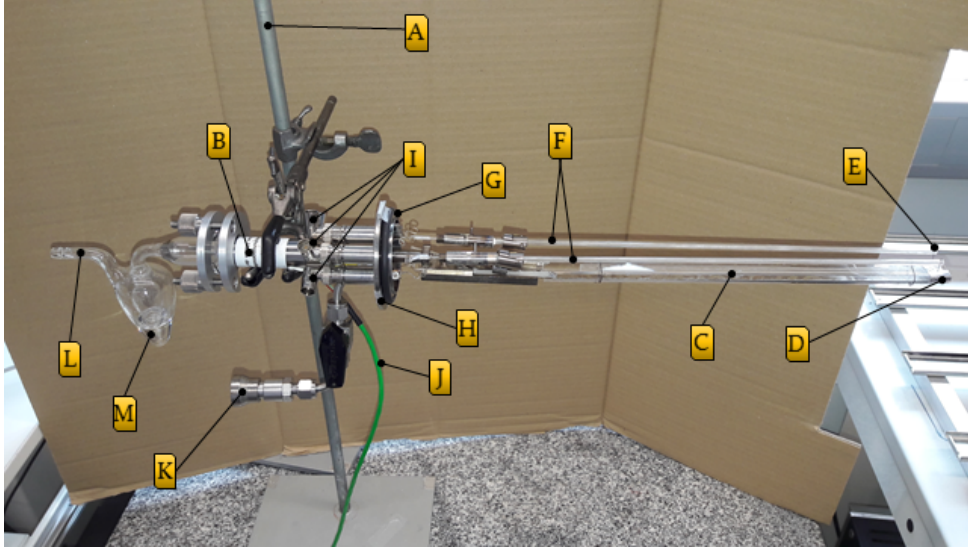
Figure 3.6: Measuring apparatus

The measurements were carried out as follows. The GERO SR(A) standard tube furnace on rails was set aside to get access to the test rod. The sample was placed on the platinum sheet and contacted with the Pt needles. After that, the furnace with the fused quartz cylinder was moved in direction of the measuring apparatus. Shocks needed to be avoided because the contacting needles slipped off easily. After sealing the quartz glass cylinder to the test rod, the inlet of synthetic air (Alphagaz, purity: 99.999 %) was started and remaining laboratory air was purged out for about 15 minutes. Next, the furnace was heated to the set point temperature. As already mentioned, all the measurements were taken at 635 °C. The test rod was shielded by a grounded mesh of steel to prevent electromagnetic distortions from the outside. The cradle of steel was grounded, as well. The type K thermocouple was connected to a Keithley 2000 multimeter which processed the input thermoelectric voltage to the corresponding temperature and sended this signal to the computer.

Figure 3.7 shows the measuring setup consisting of the measuring apparatus and the furnace. Figure 3.8 shows a contacted sample of the rectangle geometry.
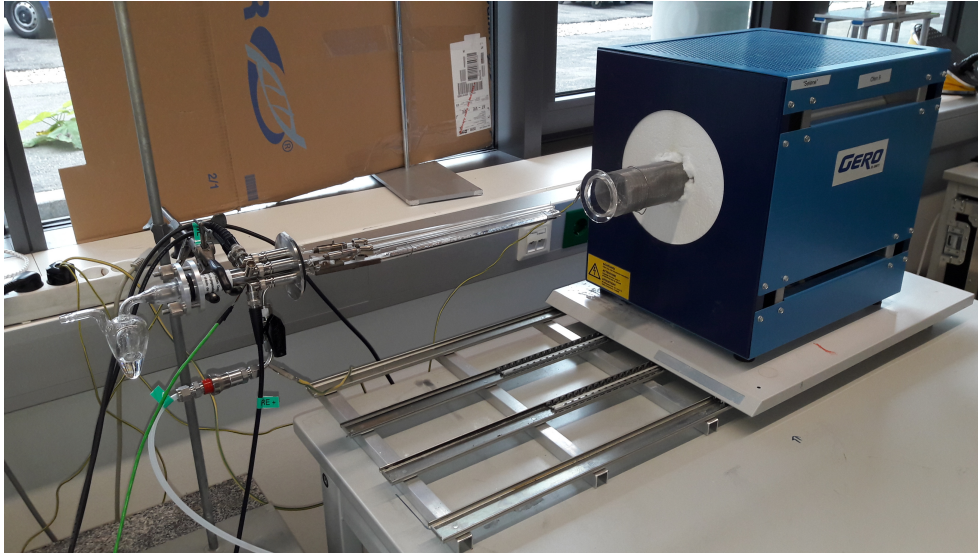
Figure 3.7: Measuring setup

Figure 3.8: Contacted rectangle geometry sample

3.2.4 Impedance Analyzer

All impedance spectra in this work were measured with a Novocontrol Alpha A9 Frequency Analyzer using a Novocontrol POT/GAL 30 V/2 A as potentiostat. The device was calibrated just before the measurements were taken. The impedance analyzer was controlled by the AC impedance software JAVA LAB 1.41. The measuring apparatus was connected to the impedance analyzer with coaxial BNC cables. The shield of the cables was connected to ground potential.

Two-Terminal Configuration

To prevent measuring the ohmic cable resistance as series resistance to the sample, the RE terminals from the potentiostat were connected directly to the working and counter electrode nodes at the measuring apparatus. The WE and CE nodes at the measuring apparatus are connected to the WE and CE nodes at the potentiostat. Thus, the two-point samples were measured in 4-Wire Mode. Figure 3.9 shows the wiring configuration of this measurement setup.
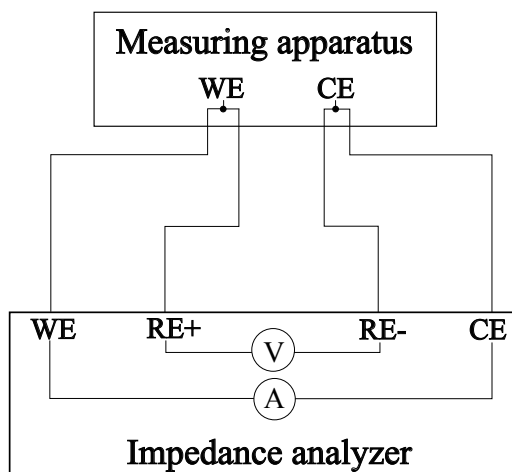
Figure 3.9: Two-terminal configuration

Three-Terminal Configuration

The three-point measurements were conducted in regular 3-Wire Mode. In this setup, WE and CE nodes from the measuring apparatus were connected to the WE and CE nodes at the potentiostat. These two terminals again are used for the current measurement. The RE node from the measuring apparatus linked to the actual reference electrode at the sample, was plugged into the RE+ node at the potentiostat. The voltage was measured between working electrode (WE) and reference electrode (RE) by the Novocontrol Alpha A9 Frequency Analyzer. Unlike in the two-terminal configuration, the voltage drop across the WE BNC cable was not omitted in this setup. Figure 3.10 shows the wiring configuration of the three-point measurements.
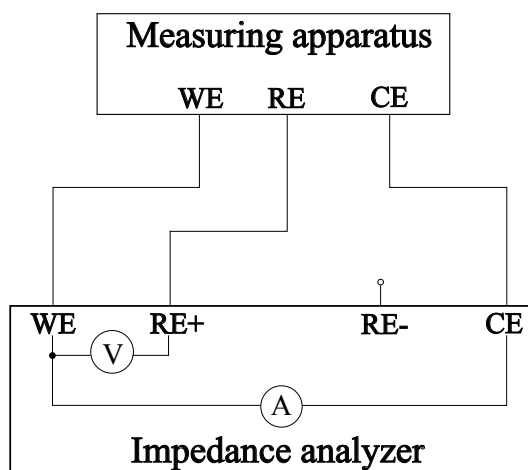
Figure 3.10: Three-terminal configuration

3.2.5 Electric Circuit Measurements

In order to check the influence of mainly external error sources, electric circuits were measured. This offers the advantage that intrinsic distortions like geometric effects or non ideal sample behaviour can be completely excluded as error source. Thus, external influences could have been investigated separately. The part of the

electric circuit that resembled the electrochemical cell consisted of three RC elements reflecting the electrodes (polarization resistance and chemical capacitance) and two resistances that resembled the electrolyte resistance. The circuit-scheme is depicted in Figure 3.11.
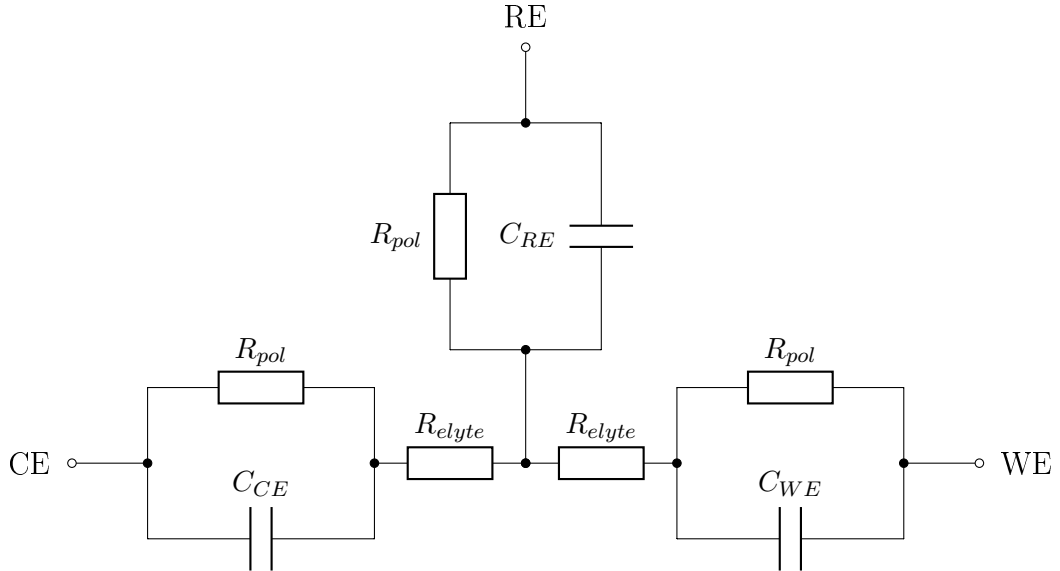

Figure 3.11: Electric circuit-scheme of a 3-terminal measurement setup

The values of the RC-elements of the electrodes are realistic parameters for mixed ionic electronic conductors (MIEC). Furthermore, the values are standardized electric components. Table 3.1 gives an overview of the used components.

Table 3.1: List of electric components

Element	Size	Tolerance	Type
R_{pol}	$200\,\Omega$	$\pm 1\,\%$	Thin film axial resistor
R_{elyte}	$47\,\Omega$	$\pm 1\,\%$	Thin film axial resistor
$C_{WE,\,CE}$	$33\,\mu F$	$\pm 10\,\%$	Polyester capacitor
C_{RE}	$10\,\mu F$	$\pm 5\,\%$	Polypropylene capacitor
$C_{couple\,big}$	$4.7\,\mu F$	$\pm 5\,\%$	Polypropylene capacitor
$C_{couple\,small}$	$10\,pF$	$\pm 10\,\%$	Ceramics capacitor

The circuit was built on a nickel project board. Tinned copper connection cables with 7 strands, a cross-sectional area of $0.22\,mm^2$ and a length from $5\,cm$ to $15\,cm$ were used in between most of the components. The effective value of the measuring voltage was $10\,mV$ just as in the electrochemical measurements. The frequency range of the electric circuit measurements reached from $10\,mHz$ to $1\,MHz$.

3.3 Simulations

Two kinds of simulations were performed for this thesis. In order to evaluate the distorting influence of coupling capacitances and other potential error sources, electric circuits were simulated with LTSPICE. LTSPICE is an open source Simulation Program with Integrated Circuit Emphasis (SPICE) that offers several analysis tools for simulating electric circuits.

In contrast to the electric circuit simulations with discrete elements, finite elements analyses with a distributed character were performed as well. This kind of analyses were carried out by using COMSOL MULTIPHYSICS. This program comprises fundamental physical equations from many disciplines. The equations of the different fields can be integrated coupled or separated from one another into the model.

Both kinds of simulations were crucial for the investigations. Electric circuit simulations are highly simplified and idealised models of the inspected systems that offer the possibility to investigate *one* certain effect isolated from other effects that occur in reality. Finite elements analysis allows a look deep into the system and enables investigations on effects which are not possible to evaluate or measure by other means. The depiction of the electric potential distribution and the electric current density field are examples for the numerous possibilities offered by finite elements analysis.

3.3.1 Equivalent Circuit Simulations (ECS)

The equivalent circuit simulations were carried out with LTSpice XVII. The simulations were performed by using the AC analysis tool. With this tool, the voltages and currents of interests were calculated for the chosen frequency range.

The core of every simulated model consisted of an independent current source and an ideal voltmeter. The ideal voltmeter was modeled as a purely ohmic resistance with a value of $1 \cdot 10^{50}\,\Omega$, which practically resembles an infinitely high input impedance, independent of the frequency. The current source fed a constant current of $1\,\mathrm{A}$ into the system. This current provoked a voltage drop across the voltmeter which was then tapped between reference point A and ground (see Figure 3.12).
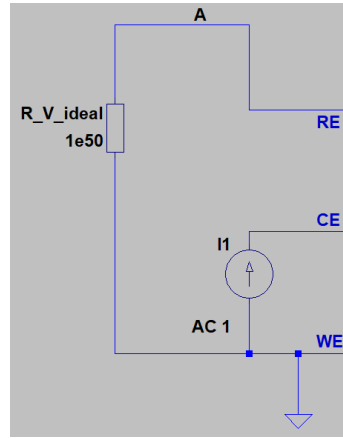
Figure 3.12: Model core

The voltage was then divided by the electric current to get the impedance of the electric circuit. The simulations covered a frequency range from $10\,\mathrm{mHz}$ to $1\,\mathrm{MHz}$. The ECS served to examine the influence of externalities like couple capacitances and wire impedances, but also equivalent circuits representing intrinsic effects. The simulated models are described more detailed in the particular results sections.

3.3.2 Finite Elements Analyses (FEA)

COMSOL MULTIPHYSICS 5.2a was used to perform the finite elements analyses in this thesis. This program is based on modules for different disciplines of physics and different types of analyses. To apply the equations outlined in section 2.2, the Electric Currents Module was used. For the calculation of impedance spectra over a certain frequency range, the Frequency Domain Study Type was used. For the numerical calculation of geometric capacitances, the Stationary Study Type was used which is a special case of the first study type, only that $\omega \equiv 0$.

Frequency Domain FEA Models

The different 3-terminal geometries (ring geometry, microelectrode geometry, rectangle geometry and single wing geometry) were simulated using a Frequency Domain study. In this study, the stationary solution is calculated for a range of frequencies. The most important outcomes of these simulations were 2-point and 3-point impedance spectra and the illustration of electric quantities like the electric potential V or the electric current density $\vec{J}$.

All the models were simulated in 2D only. This reduced the calculation time significantly and delivered the great advantage of being able to process a lot of scenarios in a short amount of time, thus enhancing the possibilities for sensitivity analyses and fine meshes. All the simulations featured the finest automatically generated mesh (Physics-controlled $\rightarrow$ Extremely fine). The simplification of breaking down the model to two dimensions was justified by modeling a two-terminal geometry sample in 2D as well as in 3D. The derived impedance spectra were identical.

The ring geometry and the microelectrode geometry were modeled rotationally symmetrical. As a consequence, rectangle areas became circular ones. Corresponding radii were calculated to keep the area of the surfaces constant. Thus, the impedances were kept comparable to other geometries.

The model did not consider electrons and oxygen ions as separate charge carriers within the electrode, but instead only contained one path for a general charge carrier.

Electrodes and the electrolyte were specified as rectangular objects (domains). Unlike the practical measurements that were conducted with porous electrodes, the simulations used well defined thin film electrodes. Each domain needed to be allocated to its electric conductivity σ and its relative permittivity ϵ_r. Since the limiting parameter of the electrode reaction is the oxygen exchange reaction [42] – taking place at the working and counter electrode surface – the effective electrode impedance needed to be assigned to a surface and not to the bulk of the electrode. The bulk of a MIEC like LSF goes along with high electronic conductivity anyway. Due to the low thickness of the layer, also the ionic resistance becomes negligibly small. Therefore, an area-related resistance and capacitance were attributed to the interface between LSF and YSZ.

There were two reasons that that this impedance was assigned to the interface and not to the LSF surface:

- An impedance on the electrode surface would allow a high lateral current flow in the model. This would not reflect the real situation due to the low lateral ionic conductivity of the MIEC layer.

- The applied AC potential and ground potential were assigned to the electrode surface, too.

Thus, the electrode bulk was parameterized with a very high conductivity so that its resistivity became negligibly small in comparison to the surface reaction.

The Electric Currents module does not provide options for a chemical capacitance. Thus, the area specific interface capacitance was set such, that the absolute value equals the chemical capacitance which is equivalent if the across plane resistance is negligible.

The height of WE and CE were set to $50\,\mu\mathrm{m}$, the RE was parameterized with $10\,\mu\mathrm{m}$.

Reference electrode properties were modeled as follows: The surface between YSZ and LSF was parameterized with the same interface resistivity and capacitance as WE and CE. The reference electrode bulk was parameterized with an in-plane conductivity and the same relative permittivity as the other electrodes, since the

chemical capacitance was already integrated into the model via the interface capacitance. For further details, see section 4.1.2.

All simulations covered a frequency range from $10\,\mathrm{mHz}$ to $1\,\mathrm{MHz}$.

Table 3.2 shows the chosen values of the parameters.

Table 3.2: Physical properties in the 2D FEA Frequency Domain study

Material	Property	Value	Unit
LSF	conductivity σ_{LSF}	$10\,000$	$\frac{\mathrm{S}}{\mathrm{m}}$
	relative permittivity ϵ_{LSF}	3	-
YSZ	conductivity σ_{YSZ}	0.7	$\frac{\mathrm{S}}{\mathrm{m}}$
	relative permittivity ϵ_{YSZ}	50	-
interface	specific resistance ρ_{LSF}	$5 \cdot 10^{-4}$	$\Omega\,\mathrm{m}^2$
	specific capacitance C_{LSF}	20	$\frac{\mathrm{F}}{\mathrm{m}^2}$

σ_{YSZ} was derived from [43]. ϵ_{YSZ} was estimated on basis of [44, Fig. 1]. The values for the interface impedance, which resembles the oxygen exchange reaction, were derived from two-point measurements (see section 4.1.1). The value for ϵ_{LSF} was assumed small so that the negligibly small geometric capacitance of the electrode does not affect the results.

After building and parameterizing the model, a sine shaped alternating electric potential of $0.01\,\mathrm{V_{RMS}}$ was applied to the top surface of the counter electrode (boundary condition 1). The frequency of this AC signal was varied over the above mentioned range. Ground potential was applied to the surface of the working electrode (boundary condition 2). Boundary condition 3 was that all the outer edges of the model were insulating $\vec{n} \cdot \vec{J} = 0$.

After the simulation process, the current density was integrated over the surface of the working electrode to get the complex alternating current over the frequency range. Additionally, the electric potential of the reference electrode was extracted. The overall (two-point) impedances were calculated according to equation 3.1.

$$\underline{Z}_{2point}(f) = \frac{V_{applied}}{\underline{I}_{measured}(f)} = \frac{0.01\,\mathrm{V}}{\underline{I}_{measured}(f)} \tag{3.1}$$

Complex variables are marked with an underline. The three terminal impedances were calculated between working and reference electrode using equation 3.2.

$$\underline{Z}_{3\,point}(f) = \frac{\underline{V}_{ref}(f)}{\underline{I}_{measured}(f)} \tag{3.2}$$

$\underline{V}_{ref}$ ... Electric potential of reference electrode [V]

The impedance between counter and reference elctrode was calculated according to equation 3.3.

$$\underline{Z}_{3\,point\,CE\_RE}(f) = \frac{V_{applied} - \underline{V}_{ref}(f)}{\underline{I}_{measured}(f)} \tag{3.3}$$

Stationary FEA Models

The stationary solution of the DC case was used to calculate the geometric (i.e. dielectric) capacitance of geometrically non-trivial electrode alignments. The capacitance C of a certain electrode alignment can be calculated according to equation 3.4.

$$C = \frac{Q}{V} = \frac{\int_{\mathcal{V}} \rho \, dV}{\int_{\mathcal{C}} \vec{E} \, ds} \tag{3.4}$$

where

Q ... Electric charge within electrode volume $\mathcal{V}$ [C]

V ... Applied voltage [V]

ρ ... Electric charge density $[\frac{C}{m^3}]$

$\vec{E}$ ... Electric field intensity $[\frac{V}{m}]$

$\mathcal{C}$ ... Any curve from one electrode surface to the other electrode surface that does not contain singularities (e.g. as a consequence of electric charges)

The stationary models were simulated in 2D rotationally symmetric. The geometry was embedded in air. Only two electrodes were implemented, so that solely the capacitance between those was evaluated without any external perturbation. For example the model that was used to calculate the capacitance between WE and CE did not contain a RE. Apart from air, YSZ and Pt at $635\,^{\circ}$C were defined.

Pt served as electrode material. For numerical reasons, zero could not be assigned to a property, instead a value of $1 \cdot 10^{-7}$ was used. All properties are outlined in Table 3.3.

Table 3.3: Physical properties in the 2D FEA Stationary study

Material	Property	Value	Unit
LSF	conductivity σ_{air}	$\rightarrow 0$	$\frac{S}{m}$
	relative permittivity ϵ_{air}	1	-
YSZ	conductivity σ_{YSZ}	$\rightarrow 0$	$\frac{S}{m}$
	relative permittivity ϵ_{YSZ}	50	-
Pt	conductivity ρ_{Pt}	$1.4 \cdot 10^6$	$\frac{S}{m}$
	permittivity ϵ_{Pt}	$\rightarrow 0$	-

The ring geometry was simulated rationally symmetrical with corresponding radii, so that the surfaces were kept constant. All electrodes (platinum sheets and reference electrodes) were modeled with a height of $20\,\mu m$.

After parameterizing the model, the surface of one electrode was assigned to ground potential and the other electrode surface was set to $1\,V$. Since the models only contain two dimensions and the electric charge concentrates at the surface for $t \rightarrow \infty$ due to electrostatic repulsion, equation 3.4 can be simplified to equation 3.5.

$$C = \frac{Q}{V} = \frac{\int_{\mathcal{S}} \rho_s * 2 * r * \pi \, ds}{V} \tag{3.5}$$

where

$\mathcal{S}$ ... Electrode surface

ρ_s ... Electric surface charge density $[\frac{C}{m}]$

r ... Radius [m]

4 Results and Discussion

First, some results of measurements and calculations are presented, that were necessary to acquire certain physical properties for simulations. Those evaluations are presented in section 4.1. The subsequent part 4.2 deals with the understanding and identification of error and artifact sources and to which extent they apply to the ring geometry. Section 4.3 contains further investigations on sample geometries that were already introduced in literature (microelectrode and rectangle geometry). The final part 4.4 presents results to our optimized three-point geometry, the single wing geometry.

4.1 Acquirement of Simulation Parameters

In order to conduct simulations, some measurements and calculations needed to be performed.

4.1.1 Electric and Dielectric Properties of LSF

In order to check results originating from 3-terminal measurements for plausibility, conventional 2-point measurements were conducted. The specific resistance and chemical capacitance of LSF (ρ_{LSF}, C_{LSF}) were the physical quantities that were derived from these measurements. The geometry of the samples was introduced in section 3.1.1. The two-point samples were prepared and measured as described in sections 3.2.1 and 3.2.2. Figure 4.1 shows the measured impedance spectrum of a 2-point sample. The measured spectrum was fitted with an electrolyte resistance and a serial Gerischer-element. The inductive high frequency data points arising from cable inductances were excluded from that fit. The results of the fitted elements are outlined in Table 4.1. It was derived from [43] that the YSZ resistance at
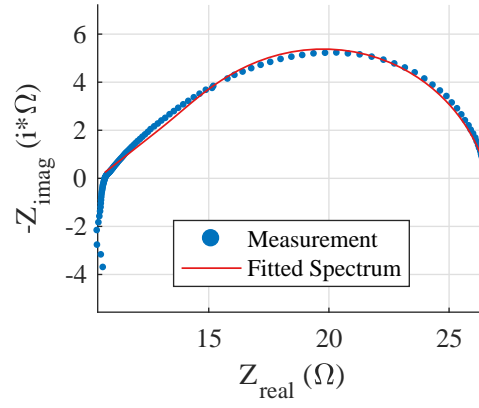
Figure 4.1: Impedance spectrum of a 2-point sample with porous LSF electrodes, and a YSZ electrolyte, 635 °C

Table 4.1: Fitted elements of 2-point impedance spectrum

Element	Value	Unit	Error[%]
R_s	10.65	Ω	0.196
GE_T	0.009 217 9		0.348 12
GE_P	47.97		0.745 03

635 °C in a typical macroscopic electrode measurement with an electrode surface of $1\,\text{cm}^2$ and a YSZ height of $0.5\,\text{mm}$ should be $6.5\,\Omega$. Given that the measured electrolyte resistance was $10.65\,\Omega$, we conclude that only $\frac{10.65\,\Omega}{6.5\,\Omega} - 1 = 63.85\%$ of the electrode surface was polarized. This means that the measured electrode impedance arises from only around 60 % of the actual electrode surface. The real polarization resistance therefore needs to be corrected by a factor of 0.6385. To get the values for the polarization resistance and chemical capacitance out of the Gerischer element, the following equation 4.1 was used [45] [46, page 29].

$$Z_{imag} = -\frac{R_{chem}}{\sqrt{2}}\sqrt{\frac{\sqrt{(\omega * t_{chem})^2 + 1} - 1}{(\omega * t_{chem})^2 + 1}} \tag{4.1}$$

R_{chem} ... Polarization resistance of the electrode $[\Omega]$
t_{chem} ... Characteristic time constant $[\text{s}]$

The imaginary part of the measured impedance was fitted to equation 4.1, using the angular frequency ω as independent variable. A Levenberg-Marquardt fit returned the values $R_{chem} = 15.42\,\Omega$ and $t_{chem} = 0.021\,65\,\text{s}$. The chemical capacitance can then be extracted using equation 4.2 [see 45].

$$C_{chem} = \frac{t_{chem}}{R_{chem}} \tag{4.2}$$

which results in a capacitance of $1.404\,\text{mF}$. These values now have to be corrected by the fraction of the active electrode surface 0.6385. Furthermore the two-terminal impedance contains the electrode impedance two times in series, therefore the resistance must be divided by 2 and the capacitance must be multiplied by 2 to obtain the values for one single element. This results in the values $R_{pol,\,\text{electrode}} = 4.922\,\Omega$ and $C_{chem,\,\text{electrode}} = 1.793\,\text{mF}$.

As the polarization resistance and the chemical capacitance change with other factors like the oxygen partial pressure and the electric potential, the orders of magnitude are more significant than the exact values. Subsequently, the specific polarization resistance of LSF was set to $5\,\Omega\,\text{cm}^2$ and the specific chemical capacitance was set to $2\,\frac{\text{mF}}{\text{cm}^2}$.

The properties of the measured porous electrodes are in the same order of magnitude like the properties of well prepared LSF thin films. This guaranteed the plausibility of using the results of the porous electrodes for the thin film simulations.

4.1.2 In-Plane Conductivity and Permittivity of LSF

To conduct the finite elements simulation of the ring geometry, an in-plane conductivity of LSF was required. Therefore, a Van der Pauw sample was produced and measured according to sections 3.2.1 and 3.2.2. One temperature cycle from $600\,°C$ to $680\,°C$ and back to the start temperature was conducted. The conductivities at $630\,°C$ and $640\,°C$ were identified and related to an electrode height of $10\,µm$[1]. A mean value was calculated to approximate the conductivity at $635\,°C$. Table 4.2 summarizes the results. The mean value is $66.292\,\frac{S}{m}$. The in-plane conductivity of

Table 4.2: In-plane conductivity of porous LSF according to Van der Pauw measurements

In-plane conductivity σ_{IP} $[\frac{S}{m}]$	Temperature [°C]
66.73	630
66.71	640
66.05	640
66.68	630

the LSF reference electrode was parameterized accordingly in the finite elements simulations.

---

[1]The exact electrode height is hard to determine for porous electrodes that are geometrically not well defined. However, this doesn't matter for the current evaluations, because only the absolute conductivity of the layer is relevant. As long as the reference electrode height in the FEA model is the same as the related value in these calculations, the absolute value is correct

4.1.3 Numerical Capacitance Calculations of the Ring Geometry

The coupling capacitances between electrodes do not only originate from measuring probes, but also from geometric capacitances of the sample. The capacitance of these non-trivial alignments cannot be calculated according to simple formulae with sufficient accuracy. Therefore, the geometric capacitances were calculated numerically according to section 3.3.2.

The ring geometry sample features two different intrinsic geometric capacitances. The most obvious one is the capacitance between working and counter electrode, in which the platinum sheets of the measuring apparatus act as capacitor-electrodes. The dielectric in between is mostly the electrolyte ($\epsilon_r = 50$) and partly air ($\epsilon_r = 1$). Apart from this capacitance, the reference electrode also exhibits a capacitance to both, working and counter electrode ($C_{geo,\,WR}$ and $C_{geo,\,CR}$). Since the reference electrode is placed at center height, $C_{geo,\,WR} = C_{geo,\,CR}$. Table 4.3 summarizes the capacitances that were calculated according to equation 3.5. At first sight, it

Table 4.3: Geometric capacitances of the ring geometry sample

$C_{geo,\,WR}$, $C_{geo,\,CR}$	$21.94\,\mathrm{pF}$
$C_{geo,\,WC}$	$14.38\,\mathrm{pF}$

might be surprising that the capacitance involving the reference electrode exceeds the capacitance of the spatially further extended platinum sheets. One reason for this is the smaller distance from electrode to electrode. The other reason is derived as follows.

The capacitance is defined by the quotient of the electrostatically induced charge per applied voltage. According to Maxwell, the source of the electric displacement field $\vec{D}$ is the charge density ρ ($\vec{\nabla}\cdot\vec{D} = \rho$). Thus, the electric charge within a defined volume $Q(\mathcal{V})$ equals the electric displacement flux over the edge of the volume $\Psi(\partial\mathcal{V})$ ([see 40, page 163]). If the volume $\mathcal{V}$ is defined as one of the capacitor-electrodes, the integral of the electric displacement field over the electrode surface returns the charge ($\int_{\partial\mathcal{V}} \vec{n} \cdot \vec{D}\, dA = Q(\mathcal{V})$). Therefore, a high electric displacement field along the electrode edges ultimately leads to a high capacitance.

Figures 4.2 and 4.3 show the distribution of the electric displacement field $|\vec{D}|$ for the axisymmetric 2D-simulations. In Figure 4.2 it is visible that $|\vec{D}|$ is almost exclusively concentrated within the YSZ sample due to its higher permittivity. The geometric capacitance originates - not very surprisingly - mainly from the dielectric properties of YSZ.

More importantly, if one compares the maximum values of $|\vec{D}|$ of the WE-CE alignment in Figure 4.2b to the maxima of the RE-WE alignment in Figure 4.3b, one can find that the values in the second scenario are about one order of magnitude higher. Here the electric displacement field reaches values up to $4 \cdot 10^{-6} \frac{\mathrm{A\,s}}{\mathrm{m}^2}$ close to the edges (depicted in dark violet), whereas the maxima in the WE-CE alignment only add up to $4 \cdot 10^{-7} \frac{\mathrm{A\,s}}{\mathrm{m}^2}$. The increased field intensities along the edges stem from high concentrations of electrostatically induced charge resulting in the high capacitance of the RE-WE alignment.

(a) $|\vec{D}|\,(\frac{\mathrm{A\,s}}{\mathrm{m}^2})$ around the sample (b) $|\vec{D}|\,(\frac{\mathrm{A\,s}}{\mathrm{m}^2})$ around the sample, zoomed in
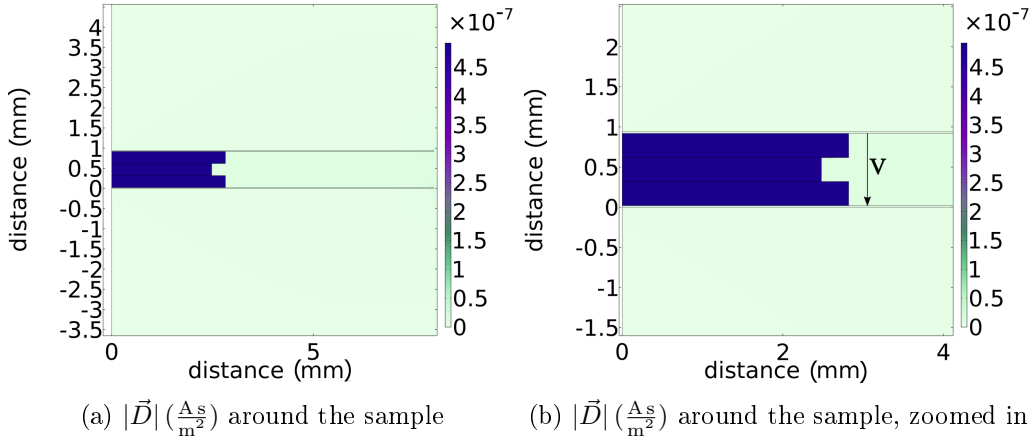
Figure 4.2: Ring geometry: Magnitude of the electric displacement field $|\vec{D}|(r,z)$ in $\frac{\mathrm{A\,s}}{\mathrm{m}^2}$ for working to counter electrode (WE-CE) capacitance

(a) $|\vec{D}|\,(\frac{\mathrm{A\,s}}{\mathrm{m^2}})$ around the sample
(b) $|\vec{D}|\,(\frac{\mathrm{A\,s}}{\mathrm{m^2}})$ around the sample, zoomed in
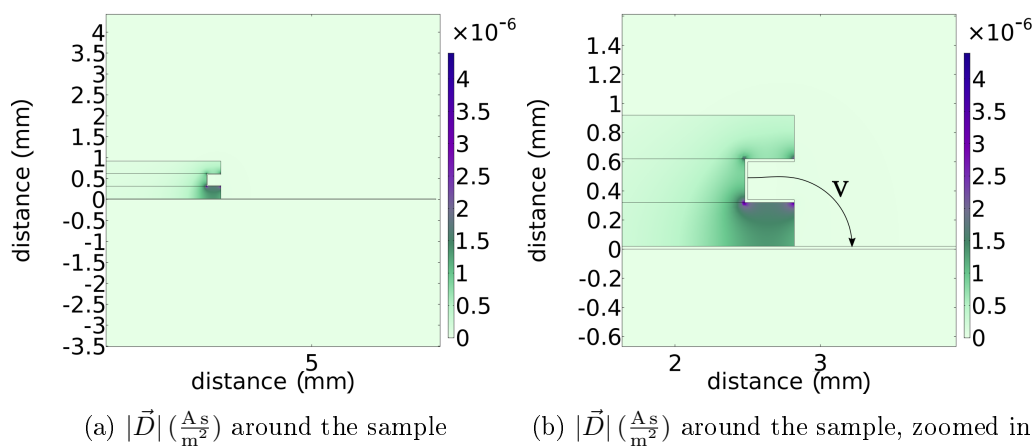
Figure 4.3: Ring geometry: Magnitude of the electric displacement field $|\vec{D}|(r,z)$ in $\frac{\mathrm{A\,s}}{\mathrm{m^2}}$ for reference to working/counter electrode (RE-WE, RE-CE) capacitance

4.2 Error and Artifact Sources

Three-point measurements of ring geometry samples often featured a semicircle that preceded the working electrode semicircle in the impedance spectrum. The transition from the artifact semicircle to the electrode semicircle was often accompanied by loops. Typical distorted impedance spectra are depicted in Figure 4.4.
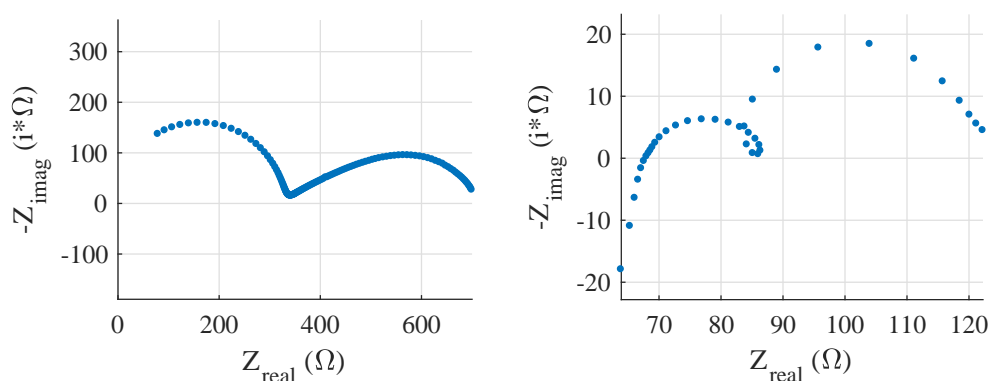
(a) High-frequency artifact semicircle followed by the porous WE feature

(b) Mid-frequency semicircle with a loop at the low frequency intercept; anodic Bias of 450 mV

Figure 4.4: Typical artifact impedance spectra taken from ring geometry samples

Figure 4.4a shows a three-terminal impedance spectrum of a sample with porous LSF-Pt as electrodes. The spectrum was taken at 585 °C at an oxygen partial pressure of 10 mbar. There was no bias applied in this case. The high frequency semicircle is considered to be an artifact because it disappears in the corresponding two-terminal spectrum. Moreover, the circle shows almost no depression which is rather unusual for a semicircle arising from electrochemical effects. Its peak frequency is at around 450 kHz. The corresponding two-termianl spectrum is depicted in Figure 4.5.

The spectrum depicted in Figure 4.4b was taken from a sample that had thin film LSF working and counter electrodes. The reference electrode was also made out of porous LSF-Pt. The measurement was taken in 50 vol% O_2 and a temperature
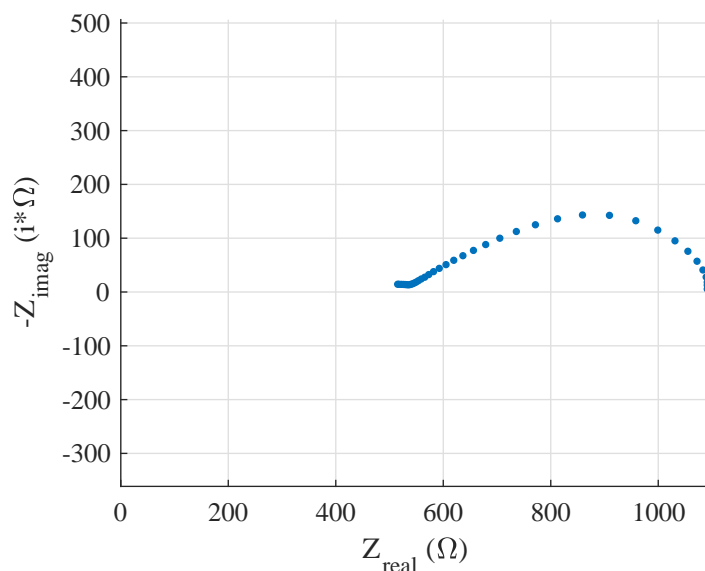
Figure 4.5: Two-point impedance spectrum of the sample in Figure 4.4a

of 600 °C and a superposed anodic DC voltage of 450 mV was applied. The high frequency semicircle might be an interface feature, however it is likely that it is at least partly an artifact because of the loop in the transition range between the two arcs. This semicircle probably stems from another error source since it is more depressed (CPE-P of about 0.75) and its high frequency intercept is at a value that is likely to resemble the expected electrolyte resistance of about 50 Ω to 100 Ω. The peak frequency is at about 1 kHz which is also different from the artifact semicircle in Figure 4.4b.

The approach to identify the artifact origins was to check the list of known artifact sources in Table 2.1, whether one of the listed causes may apply in the cases above. First, the focus was laid on external influences.

4.2.1 Voltage Divider Effect between RE and Voltmeter

The voltage divider effect becomes crucial if the impedance of the reference electrode is in the same order of magnitude as the input impedance of the voltmeter
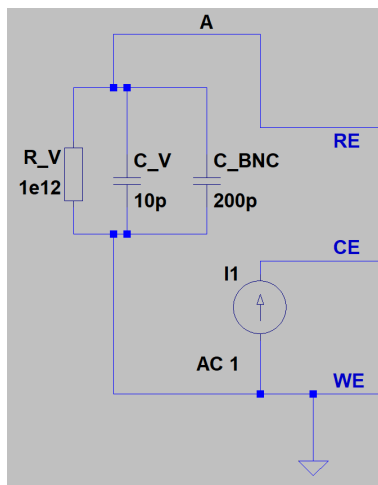
Figure 4.6: Model core

(see equation 2.6). In [24], it was shown that a small interface capacitance of a high-ohmic reference electrode causes inductive behaviour in the low frequency range. In this thesis, the inspected systems feature relatively low-ohmic LSF reference electrodes with chemical capacitances in the range of a few hundred µF to a few mF which clearly exceed the input capacitance of typical voltmeters by several orders of magnitude. Thus, the voltage divider effect rather states a problem at high frequencies due to a lowered impedance of the voltmeter. The voltage divider effect was investigated by simulating the 3-point arrangement depicted in Figure 3.11 with $R_{pol} = 20\,\Omega$, $C_{WE} = C_{CE} = 330\,\mu F$ and $C_{RE} = 100\,\mu F$. The chosen values for the capacitances are rather low but still realistic so that the negative influence of this effect is maximized. The ideal voltmeter in Figure 3.12 was replaced by a simplification of the potentiostat Novocontrol POT/GAL 30 V/2 A. The potentiostat was modeled as a parallel setup of its input resistance and input capacitance which were taken from the Manual of the potentiostat (see Figure 4.6). The resistance R_V was $1\,\mathrm{T}\Omega$ and the capacitance C_V had a value of $10\,\mathrm{pF}$. The input impedance was complemented by an additional parallel capacitance C_{BNC} of $200\,\mathrm{pF}$ which is a typical value for the capacitance between the core and the shield of a 2 m coaxial voltage cable. This additional capacitance adds up to the
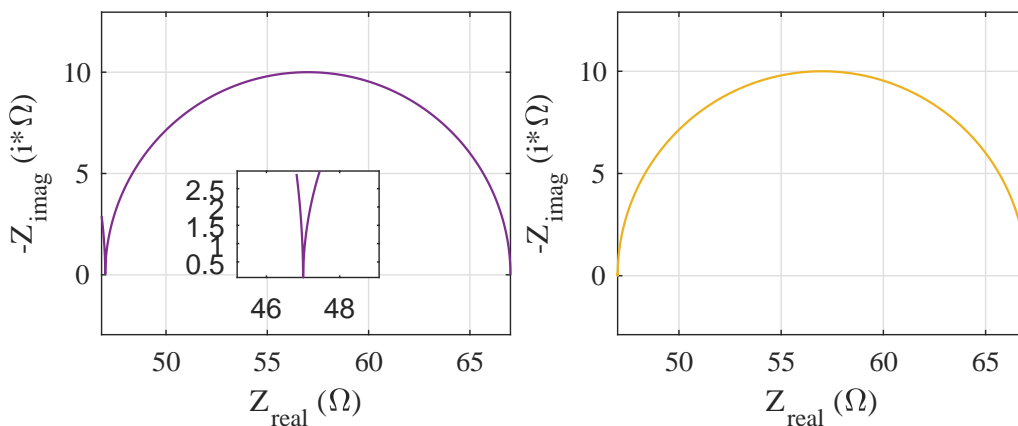
(a) without driven shields; the high frequency arc arises from the voltage drop across the voltmeter input impedance and C_{BNC}
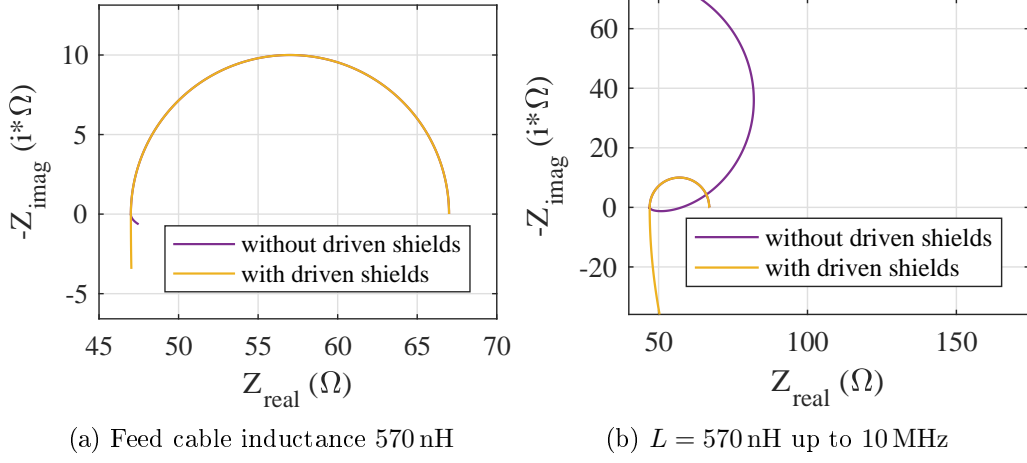
(b) with driven shields

Figure 4.7: Voltage divider effect: Simulated spectra of a 3-point circuit ($R_{pol} = 20\,\Omega$, $R_{elyte} = 47\,\Omega$, $C_{WE} = C_{CE} = 330\,\mu F$, $C_{RE} = 100\,\mu F$) with the real input impedance of the potentiostat

input capacitance if the shield of the coaxial voltage cable is grounded.

The voltage divider effect can cause artifacts in the high frequency range. As visible in Figure 4.7a, an additional high frequency semicircle starts to emerge. The semicircle is caused by the input impedance of the voltmeter and the parallel C_{BNC}, which is the capacitance between the coaxial cable core and its shield. The latter is a big impact source, as it is a quite big capacitance. This capacitance can be cancelled out by actively shielding the reference electrode BNC cable. This measure forces the shield of the BNC cable on the same potential like its core, which effectively eliminates the capacitance. Figure 4.7b shows the spectrum if the capacitance C_{BNC} is eliminated by active shielding. This impedance spectrum shows that the influence of the voltage divider effect can be avoided in the simulated frequency range, if one actively shields the reference electrode BNC cable.

However, depending on the measuring apparatus, one needs to take care if the BNC cables are grounded via the steel flange. If so, the shields of the cables are forced to equal potentials due to their electric connection. Thus, the "Driven

(a) Feed cable inductance 570 nH   (b) $L = 570\,\mathrm{nH}$ up to 10 MHz

Figure 4.8: Voltage divider effect: Simulated spectra of a 3-point circuit ($R_{pol} = 20\,\Omega$, $R_{elyte} = 47\,\Omega$, $C_{WE} = C_{CE} = 330\,\mu\mathrm{F}$, $C_{RE} = 100\,\mu\mathrm{F}$) with the real input impedance of the potentiostat, considering a feed cable inductance of 570 nH

Shields" option cannot be applied in this configuration.

In reality this artifact will be superposed by inductances originating from the feed cables. The value of the inductance L consists of the part arising from the coaxial BNC cables and from the probes inside the measuring apparatus. The inductance per unit length of the coaxial cables $L' = 250\,\frac{\mathrm{nH}}{\mathrm{m}}$ was calculated according to the wave resistance equation 2.7, whereas $Z_0 = 50\,\Omega$ was taken from the datasheet of the cable and $C' = 100\,\frac{\mathrm{pF}}{\mathrm{m}}$ is a typical value. The BNC cables were parameterized with a length of 2 m. The inductance of the measuring probes within the apparatus was calculated according to equation 2.8 to 70 nH. Therefore, the inductance of each feed cable was parameterized with 570 nH. The simulation results for this scenario are shown in Figure 4.8. Considering the regular frequency range up to 1 MHz, an inductive feature in the high frequency range arises (see Figure 4.8a). In case driven shields are not applied, the spectrum shows the beginning of an inductive loop. In case the driven shields are enabled, the feature is purely inductive without a loop, as can be seen in most measurements of a real systems (e.g. in Figure 4.4). This means that in the high frequency region the feed induc-

tance is the dominant error source, possibly covering other measurement errors. In case the frequency range is extended to 10 MHz, the combination of feed inductance and voltage divider leads to serious errors, as depicted in Figure 4.8b. The impedance spectrum without driven shields shows a capacitive arc following the small inductive feature, whereas the spectrum for a scenario with driven shields remains inductive at higher frequencies.

To sum up, the voltage drop across the voltmeter and C_{BNC} leads to an additional high frequency semicircle that has its HF intercept at $0\,\Omega$, if C_{BNC} is not eliminated (see simulated spectrum in Figure 4.7a). This semicircle resembles the artifact semicircle in Figure 4.4a. However, the peak frequencies are separated by about 1.5 orders of magnitude (500 kHz and 20 MHz). Furthermore, the artifact semicircle vanishes when considering the inductances that definitely exist in the real system. Therefore, the voltage divider effect can be ruled out as the origin of the artifacts depicted in Figure 4.4.

4.2.2 Feed Cable Inductance and Capacitance

To investigate the influence of the feed cable inductances and capacitances, worst case assumptions were made. Therefore, unshielded feed cables with a cross-sectional area of $22\,\text{mm}^2$, a length of $2\,\text{m}$ and a center-to-center distance of $2\,\text{mm}$ were assumed and connected to the ideal three point circuit in Figure 3.11. According to equations 2.8 and 2.9, $L = 1.6\,\mu\text{H}$ and $C = 28\,\text{pF}$. The alignment was measured as described in section 3.2.5 and simulated according to chapter 3.3.1, whereas the transmission line elements were subdivided into three parts, each with a third of the total value.

The impedance spectra are almost identical, as can be seen in Figure 4.9. Moreover, both impedance spectra only show the electrode semicircles without any artifacts. Minor inductive behaviour can be identified in the high frequency region. However, neither a loop, nor an additional semicircle can be reproduced by long feed cables. This potential artifact source can therefore be excluded in casu.
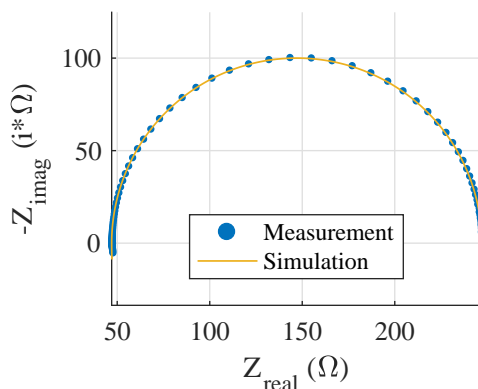
Figure 4.9: Impedance spectrum of a 3-point circuit with $2\,\mathrm{m}$ feed cables; $10\,\mathrm{mHz}$ - $1\,\mathrm{MHz}$

4.2.3 Amperemeter-Bypass by Capacitive Coupling to External Shielding

The bypass of the amperemeter as described in [30] is an effect that can be excluded for the artifact sources investigated in this thesis. The reason for this is that the capacitances in the inspected electrochemical systems are chemical capacitances in the range of a few hundred µF to a few mF. Those exceed the coupling capacitance to the external shielding C_m (in the range of a few pF) by several orders of magnitude and therefore the current through the box capacitance C_m will always be negligibly small in comparison to the current flowing through the electrochemical sample.

4.2.4 Bandwidth of Current-to-Voltage Converter Exceeded

As described in section 2.1.4, high frequencies in combination with a high closed loop gain of the current-to-voltage converter that measures the electric current can lead to an apparent inductance. Therefore, the current measurement working principle of the used measuring setup (potentiostat: Novocontrol POT/GAL $30\,\mathrm{V}/2\,\mathrm{A}$, frequency response analyzer (FRA): Novocontrol Alpha A9 Frequency Analyzer)

was examined. According to the potentiostat's manual, the current measurement for low currents ($\approx 20\,\text{mA}$ or lower) functions exactly as described in section 2.1.4. In the case at hand, the applied voltage is $10\,\text{mV}_{\text{RMS}}$ and minimal impedances are in the range of $10\,\Omega$. Therefore the maximum currents are in the range of $\frac{0.01\,\text{V}}{10\,\Omega} = 1\,\text{mA}$, which means that the measurements in casu definitely feature low currents.

According to the FRA's manual, the feedback resistor R_f is variable and automatically adjusted to a favourable value by the Alpha A9 Frequency Analyzer. There is no exact information about which operational amplifier is used or what is the value of its Gain Bandwidth product. However, it is ensured in the manual that even for low currents in the magnitude of a few fA, the device features a bandwidth up to $10\,\text{MHz}$ which is above the highest measured frequency. This is achieved by the appropriate adjusting of R_f. Therefore, this error source can also be excluded as cause of the artifacts in Figure 4.4.

4.2.5 Three-Terminal Transfer Characteristic

The first step in investigating the issue of the three-terminal transfer characteristic as described in section 2.1.4, was to assume and calculate realistic values for an electrochemical system and the equivalent elements of the Fletcher circuit according to [27] were identified. According to section 4.1.1, the specific resistance of LSF at $635\,^{\circ}\text{C}$ in air can be assumed with about $5\,\Omega\,\text{cm}^2$. For an electrode area of $0.25\,\text{cm}^2$, the polarization resistance $R_{pol} = R_{WE} = R_{CE} = 20\,\Omega$. The reference electrode resistance was assumed 50 times higher, i.e. $1\,\text{k}\Omega$.

The capacitances between the electrodes originate from two parts: The measuring probe capacitances were calculated according to equation 2.9 and emerge between all the electrodes. The second part arises from intrinsic geometric capacitances that were calculated using finite elements analysis (see section 3.3.2 and 4.1.3). All the values are outlined in Table 4.4. On basis of these values, the elements of the equivalent 2-point circuit according to Fletcher [27] were calculated. The equivalent circuits were then simulated for a frequency range from $10\,\text{mHz}$ to $1\,\text{MHz}$ to

Table 4.4: Values of a realistic electrochemical system

Element	Value	Unit
R_{pol}	20	Ω
R_{RE}	1000	Ω
C_{WR}	24.5	pF
C_{CR}	24.5	pF
C_{WC}	16.9	pF
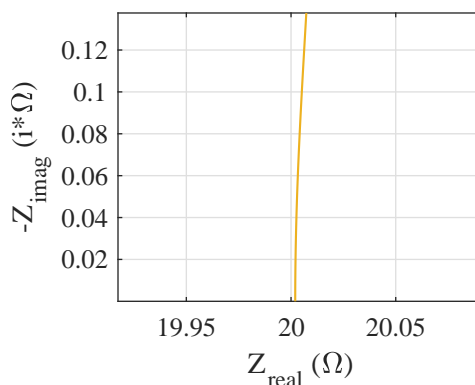
Figure 4.10: Simulated spectrum (10 mHz - 1 MHz) of the Fletcher circuit - $R_{pol} = 20\,\Omega$, $R_{RE} = 1000\,\Omega$

quantify possible non-ideal behaviour or measurement errors. The Fletcher equivalent circuit only represents electrochemical systems without electrolyte and purely ohmic polarization resistances of the electrodes. This ideal configuration should therefore only show a point on the real axis of the impedance plot with the value of the working electrode resistance. However, as a result of coupling capacitances between electrodes, artifacts arise. Figure 4.10 shows an impedance spectrum for polarization resistances of $20\,\Omega$ and a reference electrode resistance of $1\,\mathrm{k\Omega}$. As one can see, there is not only a point in the spectrum, but also a small spike. The magnitude of this distortion is in a rather small scale. It shows that additional features can emerge out of coupling capacitances, though.

However, if all resistances are multiplied by a factor of 100 - which is realistic for lower oxygen partial pressures or temperatures - conditions change dramatically.

(a) $R_{pol} = 2\,\mathrm{k\Omega}$, $R_{RE} = 100\,\mathrm{k\Omega}$ (b) $R_{pol} = 200\,\mathrm{k\Omega}$, $R_{RE} = 10\,\mathrm{M\Omega}$
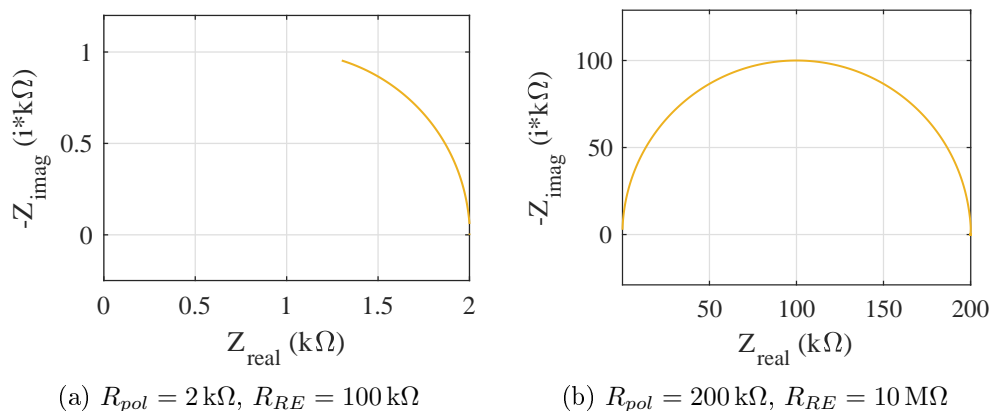
Figure 4.11: Simulated impedance spectra (10 mHz - 1 MHz) of Fletcher circuits (see Figure 2.10)

Figure 4.11a shows the impedance spectrum for $R_{pol} = 2\,\mathrm{k\Omega}$ and $R_{RE} = 100\,\mathrm{k\Omega}$. The figure shows a semicircle of an RC-element, which originates from a purely artificial background. If one regards the Fletcher equivalent circuit in Figure 2.10, the result is easy to interpret. For low frequencies, the inductance L_1 is high enough to act as a serial short circuit to the working electrode WE, whereas the capacitances C_1 and C_2 block electric current due to their high reactances. The effective low frequency impedance therefore is limited to R_{WE}. For high frequencies, the reactance of C_1 becomes smaller and thus represents a parallel path for the electric current. What remains effectively is an RC-element, consisting of R_{WE} and C_1. If one fits the impedance spectrum with an RC-element and a serial resistance, the fitted RC values are $R = 2000\,\Omega$ and $C = 58.3\,\mathrm{pF}$, which represent *exactly* the simulation parameters of R_{WE} and C_1. The peak frequency of this artifact semicircle can be shifted by further scaling up the resistances R_{WE}, R_{CE} and R_{RE}. Figure 4.11b shows the artifact semicircle for $R_{pol} = 200\,\mathrm{k\Omega}$ and $R_{RE} = 10\,\mathrm{M\Omega}$. In this figure, the whole artifact semicircle resulting from the R_{WE}-C_1 parallel circuit is visible, although the frequency range still ends at 1 MHz.

This artifact also arises for real solid electrochemical systems, where polarization impedances are RC-elements and an electrolyte resistance exists. Figure 4.12 shows a two-terminal and a three-terminal impedance spectrum for a ring geometry sam-
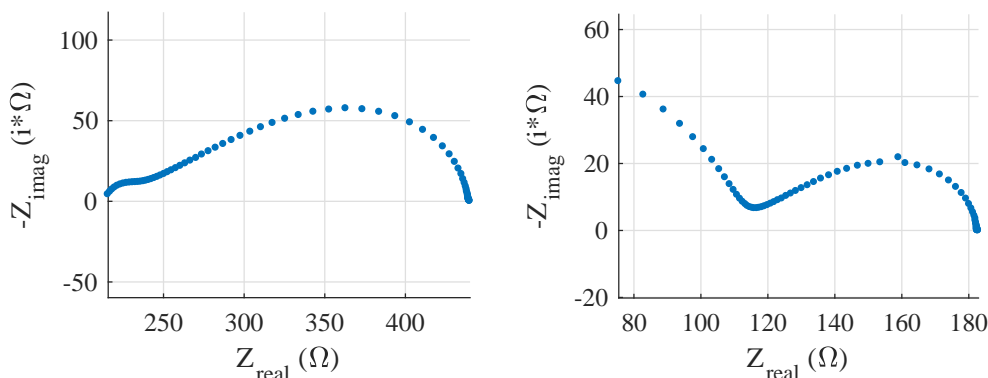
(a) Two-terminal spectrum without the artifact semicircle

(b) Three-terminal spectrum with the artifact semicircle (the outlying data point at the Gerischer peak is an interspersal from the grid frequency 50 Hz)

Figure 4.12: Ring geometry - porous LSF-Pt electrode in 21 vol% O_2

ple measured at 585 °C in synthetic air. The electrodes were a mixture of LSF and platinum. This electrode material had a higher impedance than the electrodes where LSF and platinum were applied separately, as described in section 3.2.1. The three-terminal impedance spectrum in Figure 4.12b features an artifact semicircle at high frequencies, while this semicircle disappears in the two-terminal measurement in Figure 4.12a. Both spectra show a characteristic low frequency Gerischer-type feature of a porous electrode.

These investigations already show some very important results. Ring geometry systems with high-impedance electrodes (e.g. at low oxygen partial pressures, lower temperatures or high-ohmic materials) may lead to an artifact semicircle in the high frequency range. This distortion is caused by the 3-terminal transfer characteristic of systems with significant coupling capacitances. The coupling capacitances in this geometry mainly originate from the geometric capacitances between WE to RE and CE to RE, but also from WE to CE. These are purely intrinsic geometric capacitances that cannot be circumvented in this geometry. Active shielding of the measuring probes would only eliminate the coupling capacitances arising from the cables, which are about one order of magnitude smaller than the intrinsic ca-

pacitances. The ring geometry is therefore only restrictedly suitable for 3-point measurements with high-impedance electrodes.

When comparing the artifact semicircles arising from coupling capacitances to the artifact semicircle depicted in Figure 4.4a, one can find that the scenarios are very similar to each other. The resistances are in the same order of magnitude, the frequency range of the semicircles is quite high ($f > 10\,\text{kHz}$) and the high frequency intercept is at $0\,\Omega$. Moreover, the artifact semicircle in Figure 4.4a is almost ideal ($CPE\text{-}P \approx 0.95$) and disappears in the two-terminal measurement setup. The conclusion is that the origin of the measured artifact semicircle in Figure 4.4a are the coupling capacitances and the three-terminal transfer characteristic found by Fletcher [27].

4.2.6 Intrinsic Error Sources

Apart from the coupling capacitances arising from the sample geometry, the focus of the previous inspections was on external error sources arising from the measuring equipment. The general conclusion so far was that these influences matter, however they are mostly expected at higher frequencies. The next step was to investigate the intrinsic error sources listed in Table 2.1.

Known Error Sources

For these inspections, a finite elements model was built according to section 3.3.2 with the properties outlined in Table 3.2. The reference potential was tapped at the edge of the reference electrode exactly at center height.
The most important insight can be derived from the current density within the sample depicted in Figure 4.13. Figure 4.13a shows the current distribution for a frequency of $1\,\text{MHz}$, whereas Figure 4.13b refers to a frequency of $0.01\,\text{Hz}$.

The current density at the electrode surfaces is relatively homogeneous. Therefore, the inhomogeneous current density issue as described in section 2.1.4 does not play
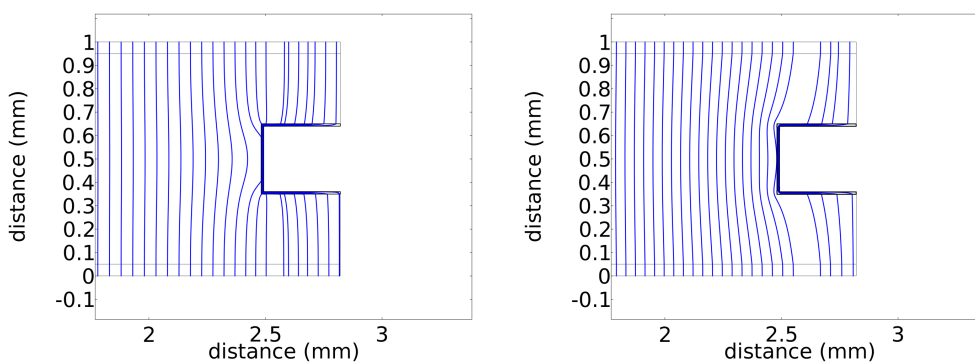
(a) primary current distribution ($\omega \to \infty$)   (b) secondary current distribution ($\omega \to 0$)

Figure 4.13: Current distribution within and around the RE of the symmetric ring geometry sample; the density of the blue current lines reflects the current density (magnitude controlled)

a role. Since the reference potential is tapped exactly at center height and WE and CE feature the exact same properties, the change of current distribution does not distort the results, either. This is due to the fact, that the reference potential is constantly at $5\,\text{mV}$ and the RE equipotential line does not shift. Thus, the change of the reference potential does not distort the impedance spectra in this setup as described in 2.1.4.

Short Circuit through the RE

None of the potential error sources listed in Table 2.1 applied to the ring geometry. However, there is one essential error source, that can be extracted from the current density. It is clearly visible, that there is a strong current flow through the reference electrode. This residues from the potential that is applied from bottom to top and the RE is spatially extended in this direction. Thus, a potential spread across the upper and lower edge of the reference electrode occurs. This voltage combined with the high in-plane conductivity of the porous LSF causes the current through the reference electrode, even though there is the barrier of the ion-electron exchange reaction in the low frequency case.
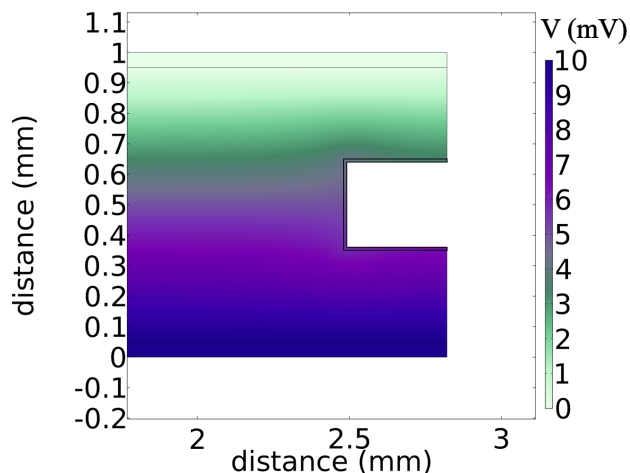
Figure 4.14: Symmetric ring geometry sample: Magnitude of the primary ($\omega \to \infty$) electric potential $|V|(r,z)$ in mV within and around the RE

A similar result was found for reference electrodes in Li-ion battery cells with a liquid electrolytic solution in [47]. That study already showed that a part of the electrolyte is short-circuited by a well conducting RE that is placed in or close to the main current path.

Figure 4.14 shows the potential distribution within the cell. This figure illustrates the potential spread between the outer edges of the reference electrode, which causes the short circuit through the RE. The potential difference is about $3\,\mathrm{mV}$ which equates $30\,\%$ of the total applied voltage.

The 3-point impedance spectrum extracted from the finite elements simulation is depicted in Figure 4.15. The spectrum was fitted with a resistor representing the electrolyte and a serial RC-element. The values of the fitted elements are outlined in Table 4.5. The working electrode set values are $R = 20\,\Omega$ and $C = 0.5\,\mathrm{mF}$. However, the apparent values extracted from the fit are $R_{apparent} = 21.79\,\Omega$ and $C_{apparent} = 0.437\,\mathrm{mF}$. This means that there is an error of about $10\,\%$.

This error is caused by the *short circuit effect* through the RE. The ohmic-capacitive RE represents an additional ohmic-capacitive current path in parallel to the by-
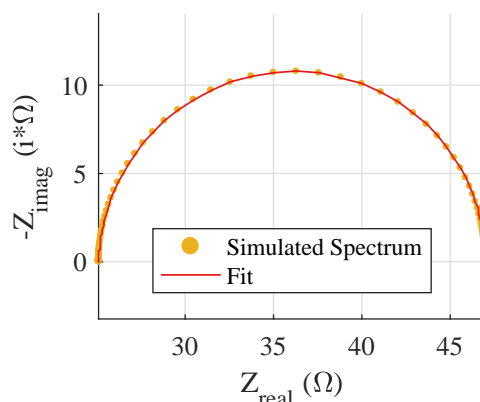
Figure 4.15: Simulated 3-terminal spectrum of a symmetric ring geometry sample with the reference potential extracted at center height

Table 4.5: Fitted elements of the three-point impedance of the ring geometry

Element	Apparent Value	Set Value
$R_{electrolyte}$	$25.17\,\Omega$	$25\,\Omega^{a}$
R	$21.79\,\Omega$	$20\,\Omega$
C	$0.437\,\mathrm{mF}$	$0.5\,\mathrm{mF}$

[a]lateral resistance neglected; the fitted value is distorted by the parallel polarization resistance of the RE

passed part of the electrolyte. This provokes an additional RC-semicircle. However, the peak frequency of this arising semicircle is very close to the one of the electrode semicircle and is therefore not visible in the spectrum. As a consequence, the working electrode semicircle is enlarged and the apparent impedance is bigger than it should be. The follow up section on the equivalent network of the short circuit effect provides a more detailed explanation of this situation.

This *short circuit effect* was verified as distortion source by simulating a scenario with reversible ($R_{pol} = 0$) working and counter electrodes. In this scenario, only a small semicircle appeared (see Figure 4.16). The semicircle in this figure was again fitted with an RC-element, returning the values $R_{short} = 1.725\,\Omega$ and $C_{short} = 2.774\,\mathrm{mF}$. R_{short} represents quite precisely the deviation of the set value $20\,\Omega$ from the apparent value $21.79\,\Omega$ outlined in Table 4.5. Since the WE RC-

element and the short circuit RC-element exhibit equal properties, i.e. similar peak frequencies[2], the overall capacitance C_{tot} can be approximated with a series circuit of $C_{WE} = 0.5\,\mathrm{mF}$ and $C_{short} = 2.774\,\mathrm{mF}$. This results in an overall capacitance that can be calculated according to equation 4.3.

$$C_{tot} = \frac{C_{WE}C_{short}}{C_{WE} + C_{short}} \tag{4.3}$$
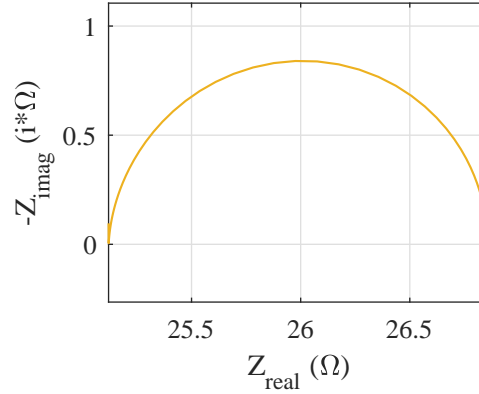
Figure 4.16: Simulated 3-terminal spectrum of a symmetric ring geometry sample with reversible WE and CE ($R_{pol} = 0$); the semicircle is caused by the short circuit effect

The total capacitance C_{tot} of this circuit is $0.424\,\mathrm{mF}$ which also comes quite close to the apparent capacitance $C_{apparent}$ $0.437\,\mathrm{mF}$ of the symmetric ring geometry sample with non-reversible electrodes. The remaining deviation results from the different current distributions in the particular scenarios. Thus, the error in the electrode semicircle can be explained by the short circuit through the RE.

This reveals that the short circuit effect is a crucial error source, since it produces a significant error, however the distortion is not visible in the spectrum. An equivalent network model of the short circuit effect is presented in the follow up section.

---

[2]similar and not equal peak frequencies due to different geometries

Equivalent Network Model of the Short Circuit Effect

The electrode semicircle and the loop depicted in Figure 4.4b could not have been reproduced, so far. However, one needs to consider that the capacitances of the real WE and RE usually differ from each other for several reasons like applied bias, used material and electrode structure (thin film or porous). In order to show that this difference matters, an LTSPICE-model representing a 1D-model of the short circuit effect as shown in Figure 4.17 was built.
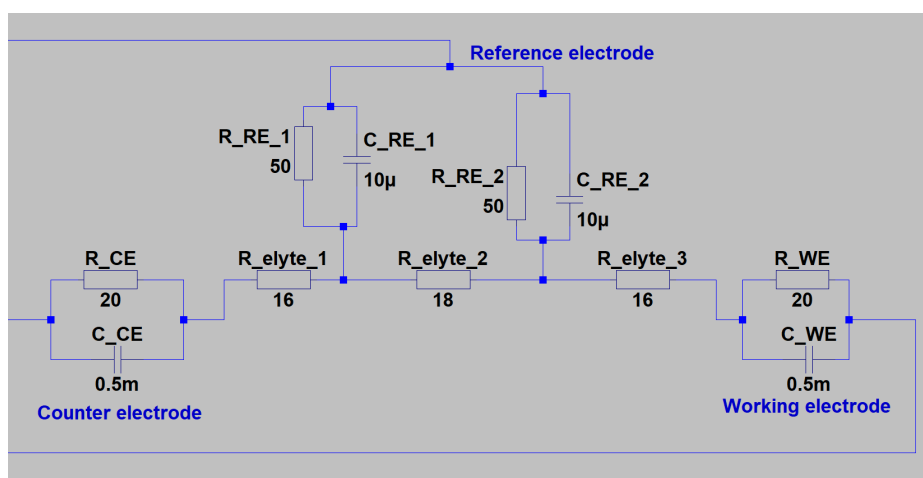
Figure 4.17: LTSPICE-model of the short circuit effect (element parameters for a symmetrical reference electrode)

The model contains WE and CE properties that are the same as in the finite elements simulations. The electrolyte resistances ($16\,\Omega$ and $18\,\Omega$) equate YSZ resistances at $635\,°\mathrm{C}$ with a height of $0.3\,\mathrm{mm}$ and the respective cross-sectional area ($5\,\mathrm{mm} \times 5\,\mathrm{mm}$ and $4.4\,\mathrm{mm} \times 4.4\,\mathrm{mm}$). The ohmic and capacitive values of the reference electrode are estimated values that are in realistic dimensions. The in-plane conductivity of LSF is so high, that no according resistance was included in the electric circuit model.

Two scenarios were simulated. The first simulation reflects the short circuit effect of a cell with symmetric RE properties. However, it is very likely that the reference electrode is geometrically not symmetric since it is simply brushed on the side of

the sample. Furthermore, when bias is applied to the sample, the reference electrode resistances and capacitances are no longer symmetrical due to the potential spread across the RE. In other words, one part features different physical properties than the other which makes the ohmic and capacitive elements asymmetrical. This asymmetrical case is the second simulated scenario.

Table 4.6 shows the element parameters that were used in the two simulated scenarios.

Table 4.6: Simulation Parameters of the LTSPICE short circuit models

Element	Symmetrical	Asymmetrical
$R_{RE\,1}$	$50\,\Omega$	$50\,\Omega$
$R_{RE\,2}$	$50\,\Omega$	$40\,\Omega$
$C_{RE\,1}$	$10\,\mu F$	$10\,\mu F$
$C_{RE\,1}$	$10\,\mu F$	$6\,\mu F$
$R_{elyte\,1}$	$16\,\Omega$	
$R_{elyte\,2}$	$18\,\Omega$	
$R_{elyte\,3}$	$16\,\Omega$	
R_{WE}	$20\,\Omega$	
C_{WE}	$0.5\,mF$	
R_{CE}	$20\,\Omega$	
C_{CE}	$0.5\,mF$	

Figure 4.18 shows the impedance spectra for the symmetric and asymmetric RE configuration. Unlike the spectrum calculated from the finite elements analysis, the spectra arising from the equivalent network show an additional semicircle preceding the electrode semicircle due to the different time constants of WE and RE. The electrode semicircles in both cases return quite precisely the set values (error below 1 %). The high frequency semicircle is an artifact and caused by the short circuit effect. This can be explained according to Figure 4.19:
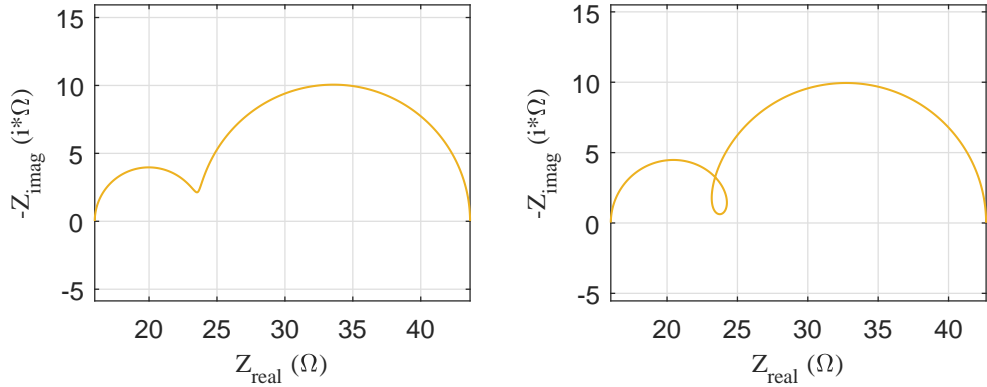
(a) Symmetric RE ($R_{RE\,1} = R_{RE\,2} = 50\,\Omega$; $C_{RE\,1} = C_{RE\,2} = 10\,\mu F$)

(b) Asymmetric RE ($R_{RE\,1} = 50\,\Omega$, $R_{RE\,2} = 40\,\Omega$, $C_{RE\,1} = 10\,\mu F$, $C_{RE\,2} = 6\,\mu F$)

Figure 4.18: Simulated 3-terminal impedance spectra of the LTSPICE short circuit model in Figure 4.17
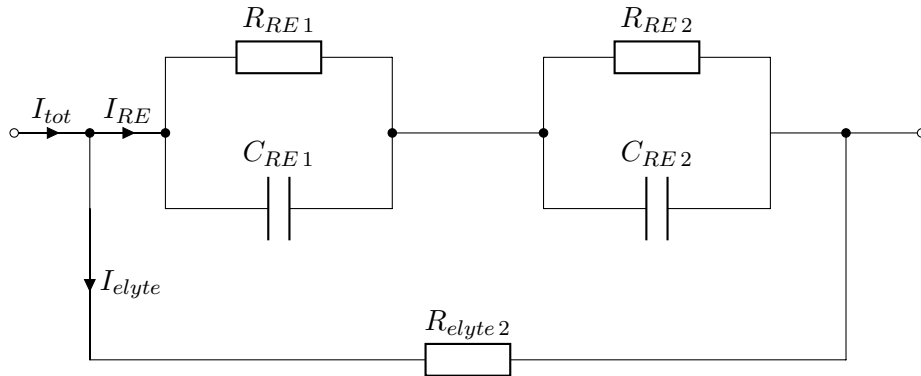
Figure 4.19: Current divider of the short circuit effect

The electric current faces a parallel circuit of the middle part of the electrolyte – corresponding to $R_{elyte\,2}$, and a current path via the reference electrode – a serial circuit of the two RC-elements arising from the reference electrode. For two identical RE RC-elements (symmetrical case), this equivalent circuit can be simplified to a simple RC-element with the values $R_{calculated} \approx 15.25\,\Omega$ and $C_{calculated} = 5\,\mu F$. The reference potential is tapped exactly at the center of this circuit and there-

fore, the apparent values equate precisely half of the calculated values. This is an important clue for identifying the high frequency semicircle as an artifact, because its diameter is approximately $\frac{R_{elyte\,2}}{2}$. This is because $R_{elyte\,2} \ll R_{RE\,1} + R_{RE\,2}$ and the total resistance of a parallel circuit is mostly determined by the smaller resistance. Of course a deviation will occur in reality because the system is not a 1D circuit as suggested in Figure 4.17, but a 3D geometry and the current distribution depends on the frequency.

The fit of the high frequency semicircle for the symmetrical scenario leads exactly to the expected apparent values $R_{apparent} = 7.63\,\Omega$ and $C_{apparent} = 10\,\mu F$. These are exactly the expected values ($\frac{R_{calculated}}{2}$ and $C_{calculated} \cdot 2$). Thus, the short circuit effect causes a separate artifact semicircle due to the lower RE capacitances. Electrode semicircle and short circuit semicircle are no longer superposed by each other. This case is not that critical because the short circuit semicircle appears well isolated from the electrode semicircle and hardly influences the extracted electrode properties.

In case the RE features asymmetric properties, a loop may appear in the transition zone between the semicircles. Figure 4.18b shows the spectrum for the scenario with asymmetric properties that contains a loop of this kind. The asymmetric RE properties can be caused by an applied bias, a geometrical asymmetry or a spatial material variation. It is noteworthy, that also in this case, the extracted WE properties are within 1 % error range.

The theory stated above can be confirmed by real measurements. Figure 4.20a shows a spectrum that was taken at 600 °C. At this temperature, $R_{elyte\,2} = 33.5\,\Omega$ according to [43]. The high frequency semicircle in this figure can be fitted with an R-CPE element and the returned ohmic value is 16.52 Ω. This agrees very well to the value of $\frac{R_{elyte\,2}}{2} = 16.75\,\Omega$. The slight deviation can be attributed to measurement inaccuracies and the parallel RE resistance, that lowers the total impedance of the parallel circuit. Furthermore, the small semicircle scales to a very small extent with the oxygen partial pressure. This is also in accordance with the theory because the RE impedance is partial pressure dependent. However, since the RE resistance exceeds the electrolyte resistance, the overall resistance is only
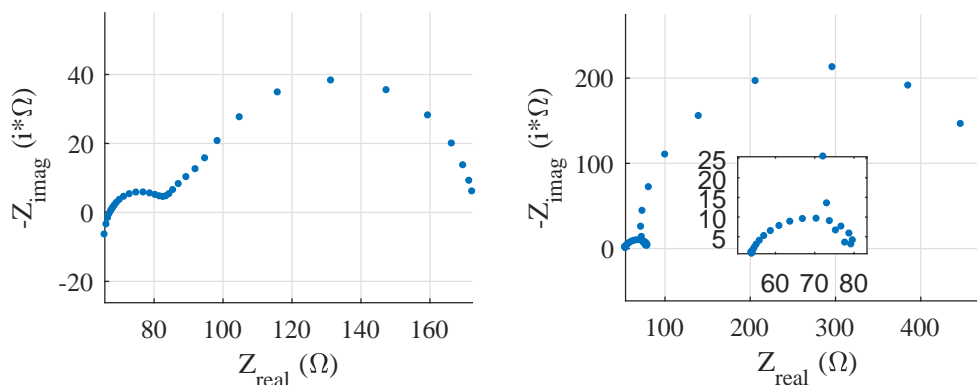
(a) RE semicircle without loop, $p_{O_2} = 50\,\%$, Bias: $250\,\text{mV}$ anodic

(b) RE semicircle with loop, without applied bias, $p_{O_2} = 0.1\,\%$

Figure 4.20: Measured ring geometry three-terminal impedance spectra with a reference electrode semicircle preceding the working electrode; the spectra were measured from different samples

influenced to a minor extent by the part of the RE. From these evaluations, it can be concluded that the semicircle in Figure 4.20a can be attributed to the voltage drop across the reference electrode.

Also the loops arising of an asymmetric RE were observed in real measurements. The earlier shown spectrum in Figure 4.4b was taken with an anodic bias of $450\,\text{mV}$. The same sample without applied bias did not show a loop which supports the theory of the asymmetric RE as loop origin.

Spectrum 4.20b was taken from a different sample without bias applied. This shows that the loop does not necessarily originate from applied bias.

To sum up, the conducted finite elements and electric circuit simulations have shown that there is an intrinsic *short circuit effect* through the reference electrode which causes errors in the apparent impedances and may also lead to additional artifact semicircles. The short circuit effect is a very critical error source because in the worst case, it can distort the measured electrode values without leaving a trace of distortion in the impedance spectrum. If the reference electrode causes an isolated semicircle, it is less critical, because this hardly affects the extracted WE properties.

4 Results and Discussion

The short circuit effect in the ring geometry occurs due to the reference electrode that is spatially extended in current flow direction. There are two geometrical options to tackle this problem.

- Not to spatially extend the RE in current flow direction

- Avoid a potential spread across the RE

These are obligatory specifications for the subsequent chapter that deals with alternative sample geometries.

4.3 Alternative Three-Terminal Sample Geometries

This chapter deals with alternative sample geometries that avoid the intrinsic error sources listed in Table 2.1 and the short circuit effect found in the previous chapter.

4.3.1 Microelectrode Geometry

The first attempt of an alternative geometry was the Microelectrode Geometry. A similar geometry was already listed in [12, configuration 4], however without specific results. Therefore, the geometry was built in COMSOL MULTIPHYSICS with the parameters outlined in Table 3.2. A sketch of the geometry can be found in section 3.1.3. The model was simulated 2D-axisymmetrically, leading to a cylindrical sample. In order to stay comparable with a rectangular sample, an equivalent sample radius of 5.64 mm was used. Thus, the sample surface deriving from the original size (10 mm × 10 mm) was kept constant.

In the model, the diameter of the microelectrode was parameterized with 200 μm. Two basic cases were simulated, one with a distance d from WE to RE of 10 μm and one with $d = 100$ μm. Table 4.7 shows the simulation results for the mentioned scenarios.

The apparent polarization resistances and chemical capacitances are erroneous, even though the distorted parts of the spectra were excluded from the fit. These errors become smaller with a decreasing distance d from WE to RE. An important insight is that the measured capacitance is more sensitive towards measurement errors. Additionally, the apparent WE resistances tend to be higher than the set resistances, whereas the apparent WE capacitances are smaller than the particular set values.

The impedance spectra of WE and CE for the case of $d = 100$ μm are shown in Figure 4.21. The WE spectrum shows a slope-like feature in the high frequency zone, whereas the CE spectrum shows an inductive arc in the same frequency range. The impedance features for the scenario $d = 10$ μm are qualitatively the same, however

Table 4.7: Microelectrode Geometry: Simulation results of a sample featuring symmetric WE-CE properties, Basic properties: $R_{pol} = 5\,\Omega\,\text{cm}^2$, $C_{chem} = 2\,\frac{\text{mF}}{\text{cm}^2}$

No.	WE to RE	Element	Set Values	Sim. Result	Error	Spectrum
1	$d = 10\,\mu\text{m}$	$R_{WE}\,(\Omega)$	5.002	5.197	3.90%	HF: slope (!)
		$C_{WE}\,(\text{mF})$	1.999	1.868	-6.58%	
		$R_{elyte\,WE}\,(\Omega)$		0.964		
		$R_{CE}\,(\Omega)$	5	4.833	-3.34%	
		$C_{CE}\,(\text{mF})$	2	2.118	5.91%	HF: inductive arc (!)
		$R_{elyte\,CE}\,(\Omega)$		6.179		
2	$d = 100\,\mu\text{m}$	$R_{WE}\,(\Omega)$	5.006	5.339	6.65%	HF: slope
		$C_{WE}\,(\text{mF})$	1.997	1.811	-9.33%	
		$R_{elyte\,WE}\,(\Omega)$		1.933		
		$R_{CE}\,(\Omega)$	5	4.715	-5.70%	
		$C_{CE}\,(\text{mF})$	2	2.193	9.62%	HF: inductive arc
		$R_{elyte\,CE}\,(\Omega)$		5.235		

even more pronounced. It is noteworthy that the extent of these distortion features does not correlate with the error of the extracted WE properties.

The reason for the errors in the results is the frequency dependent current distribution that reacts upon the potential distribution. The equipotential line of the RE for high frequencies is located higher than the one for low frequencies. This means that for high frequencies, the RE faces a thicker electrolyte relative to the WE, than for low frequencies. This explains the HF feature in Figure 4.21a. This shift is produced by the transition from primary to secondary current distribution due to the ohmic-capacitive properties of the electrodes. From the perspective of the CE, the electrolyte shift goes in the opposite direction, which is in accordance with the HF inductive arc in Figure 4.21b. This shift has the consequence that effectively, the investigated sample is a different one for high frequencies than for low frequencies. This shift was already described in section 2.1.4. In literature, the effect can be found in [15] and was referred to as "Variation of the Electrolyte Resistance".

Figure 4.22 shows the reference potential for high and for low frequencies for

(a) WE impedance spectrum

(b) CE impedance spectrum
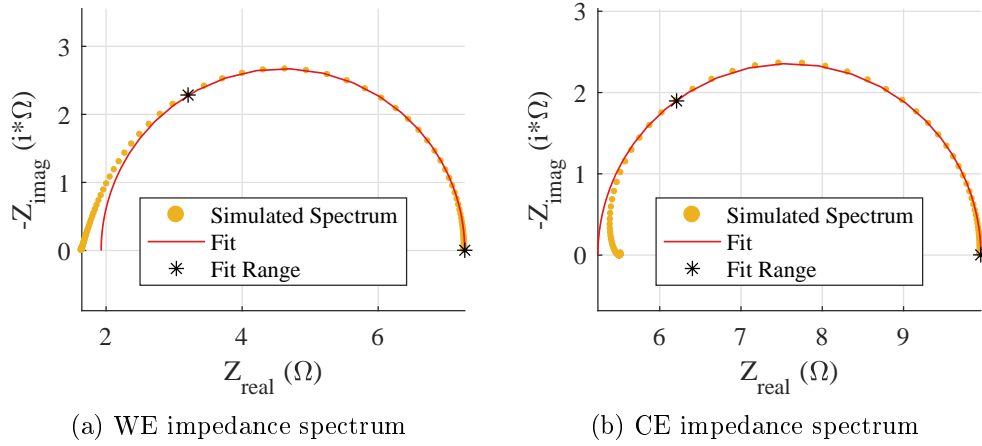
Figure 4.21: Microelectrode Geometry: Three-point impedance spectra resulting from the finite elements simulation, $d = 100\,\mu\text{m}$

$d = 100\,\mu\text{m}$. In this scenario, the shift is more pronounced than for $d = 10\,\mu\text{m}$, explaining the higher error of the apparent R_{pol} and C_{chem}. The reason for this is that the bigger electrode-uncovered space of the electrolyte leaves more possibilities for a more significant difference from primary to secondary current distribution.
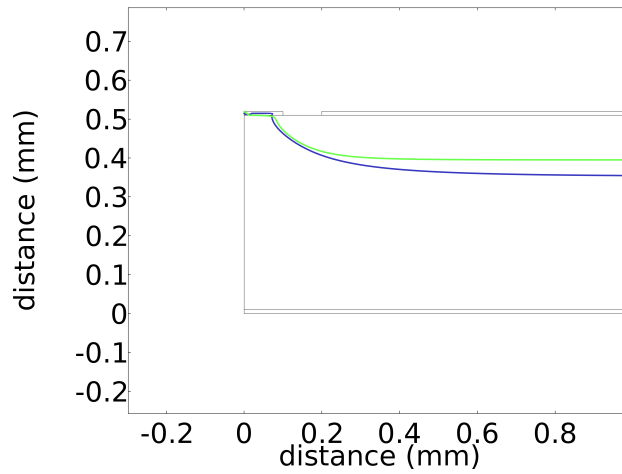
Figure 4.22: Microelectrode Geometry; distance from WE to RE $d = 100\,\mu\text{m}$; Green line: RE potential for $\omega \to \infty$, Dark blue line: $\omega \to 0$

To conclude, the microelectrode geometry leads to measurement errors due to the shift of the reference potential across the frequency range. The resulting errors are rather small (below 10 %) for symmetric WE/CE properties. However, in case WE and CE feature different physical properties, measurement errors increase as already stated in [16] and confirmed in sections 4.3.2 and 4.4.1. Even if one wants to measure solely symmetrical sample cells, there are better options. Moreover, the microelectrode geometry is hard to produce with thin film electrodes. A circular shadow mask would be required to produce a sample by

PLD. The fixation of the mask during the PLD process would also be hard to put into practice. Moreover, the contacting of the microelectrode itself is less practical than working with sheet samples. For all those reasons, the microelectrode geometry cannot be seen as an adequate solution for the intrinsic error sources and can therefore be ruled out as viable measuring geometry.

4.3.2 Rectangle Geometry

The Rectangle Geometry is an attempt to avoid a microelectrode. The aim was to get a better quantitative understanding of the errors resulting from this sample geometry. Similar geometries have already been investigated in [11–15, 17, 19]. The general outcome of those papers was that cells have to be symmetric in geometry and electrode properties to acquire meaningful results. Qualitatively, the reason of errors caused by non-symmetrical conditions is the RE equipotential line shift over frequency. This geometry was investigated in this thesis to get information on quantitative errors for specific sample properties and thus to test the tolerance with respect to any unavoidable asymmetry.

The chosen geometry was a quadratic YSZ sample with a height of 0.5 mm and a surface of $1\,cm^2$. The lengths of WE and RE were constant 5 mm and 1 mm. The length of the CE was varied.

The first simulation was conducted with perfectly aligned WE and CE (misalignment $m = 0\,mm$). In this scenario, the impedance spectra do not feature any perturbation and the potential distribution stays quite symmetric over the entire

frequency range. The results are listed in Table 4.8. The resulting resistances and

Table 4.8: Rectangle geometry: Simulation results of a sample featuring perfectly aligned WE and CE ($m = 0\,\text{mm}$), Basic properties: $R_{pol} = 5\,\Omega\,\text{cm}^2$, $C_{chem} = 2\,\frac{\text{mF}}{\text{cm}^2}$

No.	m	Element	Set Values	Sim. Result	Error
1	$0\,\text{mm}$	$R_{WE}\,(\Omega)$	10	10.050	0.50%
		$C_{WE}\,(\text{mF})$	1	0.988	-1.24%
		$R_{CE}\,(\Omega)$	10	10.050	0.50%
		$C_{CE}\,(\text{mF})$	1	0.988	-1.22%

capacitances are afflicted with an error in the scale of $1\,\%$. The errors are caused by the asymmetrically placed RE. If the RE potential was tapped at center height at the side of the sample, the error would not arise. Two trends that already existed in the microelectrode geometry also occur in the rectangle geometry.

- The apparent electrode resistance is higher than the set value, whereas the apparent capacitance is lower than the particular set value

- The capacitance error exceeds the error of the resistance

The errors resulting from the perfectly symmetric case are still in a tolerable range. However, in case the perfect alignment is not met, the notorious difficulties caused by asymmetries arise. In order to investigate the sensitivity towards misalignment of WE and CE, the length of the CE was varied, whereas the length of the WE was kept constant. Both electrodes featured identical properties. Figure 4.23 shows the error of the apparent WE polarization resistance in dependence of the WE-CE misalignment m. The plot shows that the error scales - to a very good approximation - linearly with the electrode misalignment. Furthermore, it can be seen that the sensitivity towards imperfect electrode alignment is very critical. The fitted linear function features a slope of about $75\,\%$ per mm misalignment.

As a consequence of the asymmetric RE placement, the misalignment to achieve an error-free polarization resistance, is not at $m = 0$, but at $m \approx 0.02\,\text{mm}$. It is
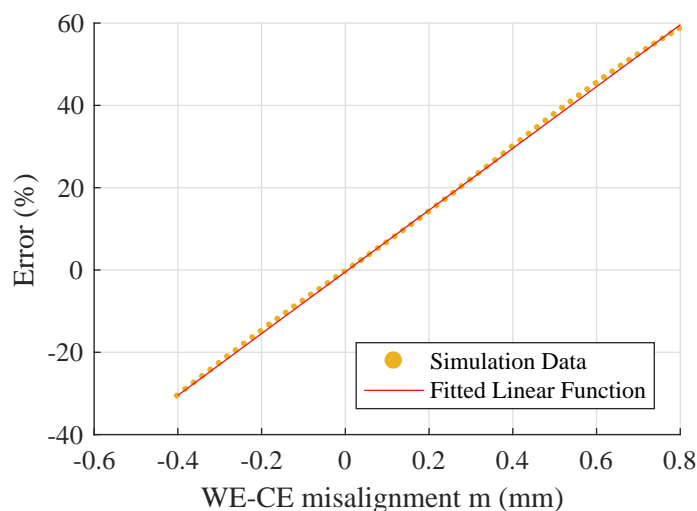
Figure 4.23: Rectangle geometry: Error of apparent WE polarization resistance in dependence of WE-CE misalignment for symmetrical electrode properties; sample height 0.5 mm; Fitted function: $y = 75.0287 * x - 0.4545$

noteworthy that the optimum for the apparent capacitance does not equal the optimum for the apparent resistance. Furthermore, the error of the capacitance goes in the opposite direction as the error of the resistance, as previously shown. This sensitivity is dependent on several factors. One of these factors is the electrolyte thickness (sample height). Therefore, three scenarios with different sample heights (0.5 mm, 1 mm and 2 mm were simulated and the resulting polarization resistance error was plotted in Figure 4.24. This figure shows that the sensitivity decreases with a higher electrolyte thickness. This is already a hint that the error source in this case is again the shift of the reference potential over the frequency range. For thicker electrolytes, the relative shift of the RE equipotential line in ratio with the total sample height is smaller and therefore leads to a smaller error.

A sample height of 2 mm exhibits an error slope of only 16.1 % per mm misalignment. However, a misalignment of about 0.29 mm is required to achieve the optimal polarization resistance measurement. With this misalignment, the error in the apparent capacitance is already quite big. A reasonably small misalignment results for a sample height of 1 mm. Here, the polarization resistance error becomes 0 if
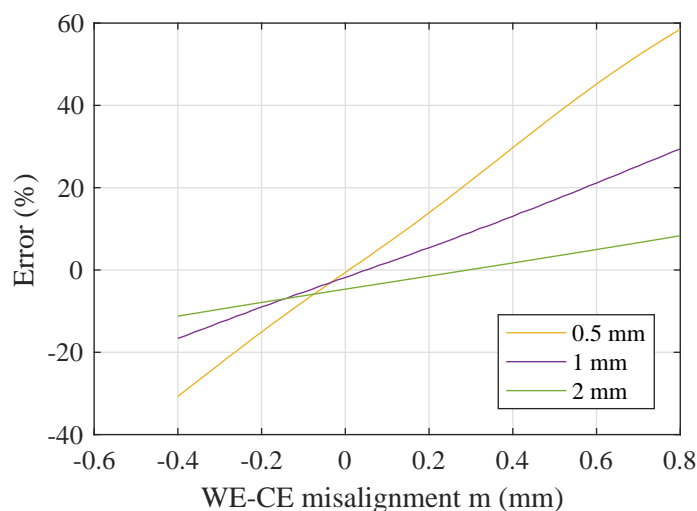
Figure 4.24: Rectangle geometry: Error of apparent WE polarization resistance in dependence of WE-CE misalignment for symmetrical electrode properties; different sample heights (see legend)

$m \approx 0.045 \, \text{mm}$. The error slope in this case is about $38\,\%$ per mm misalignment.

In order to show that the reason for the distorted apparent physical properties is indeed the RE equipotential line shift, the reference potential in the low and high frequency case is plotted in Figure 4.25. The plot refers to the scenario of $m = -0.4\,\text{mm}$, meaning that the CE is longer than the WE. As already expected, there is a RE equipotential line shift over frequency leading to distortions in the apparent resistance and capacitance. In this case, the low frequency equipotential line of the RE even ends at the edge of the CE. This has the consequence that the resulting apparent WE impedance contains a part of the CE impedance. When considering the CE, this part of the impedance misses and the CE resistance therefore appears to be even smaller than its set value. Thus, for low frequencies, the RE is not even able to separate the WE overpotential from the voltage drop across the rest of the cell. This effect was entitled "cross-contamination" in [15]. This effect adds up to the reference potential shift in this electrode alignment.

Considering the sensitivity towards electrode misalignment, the rectangle geome-
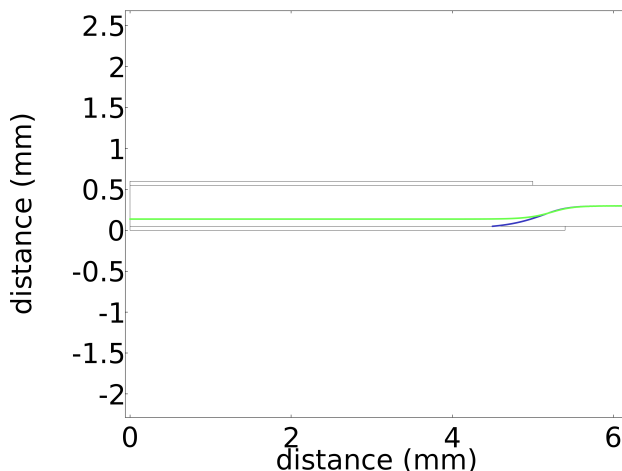
Figure 4.25: Rectangle Geometry; WE-CE misalignment $m = -0.4\,\mathrm{mm}$; Green line: RE potential for $\omega \to \infty$, Dark blue line: $\omega \to 0$

try is highly disadvantageous. Even the optimum for the least error in apparent polarization resistance depends on the electrolyte thickness. For electrodes that feature even lower resistances than LSF, higher errors and misalignment sensitivities can be expected. This is a consequence of the current cross section within the electrolyte further expanding, as the electrode resistance becomes very small. Thus, reliable results are difficult to obtain with this geometry and it can therefore be ruled out as a satisfying alternative sample geometry.

An interesting insight is that the error of the WE resistance scales linearly with the electrode misalignment. A similar plot was already shown in [13, Fig. 4] which suggests that this linearity can only be found within a certain misalignment range. The results could have been reproduced in this work. However, since the error potential is already quite high, only as a consequence of misaligned electrodes, the errors from asymmetric WE and CE properties are not investigated in this work. The results of this section clearly demonstrate that it would be best to place the RE somewhere in between WE and CE to achieve a higher level of symmetry.

4.4 Optimized Setup: Single Wing Geometry

The single wing geometry aims to avoid a frequency dependent current distribution causing the RE equipotential line to shift over frequency as for the microelectrode and rectangle geometry. This is achieved by a high level of symmetry and the RE placed centrally in between WE and CE. The improvement compared to the ring geometry is that the RE is located far away from the current flow within the electrolyte, thus avoiding the short circuit effect through the RE.

The model geometry was built accordingly to section 3.1.5. Figure 4.26 shows

(a) 3D view   (b) Side view
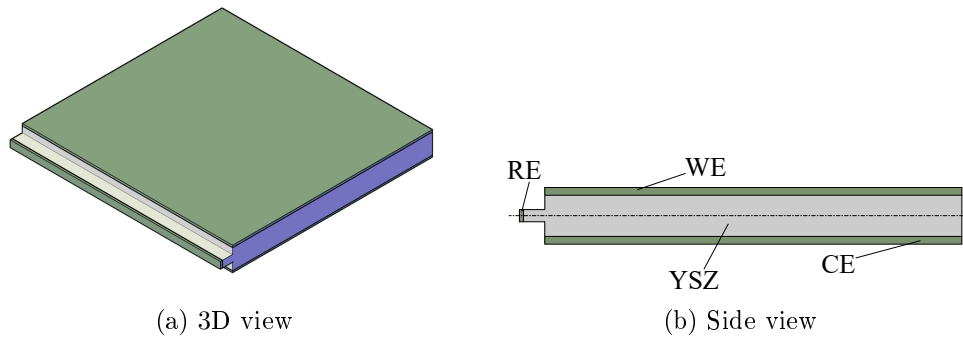
Figure 4.26: Single wing geometry sample

again the 3D and the side view of the sample cell. The RE height was 0.3 mm and the protrusion depth was 0.5 mm. The reference potential was tapped at the outer edge of the RE at center height. The physical properties were set according to Table 3.2. A related electrolyte geometry was already tested numerically in [19], however with the reference electrode on top of the protrusion. In this work, the RE is placed on the side to ensure a higher symmetry and easier contacting.

(a) Primary current distribution ($\omega \to \infty$)   (b) Secondary current distribution ($\omega \to 0$)
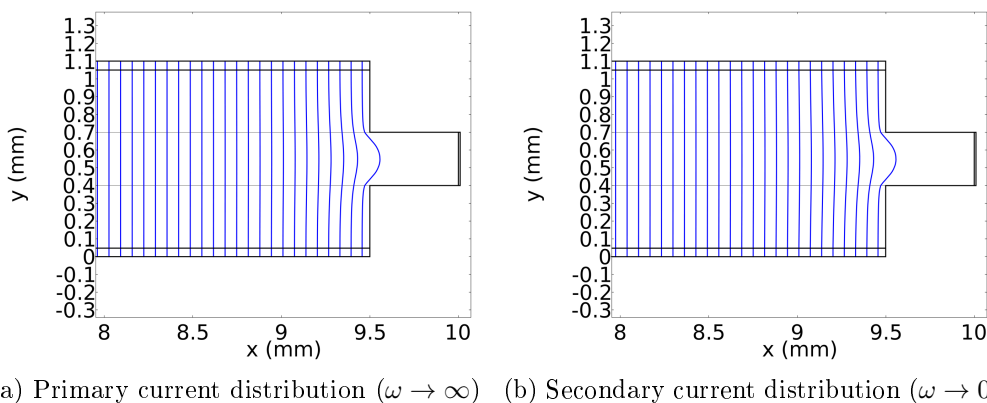
Figure 4.27: Single wing geometry: Current distribution within and around the RE; the material's properties are listed in Table 3.2

The first step was to check the current and potential distribution within the sample. Figure 4.27 shows the primary and secondary current distribution within and around the RE. The density of the blue current lines reflects the current density (magnitude controlled). From the plot, it can be concluded that the field distortion around the protrusion is marginal and a short circuit effect through the RE is avoided. Moreover, the current distribution is almost frequency independent.

To qualitatively underpin this statement, Figure 4.28 shows the magnitude of the primary and secondary current density at the center of the sample. Note that the x-axis origin is at $8\,\mathrm{mm}$. The illustrated zone only shows the $2\,\mathrm{mm}$ around the protrusion since the current density is constant beyond this zone. From Figure 4.28a can be seen that the current density within the RE is about $\frac{1}{14} \approx 7\%$ of the current density within the electrolyte. This means that the short circuit effect is not completely avoided, but greatly reduced. Since the RE thickness is very small compared to the width of the sample, the current through the RE is far smaller than the overall current through the electrolyte.

Figure 4.28b illustrates that there is almost no current through the RE in the low frequency case. This is due to the relatively high resistive barrier of the oxygen exchange reaction on the RE/YSZ interface.

Up to here, it was shown that the current distribution in the single wing geome-

(a) Primary current density ($\omega \to \infty$)   (b) Secondary current density ($\omega \to 0$)
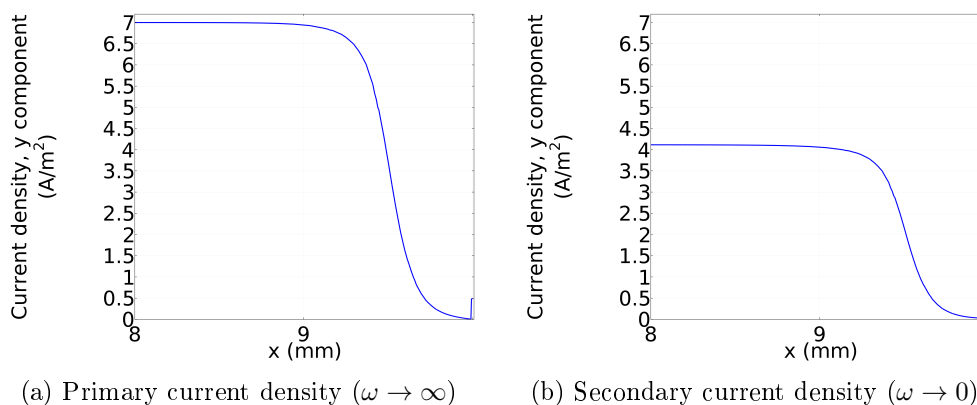
Figure 4.28: Single wing geometry: Current density $\left(\frac{A}{m^2}\right)$ for the outer $2\,\text{mm}$ of the sample at center height

try is favourable. A further advantage of this geometry is its reference electrode location in the center between WE and CE and not at the same surface as one of the current carrying electrodes. Therefore, the reference potential does not change over frequency which reduces the possible error introduced by a RE potential shift as described in section 2.1.4. Figure 4.29 underpins this advantage by showing that the reference potential is constantly $5\,\text{mV}$ over the whole frequency range. Furthermore, there is almost no potential spread from top to bottom of the RE.

However, the very small amount of current flow through the RE might lead to slight errors or artifacts. To ensure that the extent of the errors is negligible, the three-terminal impedance spectrum was calculated and is shown in Figure 4.30. The spectrum shows an electrode semicircle without any noticeable perturbation. The surface of $0.95\,\text{cm}^2$ leads to set values of $R_{set} = 5.263\,\Omega$ and $C_{set} = 1.9\,\text{mF}$ for each electrode. A fit of the curve returns *exactly* those values. This shows that the single wing geometry is perfect for measuring a sample with symmetric WE and CE properties because it does neither lead to measurement errors, nor to artifacts in the impedance spectrum.
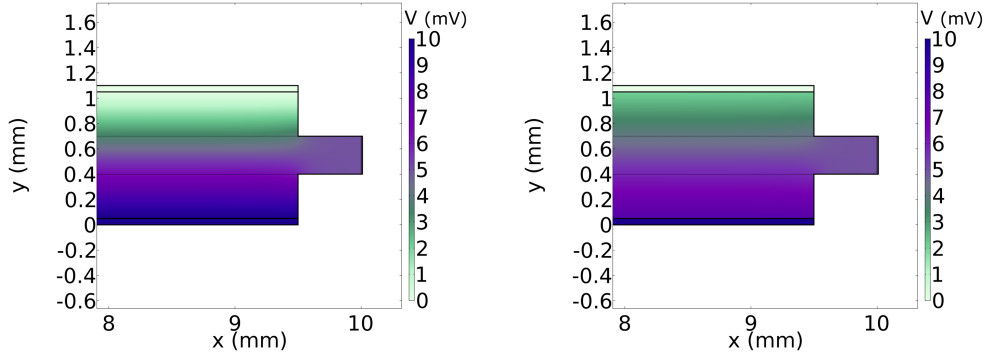
(a) Primary potential distribution ($\omega \to \infty$) (b) Secondary potential distribution ($\omega \to 0$)

Figure 4.29: Single wing geometry: Potential distribution (mV) within and around the RE
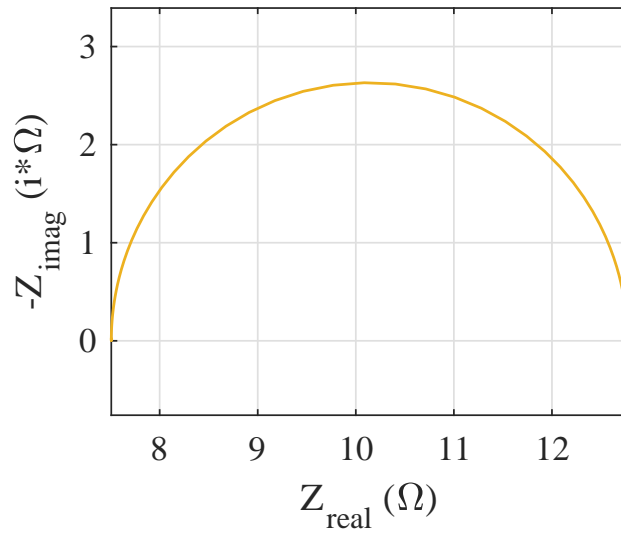
Figure 4.30: Simulated three-terminal spectrum of a single wing geometry sample with identical WE and CE properties; The diameter R_{sim} of the semicircle equals exactly the set value R_{set} of $5.263\,\Omega$; the extracted capacitance of $1.9\,\text{mF}$ is also in accordance with its set parameter

4.4.1 Asymmetric WE and CE propertes

According to [16], asymmetrical WE and CE properties can lead to distortions in the impedance spectrum as a consequence of a non-ideal reference potential progression over frequency, even with perfectly aligned WE and CE. When measuring electrode properties with superposed DC voltage, the electrodes will mostly have different resistances and capacitances. Therefore, also several scenarios with asymmetric electrode properties were investigated for the single wing geometry.

The basic method was to parameterize the CE with standard LSF properties outlined in Table 3.2 ($5\,\Omega\,\mathrm{cm}^2$ and $2\,\frac{\mathrm{mF}}{\mathrm{cm}^2}$). The WE resistance and capacitance were varied by $\pm$ one order of magnitude to introduce an asymmetry.

The sample geometry was the same throughout all the simulations (see section 3.1.5). The single wing geometry is made out of a $10\,\mathrm{mm} \times 10\,\mathrm{mm} \times 1\,\mathrm{mm}$ YSZ single crystal. On one side, there are cuts at the top and the bottom of the sample with a depth of $0.5\,\mathrm{mm}$ and a height of $0.35\,\mathrm{mm}$, resulting in a protrusion of $0.3\,\mathrm{mm}$ height that hosts the reference electrode. Table 4.9 shows the fit results that were derived from the generated impedance spectra. Note that the error is defined as $\frac{X_{result}-X_{set}}{X_{set}}$, where X . . . measured quantity.

Table 4.9 shows, that the single wing geometry leads to minor errors that are mostly below $2\,\%$. This is an error range far smaller than the other examined geometries. However, two scenarios showed significant artifacts or measurement errors: Those are highlighted with a bold font in the table.

The WE impedance spectrum of scenario 6 - featuring a low WE resistance and capacitance - yielded an inductive semicircle at the low frequency range at around $100\,\mathrm{Hz}$ to $10\,\mathrm{mHz}$. The spectrum is shown in Figure 4.31. The reason for this is the difference in primary and secondary potential distribution within the sample depicted in Figure 4.32. For high frequencies, the potential distribution is symmetric and the RE equipotential line is at the center of the electrolyte. For low frequencies, the potential distribution is asymmetric. This causes a shift of the RE equipotential line, resulting in a lower apparent electrolyte resistance at low frequencies, see also section 4.3.1, 4.3.2 and [15].

The frequency range of this artifact was well separated from the WE semicircle

Table 4.9: Single wing geometry: Simulation results of a sample exhibiting asymmetric WE-CE properties, Basic properties: $R_{pol} = 5\,\Omega\,\mathrm{cm}^2$, $C_{chem} = 2\,\frac{\mathrm{mF}}{\mathrm{cm}^2}$

No.	WE Modification	Element	Set Value	Sim. Result	Error	Spectrum Anomaly
1	Symmetric Cell	$R_{WE}\,(\Omega)$	5.263	5.263	0.00%	-
		$C_{WE}\,(\mathrm{mF})$	1.900	1.900	0.00%	
		$R_{CE}\,(\Omega)$	5.263	5.263	0.00%	
		$C_{CE}\,(\mathrm{mF})$	1.900	1.900	0.00%	-
2	$R_{pol}/10$	$R_{WE}\,(\Omega)$	0.526	0.520	-1.14%	slight LF distortion
		$C_{WE}\,(\mathrm{mF})$	1.900	1.890	-0.54%	
		$R_{CE}\,(\Omega)$	5.263	5.294	0.59%	
		$C_{CE}\,(\mathrm{mF})$	1.900	1.885	-0.78%	-
3	$R_{pol} * 10$	$R_{WE}\,(\Omega)$	52.632	52.680	0.09%	-
		$C_{WE}\,(\mathrm{mF})$	1.900	1.895	-0.27%	
		$R_{CE}\,(\Omega)$	5.263	5.211	-0.99%	very slight LF distortion
		$C_{CE}\,(\mathrm{mF})$	1.900	1.899	-0.07%	
4	$C_{chem}/10$	$R_{WE}\,(\Omega)$	5.263	5.268	0.09%	non-ideal semicircle
		$C_{WE}\,(\mathrm{mF})$	0.190	0.188	-1.06%	
		$R_{CE}\,(\Omega)$	5.263	5.274	0.21%	non-ideal semicircle
		$C_{CE}\,(\mathrm{mF})$	1.900	1.905	0.24%	
5	$C_{chem} * 10$	$R_{WE}\,(\Omega)$	5.263	5.276	0.24%	non-ideal semicircle
		$C_{WE}\,(\mathrm{mF})$	19.000	19.046	0.24%	
		$R_{CE}\,(\Omega)$	5.263	5.270	0.13%	non-ideal semicircle
		$C_{CE}\,(\mathrm{mF})$	1.900	1.880	-1.06%	
6	$R_{pol}/10$, $C_{chem}/10$	$R_{WE}\,(\Omega)$	0.526	0.531	0.83%	**LF inductive semicircle**
		$C_{WE}\,(\mathrm{mF})$	0.190	0.187	-1.35%	
		$R_{CE}\,(\Omega)$	5.263	5.296	0.62%	
		$C_{CE}\,(\mathrm{mF})$	1.900	1.883	-0.87%	-
7	$R_{pol} * 10$, $C_{chem}/10$	$R_{WE}\,(\Omega)$	52.632	52.670	0.07%	-
		$C_{WE}\,(\mathrm{mF})$	0.190	0.189	-0.36%	
		$R_{CE}\,(\Omega)$	5.263	5.229	-0.65%	non-ideal semicircle
		$C_{CE}\,(\mathrm{mF})$	1.900	1.941	2.16%	
8	$R_{pol}/10$, $C_{chem} * 10$	$R_{WE}\,(\Omega)$	0.526	0.497	**-5.57%**	non-ideal semicircle
		$C_{WE}\,(\mathrm{mF})$	19.000	20.770	**9.32%**	
		$R_{CE}\,(\Omega)$	5.263	5.293	0.57%	
		$C_{CE}\,(\mathrm{mF})$	1.900	1.883	-0.88%	-
9	$R_{pol} * 10$, $C_{chem} * 10$	$R_{WE}\,(\Omega)$	52.632	52.680	0.09%	-
		$C_{WE}\,(\mathrm{mF})$	19.000	18.929	-0.37%	
		$R_{CE}\,(\Omega)$	5.263	5.283	0.38%	slight LF distortion
		$C_{CE}\,(\mathrm{mF})$	1.900	1.880	-1.04%	

(a) Total impedance spectrum

(b) Low frequency part of the impedance spectrum
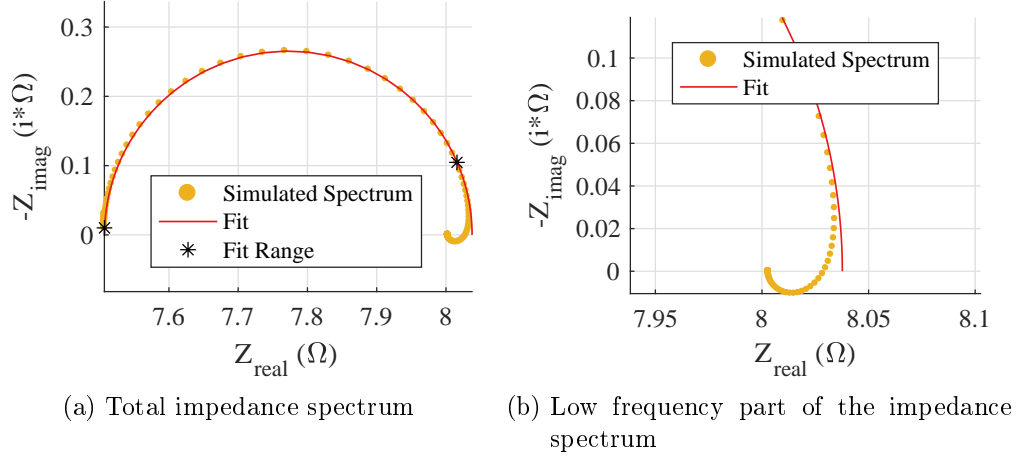
Figure 4.31: Scenario 6: Simulated WE impedance spectrum of a single wing geometry sample with $R_{WE} = 0.5\,\Omega\,\text{cm}^2$, $R_{CE} = 5\,\Omega\,\text{cm}^2$, $C_{WE} = 0.2\,\frac{\text{mF}}{\text{cm}^2}$, $C_{CE} = 2\,\frac{\text{mF}}{\text{cm}^2}$

(a) Primary potential distribution ($\omega \rightarrow \infty$)

(b) Secondary potential distribution ($\omega \rightarrow 0$)
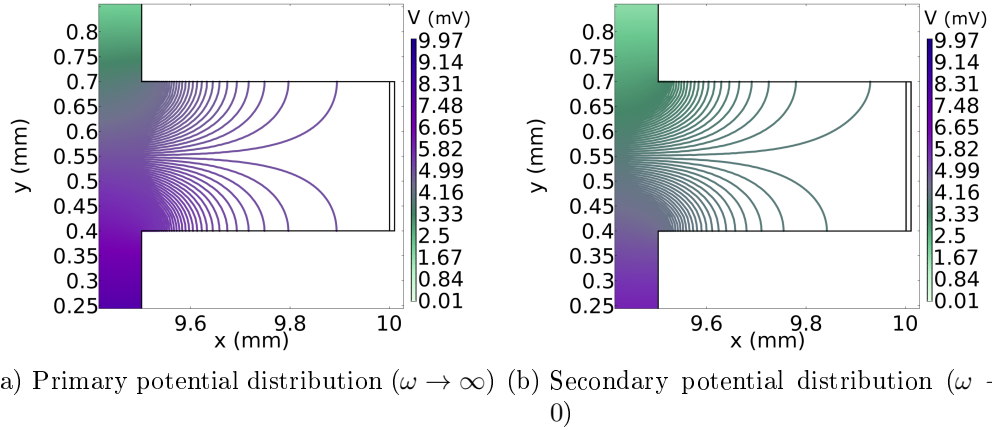
Figure 4.32: Single wing geometry Scenario 6: Potential distribution (mV) around and within the RE

because the peak frequencies of WE and CE diverged from one another by a factor of 100. Thus, the inductive artifact semicircle could be separated from the WE semicircle without significantly distorting the latter. Although this new geometry cannot completely avoid artifacts, they do not interfere with the feature of interest if their peak frequencies are sufficiently different.

This effect is much more critical, if WE and CE have asymmetric resistances but identical relaxation times, ergo identical peak frequencies. Thus, the transition of the electrolyte resistance occurs in the same frequency range as the WE semicircle and the derived electrode properties are erroneous, despite an almost ideal looking impedance spectrum. The only discrepancy is a slight deviation of fit and simulated spectrum in Figure 4.33 starting at the same frequency as the inductive semicircle from the previous example (around $100\,\text{Hz}$).
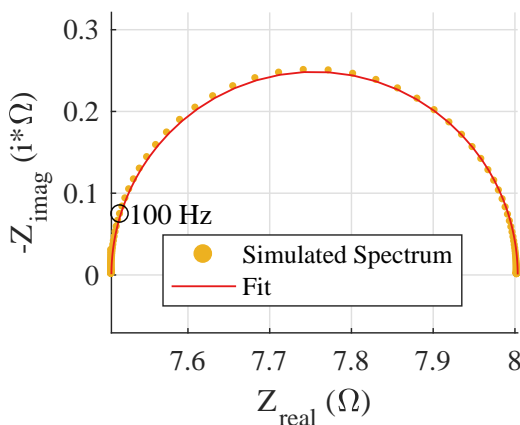
Figure 4.33: Scenario 8: Simulated WE impedance spectrum of a single wing geometry sample with $R_{WE} = 0.5\,\Omega\,\text{cm}^2$, $R_{CE} = 5\,\Omega\,\text{cm}^2$, $C_{WE} = 20\,\frac{\text{mF}}{\text{cm}^2}$, $C_{CE} = 2\,\frac{\text{mF}}{\text{cm}^2}$; a slightly imperfect fit starts at about $100\,\text{Hz}$

The effect of asymmetric WE/CE properties on the impedance spectrum is summarized in Figure 4.34. This figure shows three impedance spectra with the very same set value for the WE polarization resistances $R_{WE\,set} = 0.5263\,\Omega$. One spectrum shows the undistorted impedance spectrum of a sample with an identical CE ($R_{pol} = 0.5263\,\Omega$, $C_{chem} = 1.9\,\text{mF}$). The other spectra show the WE impedance spectra of scenario 6 and scenario 8. Spectrum 6 shows the inductive loop with the

(a) Total impedance spectra

(b) Detailed view on the spectra difference
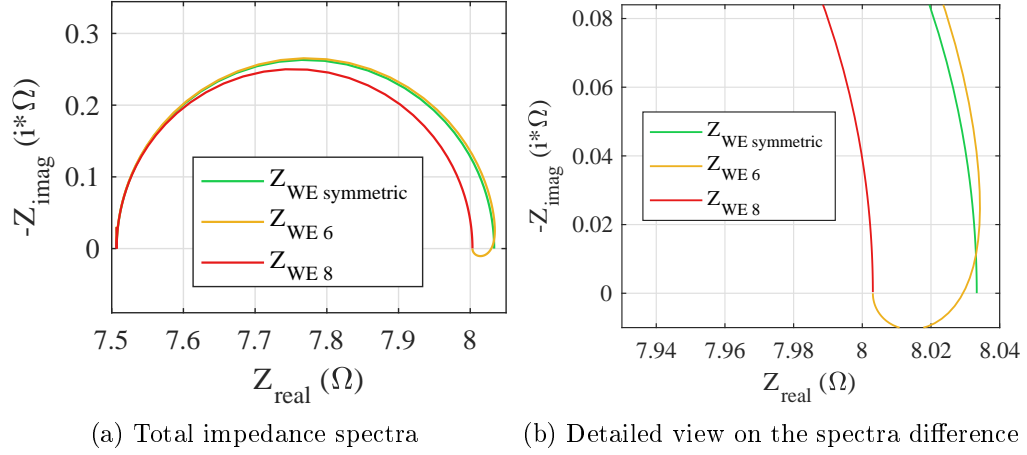
Figure 4.34: Simulated WE impedance spectra of the single wing geometry; every scenario features the same set value for the WE polarization resistance $R_{WE\,set} = 0.5263\,\Omega$. The green spectrum is undistorted and stems from a scenario with an identical CE. The yellow graph shows the WE spectrum of scenario 6, in which the RE equipotential line shift occurs quite well separated from the WE semicircle, due to the different peak frequencies of WE and CE ($f_{peak\,WE} = 100 \cdot f_{peak\,CE}$). The red spectrum represents scenario 8, the worst case scenario ($f_{peak\,WE} = f_{peak\,CE}$). Here, the RE equipotential line shift distorts the impedance spectrum at the characteristic frequency of the WE and thus leads to erroneous results without leaving a trace in the spectrum

big advantage that this distortion is quite well separated from the WE semicircle because the peak frequencies of WE and CE differ from one another by a factor of 100. Spectrum 8 shows the worst case scenario, where the RE equipotential line shift occurs at the characteristic frequency of the WE and thus distorts the extracted values without leaving a trace in the spectrum.

4.4.2 Influence of the Electrolyte

The evaluations above show that measurements with asymmetric WE/CE properties, low-ohmic electrodes and identical relaxation times of the electrodes are very likely to cause measurement errors. Moreover, the transition from primary to secondary current distribution also depends on the electrolyte resistance. If the ratio $a = \frac{R_{electrolyte}}{R_{measured\ electrode}}$ increases, the current will "use" the extended cross section even more at high frequencies, in order to compensate the higher resistance of the electrolyte. This leads to a more significant change of current distribution over frequency. When considering the CE in Table 4.9, Scenario 7, this consideration is confirmed. From the perspective of the CE, this is the same asymmetry as for the WE in Scenario 8, only that the ratio $a = \frac{R_{electrolyte}}{R_{electrode\ measured}}$ is smaller, thus causing the smaller error. The errors of the derived CE properties are much smaller and still in the tolerable region. To get a quantitative impression, the ratio a for the WE, scenario 8 was $\frac{R_{electrolyte}}{R_{measured\ electrode}} = \frac{15\Omega}{0.526\Omega} \approx 28.5$, resulting in critical errors of up to 10 %; whereas for the CE, scenario 7, $a = \frac{15\Omega}{5.263\Omega} \approx 2.85$, resulted in rather low errors of only about 2 %.

To underpin this statement, additional simulations with varying electrolyte resistance were conducted. In general, there are two parameters to influence the overall electrolyte resistance.

- Electrolyte conductivity respectively resistivity (σ_{elyte} respectively ρ_{elyte})

- Thickness of the electrolyte, while keeping the ratio of protrusion height to sample thickness constant ($\frac{h_{protrusion}}{h_{sample}} = 0.3$)

To quantitatively show the electrolyte influence, three more scenarios were thus considered with the electrode properties of the worst case Scenario 8 of Table 4.9 (low-ohmic electrodes and identical relaxation times). The results of the simulations are presented in Table 4.10.

Scenario 10 and 12 show significant errors of about 10 % without showing any notable distortion or artifact in the corresponding impedance spectrum. In these scenarios, the electrolyte resistance was increased. Thus, the difference between

Table 4.10: Single wing geometry: Variation of electrolyte parameters, asymmetric electrode properties like in Scenario 8; Set Values: $R_{WE} = 0.526\,\Omega$, $R_{CE} = 5.263\,\Omega$, $C_{WE} = 19\,\mathrm{mF}$, $C_{CE} = 1.9\,\mathrm{mF}$

No.	Variation	Element	Sim. Result	Error	Spectrum Anomaly
10	$\rho_{elyte} * 10$	$R_{WE}\,(\Omega)$	0.477	**-9.38%**	-
		$C_{WE}\,(\mathrm{mF})$	21.121	**11.16%**	
		$R_{CE}\,(\Omega)$	5.313	0.95%	
		$C_{CE}\,(\mathrm{mF})$	1.881	-1.02%	-
11	$\rho_{elyte}/10$	$R_{WE}\,(\Omega)$	0.522	-0.73%	non-ideal semicircle
		$C_{WE}\,(\mathrm{mF})$	19.441	2.32%	
		$R_{CE}\,(\Omega)$	5.267	0.07%	
		$C_{CE}\,(\mathrm{mF})$	1.893	-0.37%	-
12	$h_{sample} * 10$	$R_{WE}\,(\Omega)$	0.578	**9.75%**	-
		$C_{WE}\,(\mathrm{mF})$	17.027	**-10.38%**	
		$R_{CE}\,(\Omega)$	5.348	1.61%	
		$C_{CE}\,(\mathrm{mF})$	1.864	-1.89%	-

primary and secondary current distribution was bigger and the RE equipotential line varied to a larger extent. These simulation results underpin the statement that the ratio $a = \frac{R_{\mathrm{electrolyte}}}{R_{\mathrm{measured\ electrode}}}$ should not get too large. Scenario 11 featured an error in apparent polarization resistance of below than 1 % and a capacitance error of 2.32 %. These errors are in a tolerable region. The ratio $a = \frac{R_{\mathrm{electrolyte}}}{R_{\mathrm{measured\ electrode}}}$ was $\frac{1.5\Omega}{0.526\Omega} = 2.85$.

4.4.3 Influence of the Protrusion Height

Generally speaking, the difference between primary and secondary current distribution determines the extent of the measurement error. Thus, a safe strategy to avoid this error source, is to minimize the frequency dependence of the current distribution. Apart from lowering the electrolyte resistance, this can also be achieved by adjusting the sample shape. To investigate this, several scenarios featuring the electrode properties of Scenario 8 and different protrusion heights were simulated. The results are summarized in Table 4.11.

Table 4.11 shows that the error in measured electrode properties can be minimized

Table 4.11: Single wing geometry: Variation of protrusion height, sample height = 1 mm, asymmetric electrode properties like in Scenario 8; Set Values: $R_{WE} = 0.526\,\Omega$, $R_{CE} = 5.263\,\Omega$, $C_{WE} = 19\,\text{mF}$, $C_{CE} = 1.9\,\text{mF}$

No.	$h_{protrusion}$	Element	Sim. Result	Error	Spectrum Anomaly
13	0.1 mm	$R_{WE}\,(\Omega)$	0.523	-0.66%	-
		$C_{WE}\,(\text{mF})$	19.194	1.02%	
		$R_{CE}\,(\Omega)$	5.267	0.07%	
		$C_{CE}\,(\text{mF})$	1.898	-0.11%	-
14	0.2 mm	$R_{WE}\,(\Omega)$	0.513	-2.47%	-
		$C_{WE}\,(\text{mF})$	19.745	3.92%	
		$R_{CE}\,(\Omega)$	5.276	0.24%	
		$C_{CE}\,(\text{mF})$	1.893	-0.39%	-
15	0.3 mm $\hateq$ Scenario 8	$R_{WE}\,(\Omega)$	0.497	-5.57%	non-ideal semicircle
		$C_{WE}\,(\text{mF})$	20.770	9.32%	
		$R_{CE}\,(\Omega)$	5.293	0.57%	
		$C_{CE}\,(\text{mF})$	1.883	-0.88%	-
16	0.4 mm	$R_{WE}\,(\Omega)$	0.473	-10.10%	non-ideal semicircle
		$C_{WE}\,(\text{mF})$	22.473	18.28%	
		$R_{CE}\,(\Omega)$	5.317	1.02%	
		$C_{CE}\,(\text{mF})$	1.870	-1.60%	-
17	0.5 mm	$R_{WE}\,(\Omega)$	0.441	-16.20%	non-ideal semicircle
		$C_{WE}\,(\text{mF})$	25.250	32.89%	
		$R_{CE}\,(\Omega)$	5.350	1.65%	
		$C_{CE}\,(\text{mF})$	1.851	-2.61%	-

by keeping the protrusion height, i.e. the ratio $b = \frac{h_{\text{protrusion}}}{h_{\text{sample}}}$ small. With the chosen parameters, the resulting capacitance error is higher than the error of the polarization resistance. Moreover, the errors feature opposite tendencies. The apparent capacitance exceeds its set value, whereas the apparent resistance is lower than it was parameterized. Figure 4.35 shows the error of polarization resistance and chemical capacitance in dependence of the protrusion height.

To summarize, the single wing geometry is the best geometry that was evaluated in this thesis. The short circuit effect is almost completely avoided and the measurement error for symmetric cells is effectively 0. In case of asymmetric WE/CE
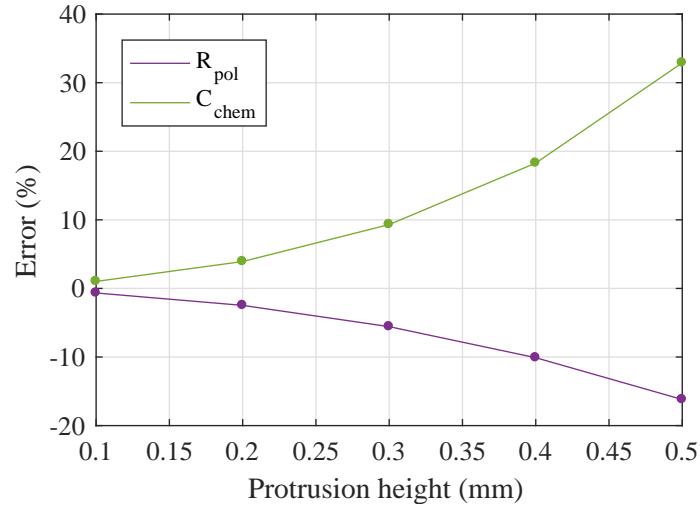
Figure 4.35: Single wing geometry: Error of simulated polarization resistance and chemical capacitance in dependence of protrusion height; asymmetric electrode properties according to Scenario 8

properties, a shift of the RE equipotential line is likely to occur. For a WE with a low resistance, a high capacitance and the same relaxation time as the counter electrode, this error source is most likely to cause measurement errors. Due to the identical characteristic frequencies of WE and CE, this effect is hidden in the electrode arc and is therefore impossible to identify as measurement error. This intrinsic error source can be minimized by a low ratio $a = \frac{R_{\text{electrolyte}}}{R_{\text{measured electrode}}}$ and a low ratio of $b = \frac{h_{\text{protrusion}}}{h_{\text{sample}}}$.

5 Conclusion and Outlook

In this thesis, possible error sources in three-point impedance spectroscopy measurements were investigated. Three error sources turned out to be relevant for typical three-terminal measurements on solid oxide fuel cells (SOFC) thin film electrodes on YSZ electrolytes.

- Shift of the reference electrode (RE) equipotential line over frequency: Electrodes on SOFC feature ohmic-capacitive properties. The chemical capacitances short-circuit the electrode polarization resistance at higher frequencies and thus the current expands its effective cross section throughout the entire electrolyte. At low frequencies on the other hand, the ohmic resistance of the electrodes limits the cross section expansion. This transition from primary ($\omega \to \infty$) to secondary ($\omega \to 0$) current distribution also determines the potential distribution. In case of asymmetric working electrode (WE)/counter electrode (CE) alignments, this transition causes a shape change of the RE equipotential line over frequency. This leads to the fact that the RE monitors different parts of the sample over the frequency range. The WE/CE asymmetry can be caused by geometry and by different electrochemical electrode properties. The corresponding shift leads to distortions in the impedance spectrum which can affect the results in two ways.

  - Less problematic: The shift occurs in a frequency range that differs from the range of the electrode semicircle. In this case, a separate feature (e.g. an inductive semicircle) appears in the impedance spectrum. The derived electrode properties remain rather unaffected, provided that the distorted part is excluded from the spectrum fit.

  - Problematic: The frequency ranges of the RE equipotential line shift and the electrode semicircle overlap. In that case, the derived electrode

properties are erroneous without leaving visible non-idealities in the impedance spectrum. This may be the case for WE and CE exhibiting different polarization resistances but identical relaxation times or peak frequencies, respectively.

- Short circuit effect:
  Finite elements analyses showed that geometries with a spatially extended RE near the main current path may cause a short circuit through the RE. The consequence is an additional ohmic-capacitive voltage drop which again distorts the resulting impedance spectrum. The short circuit effect can be avoided by a sample geometry that does not lead to a potential spread across the RE.

- Three-point transfer characteristic:
  Coupling capacitances between the electrodes can lead to distorted spectra features due to altered impedance response behaviour. In case of the ring geometry with high ohmic electrodes, an artifact semicircle preceding the electrode semicircle can be attributed to this effect. The capacitances are mainly intrinsic properties of the cell and only a small part arises from the unshielded measuring probes within the measuring apparatus. The capacitance of the probes may be eliminated by active shielding, but the remaining intrinsic part may still easily cause artifacts.

On basis of these insights, the overview of potential error sources (Table 2.1) stated in the beginning of this thesis can be shortened to the list in Table 5.1.

Table 5.1: Relevant error and artifact sources in three-terminal impedance spectroscopy of thin film SOFC electrodes on YSZ

Intrinsic	LF	HF
RE equipotential line shift over frequency due to asymmetry (Non uniform current distribution)	x	x
RE Short circuit effect	x	x

Mainly intrinsic, partly external	LF	HF
Three-terminal transfer characteristic and coupling capacitances	x	x

Based on the findings of this work, the single wing geometry was developed as a suitable geometry for three-terminal measurements. A symmetric protrusion on the electrolyte serves to host the RE. The protrusion avoids significant current flow close to the RE and therefore, the RE potential shift in consequence of asymmetric WE/CE properties is rather small. Furthermore, the potential spread over the RE is minimized to avoid the short circuit effect.

When dealing with measurements under bias, WE/CE properties are inevitably asymmetric. This asymmetry is particularly critical for low-ohmic electrodes and a CE with identical relaxation times as the measured WE. In this case, the RE equipotential line shift is superposed by the electrode semicircle and the deduced polarization resistance and chemical capacitance are erroneous. Quantitatively, this effect depends on the ratios $a = \frac{R_{\text{electrolyte}}}{R_{\text{measured electrode}}}$ and $b = \frac{h_{\text{protrusion}}}{h_{\text{sample}}}$. Both ratios should be small to minimize errors.

As an outlook, the simulation results of the single wing geometry should be verified by experiments. Therefore, a production routine for the single wing geometry needs to be developed. First of all, the YSZ protrusion needs to be carved. Moreover, a shadow mask is required to screen the protrusion during the thin film deposition by pulsed laser deposition. After a production routine is established, a measuring apparatus has to be built. To ensure easy handling, a clamping mechanism would be the preferred way to contact the RE. At the same time it is important not to oversize the platinum sheets to prevent geometrical capacitances and thus avoid three-terminal impedance transfer characteristic distortions.

Acknowledgements

First and foremost, I would like to thank Prof. Jürgen Fleig for making this master's thesis possible at the solid state electrochemistry research group. The advice I received was always helpful and lead me towards the right direction.

Moreover, I want to greatly thank my supervisor Alex Schmid for his advice and never ending patience. Always taking time and giving me detailed explanations on defect chemistry, scientific methods and Russian Sci-Fi novels contributed a lot to the quality of my output.

An equally great thank you goes out to my second supervisor Tobias M. Huber for always helping me with questions I had during my thesis. His practical skills and ideas brought me forward lots of times. Hopefully, the measuring apparatuses of huber scientific will once be the market leader in the SOFC research sector.

Furthermore, I want to thank Prof. Günter Fafilek for the crucial advice on electrical measuring engineering. I greatly appreciate the time he took to answer my questions.

I also want to thank Prof. Wolfgang Gawlik for taking the time to act as second examiner and supporting the master's degree with individual focus.

Special thanks also go out to my office colleagues Andreas Wachter-Welzl and Harald Summerer. The chit chat about computer games and the best graphics processing units was always a nice distraction from work.

Thank you to all the colleagues of the solid state electrochemistry research group. You contribute to a wonderful working environment which is a big plus for everyone who works with you.

Appendix

References

[1] A. J. Schwab. *Elektroenergiesysteme*. 2012. ISBN: 978-3-642-21957-3. DOI: 10. 1007/978-3-642-21958-0. arXiv: arXiv:1011.1669v3. URL: http://link. springer.com/10.1007/978-3-642-21958-0.

[2] M. A. Laguna-Bercero. "Recent advances in high temperature electrolysis using solid oxide fuel cells: A review". In: *Journal of Power Sources* 203 (2012), pp. 4–16. ISSN: 03787753. DOI: 10.1016/j.jpowsour.2011.12.019. URL: http://dx.doi.org/10.1016/j.jpowsour.2011.12.019.

[3] N. Q. Minh. "Solid oxide fuel cell technology – Features and applications". In: *Solid State Ionics* 174.1-4 (2004), pp. 271–277. ISSN: 01672738. DOI: 10. 1016/j.ssi.2004.07.042.

[4] A. Choudhury, H. Chandra, and A. Arora. "Application of solid oxide fuel cell technology for power generation – A review". In: *Renewable and Sustainable Energy Reviews* 20 (2013), pp. 430–442. ISSN: 13640321. DOI: 10.1016/j. rser.2012.11.031. URL: http://dx.doi.org/10.1016/j.rser.2012.11. 031.

[5] S. Badwal and K. Foger. "Solid oxide electrolyte fuel cell review". In: *Ceramics International* 22.3 (1996), pp. 257–265. ISSN: 02728842. DOI: 10.1016/ 0272-8842(95)00101-8. URL: http://www.sciencedirect.com/science/ article/pii/0272884295001018.

[6] S. J. Skinner. "Recent advances in Perovskite-type materials for solid oxide fuel cell cathodes". In: *International Journal of Inorganic Materials* 3.2 (2001), pp. 113–121. ISSN: 1466-6049. DOI: 10.1016/S1466-6049(01)00004- 6.

[7] W. Zhu and S. Deevi. "Development of interconnect materials for solid oxide fuel cells". In: *Materials Science and Engineering: A* 348.1 (2003), pp. 227– 243. ISSN: 09215093. DOI: 10.1016/S0921-5093(02)00736-0.

References

[8]   J. W. Fergus. "Metallic interconnects for solid oxide fuel cells". In: *Materials Science and Engineering A* 397.1-2 (2005), pp. 271–283. ISSN: 09215093. DOI: 10.1016/j.msea.2005.02.047.

[9]   V. Brichzin, J. Fleig, H. U. Habermeier, and J. Maier. "Geometry dependence of cathode polarization in solid oxide fuel cells investigated by defined Sr-doped LaMnO3 microelectrodes". In: *Electrochemical and Solid State Letters* 3.9 (2000), pp. 403–406. ISSN: 10990062. DOI: 10.1149/1.1391160.

[10]   C. H. Hamann and W. Vielstich. *Elektrochemie.* 4th ed. Weinheim: Wiley, 2005, p. 662. ISBN: 3-527-31068-1.

[11]   M. Nagata, Y. Itoh, and H. Iwahara. "Dependence of observed overvoltages on the positioning of the reference electrode on the solid electrolyte". In: *Solid State Ionics* 67.3-4 (1994), pp. 215–224. ISSN: 01672738. DOI: 10.1016/0167-2738(94)90008-6.

[12]   G. Hsieh, T. Mason, E. Garboczi, and L. Pederson. "Experimental limitations in impedance spectroscopy: Part III. Effect of Reference Electrode Geometry/Position". In: *Solid State Ionics* 96 (1997), pp. 153–172. ISSN: 01672738. DOI: 10.1016/S0167-2738(97)00075-1.

[13]   J. Winkler, P. Hendriksen, N. Bonanos, and M. Mogensen. "Geometric Requirements of Solid Electrolyte Cells with a Reference Electrode". In: *Journal of The Electrochemical Society* 145.4 (1998), pp. 1184–1192. ISSN: 00134651. DOI: 10.1149/1.1838436.

[14]   S. Adler. "Reference Electrode Placement in Thin Solid Electrolytes". In: *Journal of The Electrochemical Society* 149.5 (2002), E166–E172. ISSN: 00134651. DOI: 10.1149/1.1467368.

[15]   M. Cimenti, A. C. Co, V. I. Birss, and J. M. Hill. "Distortions in electrochemical impedance spectroscopy measurements using 3-electrode methods in SOFC. I – effect of cell geometry". In: *Fuel Cells* 7.5 (2007), pp. 364–376. ISSN: 16156846. DOI: 10.1002/fuce.200700019.

References

[16] M. Cimenti, V. I. Birss, and J. M. Hill. "Distortions in electrochemical impedance spectroscopy measurements using 3-electrode methods in SOFC. II – Effect of electrode activity and relaxation times". In: *Fuel Cells* (2007), pp. 377–391. ISSN: 16156846. DOI: `10.1002/fuce.200700020`.

[17] S. B. Adler, B. T. Henderson, M. A. Wilson, D. M. Taylor, and R. E. Richards. "Reference electrode placement and seals in electrochemical oxygen generators". In: *Solid State Ionics* 134.1-2 (2000), pp. 35–42. ISSN: 01672738. DOI: `10.1016/S0167-2738(00)00711-6`.

[18] A. Hashibon, S. Raz, and I. Riess. "Preferred position for the reference electrode in solid state electrochemistry". In: *Solid State Ionics* 149 (2002), pp. 167–176.

[19] J. Rutman and I. Riess. "Placement of reference electrode in solid state electrolyte cells". In: *Solid State Ionics* 179.21-26 (2007), pp. 913–918. ISSN: 01672738. DOI: `10.1016/j.ssi.2008.01.071`.

[20] G. J. Offer, P. Shearing, J. I. Golbert, D. J. L. Brett, A. Atkinson, and N. P. Brandon. "Using electrochemical impedance spectroscopy to compensate for errors when measuring polarisation curves during three-electrode measurements of solid oxide fuel cell electrodes". In: *Electrochimica Acta* 53.26 (2008), pp. 7614–7621. ISSN: 00134686. DOI: `10.1016/j.electacta.2008.04.001`.

[21] J. A. Escobar, S. Pakalapati, I. B. Celik, and H. Finklea. "A Correction for Impedance Measurements using the Three Point Electrode Technique in SOFCs". In: *ECS Transactions* 25.2 (2009), pp. 391–400. ISSN: 19385862. DOI: `10.1149/1.3205548`. URL: `http://ecst.ecsdl.org/content/25/2/391.abstract`.

[22] G. Hsieh, S. J. Ford, T. O. Mason, and L. R. Pederson. "Experimental limitations in impedance spectroscopy: Part I – Simulation of reference electrode artifacts in three-point measurements". In: *Solid State Ionics* 91.3-4 (1996), pp. 191–201. ISSN: 01672738. DOI: `10.1016/S0167-2738(96)00481-X`.

References

[23]   G. Hsieh, T. Mason, and L. Pederson. "Experimental limitations in impedance spectroscopy: Part II – Electrode artifacts three point measurements on Pt/YSZ". In: *Solid State Ionics* 91.3-4 (1996), pp. 203–212. ISSN: 0167-2738. DOI: http://dx.doi.org/10.1016/S0167-2738(96)83020-7.

[24]   G. Fafilek. "The use of voltage probes in impedance spectroscopy". In: *Solid State Ionics* 176.25-28 (2005), pp. 2023–2029. ISSN: 01672738. DOI: 10.1016/j.ssi.2004.06.024.

[25]   A. T. Tran, F. Huet, K. Ngo, and P. Rousseau. "Artefacts in electrochemical impedance measurement in electrolytic solutions due to the reference electrode". In: *Electrochimica Acta* 56.23 (2011), pp. 8034–8039. ISSN: 00134686. DOI: 10.1016/j.electacta.2010.12.088. URL: http://dx.doi.org/10.1016/j.electacta.2010.12.088.

[26]   A. Battistel, M. Fan, J. Stojadinović, and F. La Mantia. "Analysis and mitigation of the artefacts in electrochemical impedance spectroscopy due to three-electrode geometry". In: *Electrochimica Acta* 135 (2014), pp. 133–138. ISSN: 00134686. DOI: 10.1016/j.electacta.2014.05.011.

[27]   S. Fletcher. "The two-terminal equivalent network of a three-terminal electrochemical cell". In: *Electrochemistry Communications* 3.12 (2001), pp. 692–696. DOI: 10.1016/S1388-2481(01)00233-8.

[28]   J. Newman. "Current Distribution on a Rotating Disk below the Limiting Current". In: *Journal of The Electrochemical Society* 113.12 (1966), p. 1235. ISSN: 00134651. DOI: 10.1149/1.2423795.

[29]   J. Dygas and M. Breiter. "Measurements of large impedances in a wide temperature and frequency range". In: *Electrochimica Acta* 41.7-8 (1996), pp. 993–1001. ISSN: 00134686. DOI: 10.1016/0013-4686(95)00430-0.

[30]   J. Fleig, J. Jamnik, and J. Maier. "Inductive Loops in Impedance Spectroscopy Caused by Electrical Shielding". In: *Journal of The Electrochemical Society* 143.1 (1996), pp. 3636–3641. DOI: 10.1149/1.1837263.

References

[31] G. Fafilek and M. W. Breiter. "Instrumentation for ac four-probe measurements of large impedances". In: *Journal of Electroanalytical Chemistry* 430 (1997), pp. 269–278. ISSN: 15726657. DOI: `10.1016/S0022-0728(97)00263-5`.

[32] D. D. Edwards, J. Hwang, S. J. Ford, and T. O. Mason. "Experimental limitations in impedance spectroscopy : Part V . Apparatus contributions and corrections". In: *Solid State Ionics* 99 (1997), pp. 85–93. DOI: `10.1016/S0167-2738(97)00075-1`.

[33] M. D. Levi, V. Dargel, Y. Shilina, D. Aurbach, and I. C. Halalay. "Impedance spectra of energy-storage electrodes obtained with commercial three-electrode cells: Some sources of measurement artefacts". In: *Electrochimica Acta* 149 (2014), pp. 126–135. ISSN: 00134686. DOI: `10.1016/j.electacta.2014.10.083`. URL: `http://dx.doi.org/10.1016/j.electacta.2014.10.083`.

[34] A. Schmid. "Electrochemical properties of LSF upon polarization". Master's Thesis. TU Wien, 2016.

[35] J. Fleig. "Solid Oxide Fuel Cell Cathodes: Polarization Mechanisms and Modeling of the Electrochemical Performance". In: *Annual Review of Materials Research* 33.1 (2003), pp. 361–382. ISSN: 1531-7331. DOI: `10.1146/annurev.matsci.33.022802.093258`. URL: `http://www.annualreviews.org/doi/10.1146/annurev.matsci.33.022802.093258`.

[36] J. Jamnik and J. Maier. "Treatment of the Impedance of Mixed Conductors Equivalent Circuit Model and Explicit Approximate Solutions". In: *Journal of The Electrochemical Society* 146.11 (1999), p. 4183. ISSN: 00134651. DOI: `10.1149/1.1392611`.

[37] F. S. Baumann, J. Fleig, H. U. Habermeier, and J. Maier. "Impedance spectroscopic study on well-defined (La,Sr)(Co,Fe)O3-d model electrodes". In: *Solid State Ionics* 177.11-12 (2006), pp. 1071–1081. ISSN: 01672738. DOI: `10.1016/j.ssi.2006.02.045`.

References

[38] J. Fleig and J. Maier. "Finite element calculations of impedance effects at point contacts". In: *Electrochimica Acta* 41.7-8 (1996), pp. 1003–1009. ISSN: 00134686. DOI: `10.1016/0013-4686(95)00431-9`. URL: `http://linkinghub.elsevier.com/retrieve/pii/0013468695004319`.

[39] A. Prechtl. *Vorlesungen über die Grundlagen der Elektrotechnik – Band 2*. 2nd ed. Vienna: SpringerWienNewYork, 2008. ISBN: 3-211-82685-8.

[40] A. Prechtl. *Vorlesungen über die Grundlagen der Elektrotechnik – Band 1*. 2nd ed. Vienna: SpringerWienNewYork, 2006. ISBN: 3-211-82553-3.

[41] J. Federau. *Operationsverstärker: Lehr- und Arbeitsbuch zu angewandten Grundschaltungen*. 2013, p. 340. ISBN: 3834804584. DOI: `10.1007/978-3-8348-2146-1`.

[42] S. Kogler, A. Nenning, G. M. Rupp, A. K. Opitz, and J. Fleig. "Comparison of Electrochemical Properties of La0.6Sr0.4FeO3-d Thin Film Electrodes: Oxidizing vs. Reducing Conditions". In: *Journal of the Electrochemical Society* 162.3 (2015), F317–F326. ISSN: 0013-4651. DOI: `10.1149/2.0731503jes`. URL: `http://jes.ecsdl.org/cgi/doi/10.1149/2.0731503jes`.

[43] A. K. Opitz, A. Lutz, M. Kubicek, F. Kubel, H. Hutter, and J. Fleig. "Investigation of the oxygen exchange mechanism on Pt | yttria stabilized zirconia at intermediate temperatures : Surface path versus bulk path". In: *Electrochimica Acta* 56 (2011), pp. 9727–9740. DOI: `10.1016/j.electacta.2011.07.112`.

[44] N. H. Perry, S. Kim, and T. Mason. "Local electrical and dielectric properties of nanocrystalline yttria-stabilized zirconia". In: *Journal of Materials Science* 43 (2008), pp. 4684–4692. DOI: `10.1007/s10853-008-2553-x`.

[45] S. B. Adler. "Electrode Kinetics of Porous Mixed-Conducting Oxygen Electrodes". In: *Journal of The Electrochemical Society* 143.11 (1996), p. 3554. ISSN: 00134651. DOI: `10.1149/1.1837252`. arXiv: `arXiv:1011.1669v3`. URL: `http://jes.ecsdl.org/cgi/doi/10.1149/1.1837252`.

References

[46] A. Leonide. "SOFC Modelling and Parameter Identification by means of Impedance Spectroscopy". PhD Thesis. Karlsruhe Institut für Technologie, 2010. ISBN: 978-3-86644-538-3.

[47] Y. Hoshi, Y. Narita, K. Honda, T. Ohtaki, I. Shitanda, and M. Itagaki. "Optimization of reference electrode position in a three-electrode cell for impedance measurements in lithium-ion rechargeable battery by finite element method". In: *Journal of Power Sources* 288 (2015), pp. 168–175. ISSN: 0378-7753. DOI: `10.1016/j.jpowsour.2015.04.065`. URL: `http://dx.doi.org/10.1016/j.jpowsour.2015.04.065`.

List of Figures

110

List of Tables

Eidesstattliche Erklärung

Hiermit erkläre ich, dass die vorliegende Arbeit gemäß Code of Conduct – Regeln zur Sicherung guter wissenschaftlicher Praxis (in der aktuellen Fassung des jeweiligen Mitteilungsblattes der TU Wien), insbesondere ohne unzulässige Hilfe Dritter und ohne Benutzung anderer als der angegebenen Hilfsmittel, angefertigt wurde. Die aus anderen Quellen direkt oder indirekt übernommenen Daten und Konzepte sind unter Angabe der Quelle gekennzeichnet.
Die Arbeit wurde bisher weder im In- noch im Ausland in gleicher oder in ähnlicher Form in anderen Prüfungsverfahren vorgelegt.

Wien, 26. Jänner 2018

Richard Schlesinger